Finite Element Modelling of Off-Road Tyres

by

Johannes Martinus Conradie

University of Pretoria

Supervisor: Professor P. S. Heyns

Co-supervisor: Professor P. S. Els

2014

Submitted in fulfilment of part of the requirements for the degree of Master of Engineering (Mechanical) in the Faculty of Engineering, the Built Environment and Information Technology

Finite Element Modelling of Off-Road Tyres

Author: J.M. Conradie

Supervisors: Professors P.S. Heyns & P.S. Els

Department: Mechanical and Aeronautical Engineering

Degree: Master of Engineering

Summary

Most tyre models developed to date require a fair amount of data before an accurate representation of the tyre can be obtained. This study entails the development of a simplified, yet accurate, non-linear Finite Element (FE) model of an “off-road” tyre to study the behaviour of the tyre due to radial loading conditions. The study aims to develop a FE tyre model that can solve fast and be accurate enough to be used in multibody dynamic vehicle simulations. A model that is less complex than conventional detailed FE models is developed.

The work explores the use of superimposed finite elements to model the varying stiffness in the respective orthogonal directions of the sidewall and tread of the tyre. Non-linear elements defined by Neo-Hookean or Ogden models and elements with different linear orthogonal stiffnesses are superimposed onto each other to simulate the global material properties of the tread and the sidewall of the tyre investigated.

The geometry of the tyre studied was measured experimentally using laser displacement transducers and digital image correlation techniques. Material properties of segments of the tyre were obtained by performing tensile tests on samples. Since the rubber slipped against the clamps during the experiment, deformation of the segments was also measured using digital image correlation. These geometrical and material properties were used as input to develop a finite element model of an “off-road” tyre.

Measurements were conducted using laser displacement transducers, load cells mounted to actuators, etc. to obtain accurate sidewall deformation profiles and global radial load vs. displacement curves for different radial loading conditions. The data obtained from the results was used to validate the tyre model developed.

Numerous analyses are performed with different combinations of moduli of elasticity in the respective orthogonal directions of the sidewall stiffness and the tread to investigate its influence on the global behaviour of the tyre model.

The main focus of the project was to develop a tyre model from data obtained from laser and photogrammetry measurements in a laboratory that accurately represents tyre behaviour due to radial forces. A finite element model that can simulate the effect of radial forced and obstacles on a tyre was developed. The use of two subsets of elements, superimposed onto each other to simulate global material properties of the rubbers, steel wires, polyester and nylon threads, was investigated.

The combination of material properties that gave the best fit for all the load cases investigated were determined. The finite element model correlated well with the load vs. displacement graphs and sidewall displacement profiles determined experimentally.

The solving time is still fairly high and is still not quite suitable for real-time dynamic simulation. However, it solves faster than more complex tyre models where details of steel wires, etc. are included in the model.

For future studies it is recommended that different element types be investigated in the tyre model.

The study proves that equivalent material properties can be used to simulate the composite properties of the materials in tyres. Most tyres can be divided into a few regions that each has its own material structure right through the region. These regions can be characterized by simple tests and the input can be used as a first estimation of the tyre's material properties for the model.

Accurate validation criteria should be used to validate the tyre model if time does not allow for excessive testing of the material properties of all the rubber, steel wires, polyester threads, etc. Geometric displacement data at various loading conditions can be used for validation of the tyre model.

The model developed can be used to investigate the effect of different stiffnesses and other material changes in the sidewall or tread of a tyre. Useful insight can be obtained from the finite element model developed for dynamic simulation where the force vs. global displacement data is important.

Keywords: finite element analysis, finite element modelling, model updating, experimental testing, non-linear modelling, non-linear materials, tyres, multibody, ride simulation

Acknowledgements

I would like to thank the following people for their support and contributions:

- Prof PS Heyns – Supervisor – University of Pretoria
- Prof PS Els – Co-Supervisor – University of Pretoria
- Mr George Breitenbach – Lab assistance – Sasol Laboratory, University of Pretoria
- Mr Herman Booysen – Lab assistance – Sasol Laboratory, University of Pretoria
- Mr Gerrit Visser – Technical assistance with MSC.Marc & MSC.Mentat – Esteq
- Mr Neels Smit – Lab assistance – Machine Labs, University of Pretoria

Table of contents

List of figures

List of tables

Nomenclature

Symbol	**Description**
1, 2, 3, 4, 5, 6	Represents orthogonal directions
A_i	Initial area of sample
C	Stiffness matrix
C_{10}	Neo-Hookean / Mooney-Rivlin constant
C_{01}	Mooney-Rivlin constant
C_{11}	Mooney-Rivlin constant
C_{20}	Signiorini constant
C_{30}	James Green Simpson constant
CB	Distance [m]
E	Young's modulus [Pa]
F	Force [N]
G	Shear modulus [Pa]
H	Height [m]
I_1	Mooney-Rivlin coefficient
I_2	Mooney-Rivlin coefficient
J	Jacobian matrix
l	Final length of sample [m]
L	Original length of sample [m]
$\mathbf{m}, \mathbf{n}$	Vectors representing lateral contraction and axial extension
S	Correlation function / compliance matrix
U	Distance [m]
V	Displacement [m]
W	Strain energy density function
x, y, z	Distance / displacement / represents ISO coordinate system [m]
Δ	Change
α	Ogden exponent
γ	Engineering shear strain
ε	Engineering strain
λ	Principal stress [Pa]
μ	Ogden coefficient
ν	Poisson's ratio
$\nu_{a\text{-}r}$	Poisson's ratio
$\nu_{r\text{-}c}$	Poisson's ratio (the negative ratio of strain in the radial direction relative to the strain in the circumferential direction in the sidewall of the tyre)
$\nu_{c\text{-}r}$	Poisson's ratio (the negative ratio of strain in the circumferential direction relative to the strain in the radial direction in the sidewall of the tyre)
$\nu_{la\text{-}lo}$	Poisson's ratio (the negative ratio of strain in the lateral direction relative to the strain in the longitudinal direction in the tread of the tyre)
$\nu_{lo\text{-}la}$	Poisson's ratio (the negative ratio of strain in the longitudinal direction relative to the strain in the lateral direction in the tread of the tyre)

σ	Normal stress [Pa]
τ	Shear stress [Pa]

1 Background and objectives

1.1 Introduction

The contact interactions between tyres and the road largely affect the driving performance and dynamic properties of vehicles. The rubber structure of a tyre must work reliably over a large range of dynamic conditions.

Tyre-road interaction can be optimized to improve the handling of a vehicle and to ensure the safety and comfort under any circumstances. Tyres are the only parts of a vehicle which are in contact with the road. Safety in acceleration, braking, steering and cornering all depend on a relatively small contact area between the road and the tyres. Tyres can therefore be considered one of the most important components of vehicles. They must fulfil a fundamental set of functions such as provide cushioning and damping, provide stability and generate steering response, while minimising roll resistance and generation of noise and vibration.

Therefore, there is a large interest in the behaviour of tyres in the field of vehicle dynamics. Information about how tyres operate can give great insight into design considerations. Many investigators have tried to develop robust mathematical models during the past three decades to describe the kinematics and dynamics of the rolling of pneumatic tyres on rigid and deformable surfaces. Accurate simulations of tyre deformation can be used as an instrument to compare the performance of tyres under a wide range of operating conditions and designs. (Mc Allen, et al., 1996; Orteu, 2009; Ghoreishy, 2008; Mohsenimanesh, et al., 2009)

Various studies have been done on truck tyres (Hua & White, 2002; Darnell, et al., 1997; Zhang, et al., 2002), and automobile tyres (Ghoreishy, 2009; Kindt, et al., 2009; Korunovic, et al., 2008; Merzouki, et al., 2007; Tönük & Ünlüsoy, 2001), but actual tests on off-road tyres are not as common. This may be due to the ease of handling of the smaller tyres in laboratories.

Most tyre models developed to date however require fairly detailed tyre characteristics before an accurate representation of the tyre can be obtained. To reduce the burden of determining these characteristics, there is a need for simplified models which still captures the essential physics of the problem well enough for accurate multidynamic modelling of vehicles.

1.2 Scope of project

This study first explores the range of existing tyre models found in the literature. Possibilities for the development of a simplified FE (Finite Element) model, using less data from experiments, are then investigated. Various measuring techniques are implemented to obtain accurate deformation profiles for different loading conditions. The data obtained is subsequently used as input for the development of the simplified tyre model. The data acquired is also used to verify the accuracy of the model.

The following analyses are conducted to parameterise the FE model:

- Material characteristics
    - Segments of the tyre carcass and tread are tested for its material properties using tensile tests. The properties obtained are built into the model.
- Inflation analysis
    - The deformed shape is compared to real experimentally measured profiles.
- Analysis of vertically loaded tyre
    - Cleat test simulations are performed. Load-deflection curve (global stiffness of the tyre) and sidewall deformation profiles are used for validating and updating the model.

1.3 Research objectives

The primary objectives of this research are to:

- Explore the most recent developments in tyre modelling to understand the limitations and the strengths of the most advanced tyre models that have already been developed.
- Parameterize the properties of an “off-road” tyre through a range of quasi-static experiments in a laboratory. A tyre model that requires less experimental data of the material properties in the tyre than conventional empirical tyre models is developed. Accurate geometric data of different loading conditions will be used to update the model. The tyre structure will be divided into three main regions, namely the tread region, the sidewall region and the bead region.
- Develop a model that is less complex than conventional detailed FE models. The aim is to develop a tyre model that can solve fast enough to be used in multibody dynamic vehicle simulations. The use of elements with equivalent homogeneous properties is investigated (instead of inserting rebar inserts or using layered composite elements that are computationally intensive to solve). In a simulation of a tyre the specific material properties of the materials that the tyre consists of, are not of interest. The global behaviour of the composite material of the tyre is important however.
- Ensure that the tyre model can accurately simulate tyre behaviour for quasi-static analyses. The tyre model is validated and updated through the use of deformation profiles of the sidewall and radial load vs. displacement curves obtained from experiments. Different loading conditions are used to update and validate the tyre model to enable it to accurately simulate reactions experienced upon radial forces. Advanced measurement equipment (laser displacement transducers, High Definition (HD) cameras, digital image correlation software, etc.) are used to develop input data and validation data for the model.

1.4 Resources

For the purpose of this project experiments, measurements, etc. are done using a 235/85 R 16 tyre with radial construction. Various research projects have already been done on a Land Rover by the Vehicle Dynamics Group at the University of Pretoria. The investigation of this tyre can give insight on the behaviour of off-road tyres.

There are some advanced capabilities in the Sasol Laboratory for Structural Mechanics at the University of Pretoria:

1. Unique stereo photogrammetry equipment.
2. Laser vibrometry equipment
3. Good experimental and measuring equipment.

The study addresses a number of problems. The tyre profile is measured using stereo photogrammetry and laser measurement (refer to Chapter 3). Some basic characterizing tests are done to obtain the necessary material properties for the tyre model. These include stiffness tests and full field measurements of the tyre deflection, using digital image correlation.

Various documents and articles have been published that dealt with finite element models of tyres. The most important difficulties in finite element simulation of tyres are as follows (Yan, 2001):

1. Geometric non-linearity due to large deformations
2. Material non-linearity
3. Incompressibility constraint on deformation of elastomers
4. Non-linear boundary condition (contact boundary)

Establishing the contact boundary condition is a very important task. A sufficient description of the interactions between tyre and road must be defined, since all the other components of the chassis influence the vehicle dynamic properties through the tyre contact forces and torques.

MSC.Marc and MSC.Mentat combine to provide accurate non-linear finite element solutions (pre-processing, solution, and post-processing). It can be used to assess the structural integrity and performance of objects with non-linear geometric properties. MSC.Marc offers robust capabilities for large deformations, to solve static and quasi-static non-linear problems. It enables simulation of part-to-part or part-to-self contact under varying conditions and includes frictions effects. Marc is designed to solve non-linear problems, using advanced mathematics and FE technology to consistently obtain converged solutions for highly non-linear models involving non-linear materials, large strain and displacement, and contact. MSC.Marc 2012 is used to develop the finite element model.

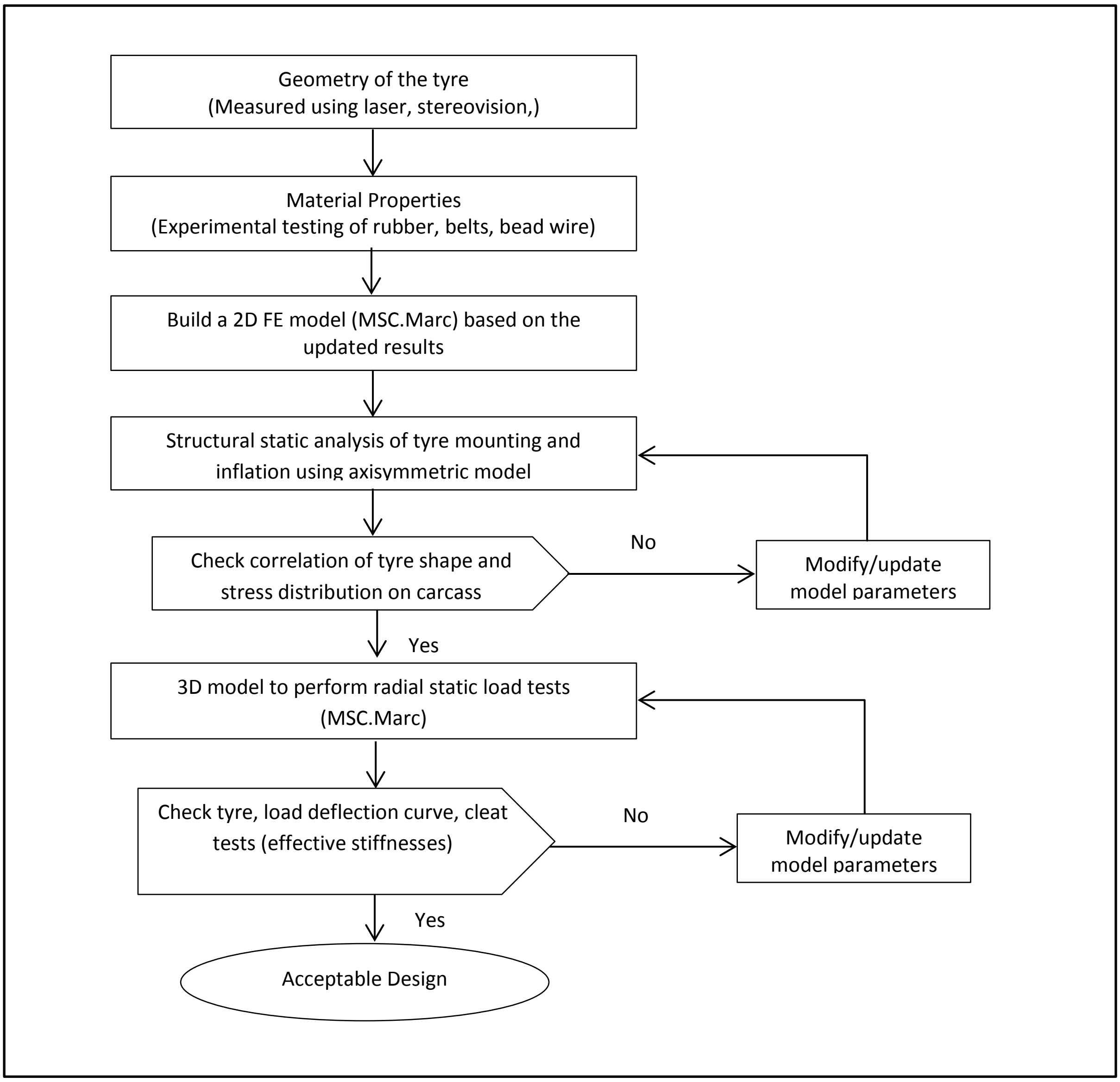

Figure 1.1: Algorithm for the building of the finite element tyre model

1.4 Outline of report

Basic background of tyres is introduced in Chapter 2. Tyre terminology and definitions are discussed in this chapter. Methods of optical measurement are discussed. Relevant non-linear and orthotropic material properties are also discussed.

Chapter 3 describes implementation of the measurement methods to obtain input data for the tyre model and the interpretation of the measurement results. The geometry of the tyre is measured using both optical measuring techniques and laser measurements. The procedures followed to experimentally determine the global material properties of tyre segments are also discussed.

Chapter 4 describes how the data from Chapter 3 is used to build FE models of the samples that are tested to determine if the material properties can be simulated with the different stiffnesses in the different orthogonal directions. Chapter 4 describes how the material properties and loading conditions are implemented to build a three dimensional finite element model.

In Chapter 5 the experimental tests that are performed to determine the global stiffness of the tyre for different loading conditions, are explained. The measurement of sidewall deformation at these loading conditions is also discussed.

The results from the FE model are compared to the experimental data in Chapter 6 and a summary of the results is given in Chapter 7. Conclusions and recommendations for future studies are also provided.

2 Literature study

2.1 Tyre construction and basic tyre terminology

Tyres have complex structures and are difficult to analyse, but they have a most significant effect on the behaviour of any vehicle. Describing the tyre performance is challenging, but necessary in the automotive industry, where simulation becomes progressively more important in designing and testing. Various ranges of different kinds of tyres are used on a large range of different kinds of vehicles.

Most pneumatic tyres consist of a specific combination of rubber compounds, cord and steel belts (Kondé, et al., 2013). The structure of most modern tyres can be divided into main parts/regions as shown in Figure 2.1. These are the tread, the sidewall and the bead region.

The body (or carcass) of the tyre consists of rubber and fabric layers of high modulus cords embedded into it which give the tyre its strength and flexibility. The fabric used usually consists of rayon, nylon or polyester cords. The sidewalls and tread are made of chemically treated rubber with different elastic moduli. The tread is the only part of the tyre in contact with road and has to be much harder than the sidewalls. The only type of material successfully used so far has been rubber (natural or synthetic) or rubber-like material. It is reinforced by suitable ingredients such as carbon black to obtain the required abrasion resistance. (Miège & Popov, 2004) Embedded in the two inner edges of the tyre are steel loops called beads. The bead bundles serve to anchor the inflated tyre to the wheel rim when inflated to its specified operating pressure. A more detailed description of common tyre components was published by the NHTSA (National Highway Traffic Safety Administration) (Gent & Walter, 2005).

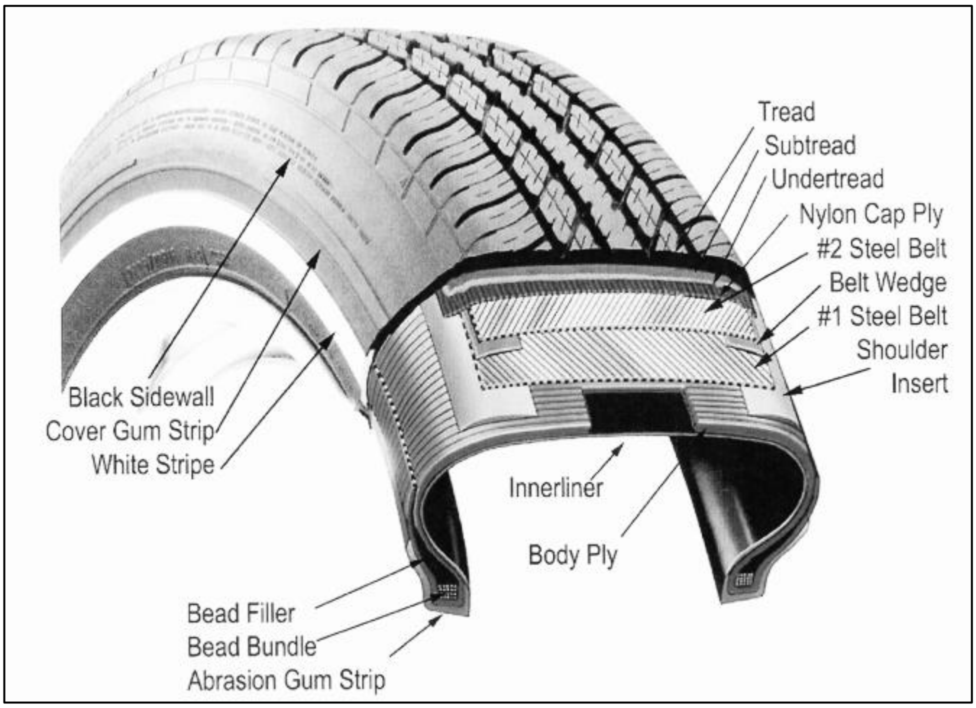

Figure 2.1: Typical structure of a radial-ply tyre (Gent, 2007)

Automobile tyres can usually be divided into two main categories. The first is tyres that use cross ply construction and are commonly referred to as bias ply tyres. The second is radial ply tyre construction, as shown in Figure 2.1, which consists of body ply cords extending from the beads and across the tread. The cords are laid at approximately right angles to the centreline of the tread, parallel to each other. There are usually also stabilizer belts directly beneath the tread in radial tyres. The tyre that is used for the purpose of this study has radial ply construction and its specifications are discussed in Chapter 3.1.

2.2 Forces and moments acting on tyres

Two noticeable conventions for vehicle axis coordinate systems exist (ISO and SAE) that describe forces and moments generated by a tyre. A simplified version of the ISO tyre coordinate system is shown below in Figure 2.2. The origin of the ISO contact-patch system lies at the local road plane at the tyre contact point.

The force *Fx* acting on the tyre is called the longitudinal force and is positive along the positive x-axis. The positive x-axis lies in the local road plane along the intersection of the wheel plane and the local road plane. The force *Fz* acting on the tyre is called the vertical or normal force (wheel load) and is positive along the positive z-axis. The positive z-axis is perpendicular (normal) to the local road plane and points upward. The force *Fy* acting on the tyre is called the lateral (side) force and is positive along the positive y-axis. The positive y-axis lies in the local road plane and is perpendicular to the positive x-axis and positive z-axis.

The moment *Mx* acting on the tyre is called the overturning couple. The moment *My* acting on the tyre is called the rolling resistance moment. The moment *Mz* acting on the tyre is called the self-aligning torque.

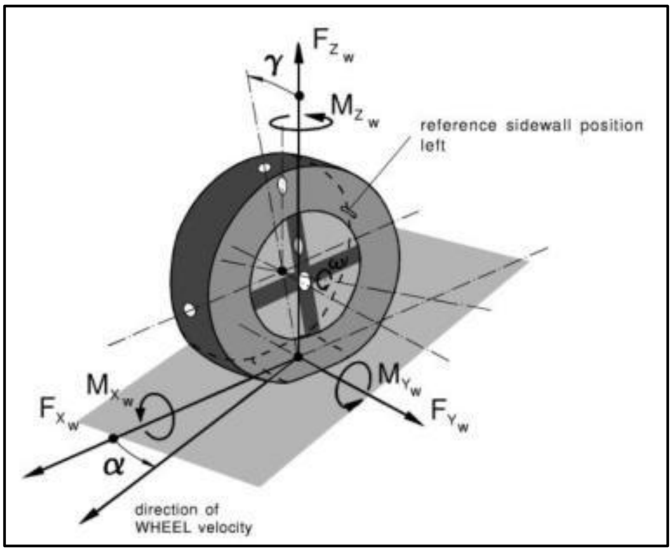

Figure 2.2: ISO tyre sign convention (MF-Tyre & MF-Swift 6.1 Users Manual, 2008)

A lateral force on a rolling pneumatic tyre will cause the tyre to drift to the side. The angle α in Figure 2.2 is called the slip angle. The slip angle is the angle between the direction the tyre is pointing and the direction the tyre is travelling.

In this study, the focus will be on the modelling of the effect of radial forces on “off-road” tyres.

2.3 Existing tyre models for radial forces on tyres

Several mathematical models of tyres have been developed in the last few decades. Models with different levels of complexity and accuracy have been introduced. Tyre models may use entirely different approaches to simulate tyre behaviour. Some existing tyre models that can simulate the tyres on rough roads are shown in Figure 2.3.

Figure 2.4 (partially based on the diagram given by Sugiyama & Suda, 2009) demonstrates how existing tyre models can be categorized by types of application for which the tyres are used. Models varying from full scale tyre experiments and little theory to models based mostly on the theory of the physical tyre behaviour are considered from left to right. Models in the middle will be relatively simple, but it might be less accurate. The model on the far right becomes complex and is not very suitable for application in the simulation of transient vehicle motion. This model may be more suitable for the study of detailed tyre performance in relation to its construction.

Empirical and semi-empirical tyre models primarily use test data from measured force-slip relations on the rolling tyre for the model. Tables or mathematical formulae and certain interpolation schemes are used to describe tyre behaviour. Empirical models like the contact point model are used for vehicle handling analyses. These models are usually assessed with the aid of regression procedures to yield a best fit to the measured data.

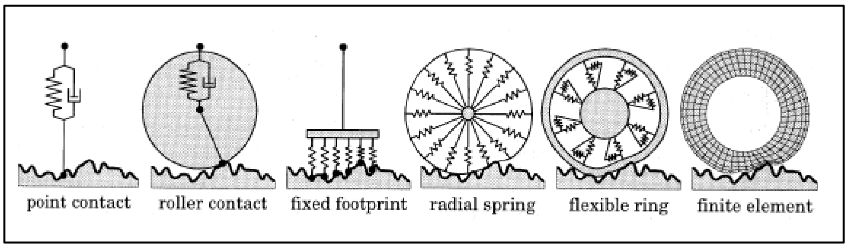

Figure 2.3: Various tyre models used for rolling over obstacles (Zegelaar, 1998)

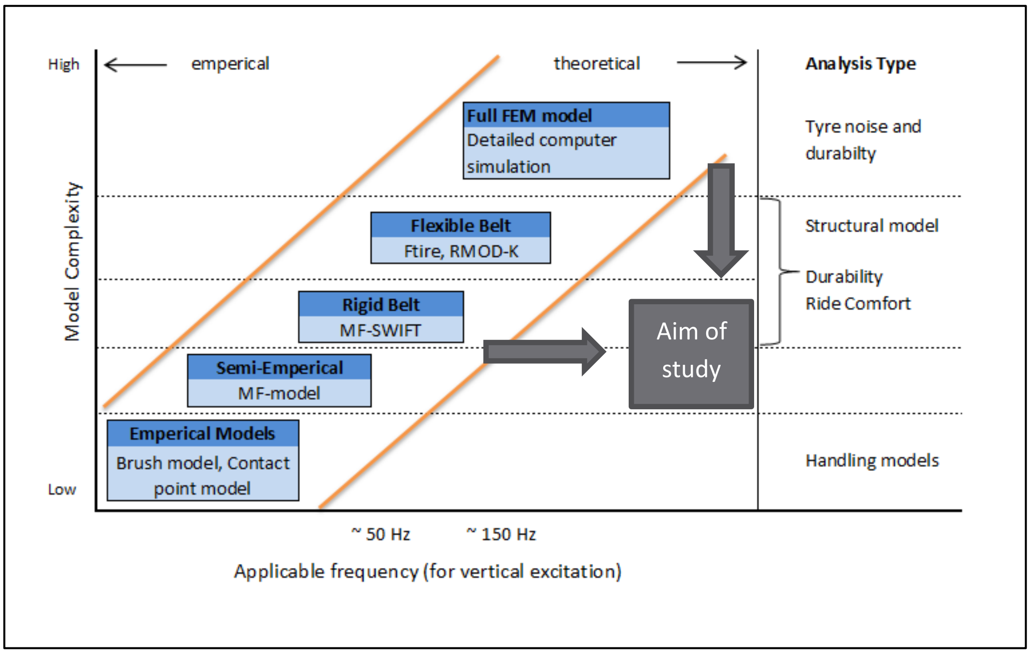

Figure 2.4: Classification of tyre models (Sugiyama & Suda, 2009)

An overview of different existing models in literature is given here:

2.3.1 Single-point contact model

The simplest and the most extensively used vertical model is the classic single-point contact model (Badalamenti & Doyle, 1988). The contact point is suspended with respect to the wheel centre by vertical, longitudinal (circumferential) and lateral springs and dampers. The springs can be modelled linearly or non-linearly. This model is only valid for relatively low frequency road obstacles with a large wavelength (longer than 3 meter) (Pacejka, 2006; Kilner, 1982).

The model can be used on surfaces with random unevennesses generated by filtered white noise. Rolling over rough roads with short wavelengths or discontinuous obstacles (e.g. cleats) gives too high accelerations of the tyre with a point contact model (Zegelaar, 1998).

2.3.2 Roller contact model

The roller contact model consists of a rigid wheel rolling over the obstacles that is connected to the centre of the wheel by one spring and damper. Since there is only one contact point, this model neglects the special cases of road geometry where the tyre has more than one contact point with the road. The contact point is not constrained to lie directly below the wheel axle. Small wavelength irregularities are filtered out by this model and its representation is much better than the single-point contact model (Badalamenti & Doyle, 1988).

2.3.3 Fixed footprint model

The model uses a linearly distributed stiffness and damping in the contact area, thereby averaging road irregularities in the footprint area. This gives a smoother and more realistic excitation of the tyre than the point contact model does (Zegelaar, 1998).

2.3.4 Radial spring model

The tyre is modelled as a radially deformable body. The radial spring model consists of circumferentially distributed independent linear spring elements. The linear stiffnesses used in the model have a limited range through which it is able to predict forces. A model with non-linear degressive radial springs can predict the typical dip in vertical force while rolling over cleats. Badalamenti & Doyle, 1988, enhanced the radial spring model by letting the radial springs depend on the deformation of adjacent springs as well.

2.3.5 MF-Tyre and MF-Swift

A well-known empirical model is the Magic Formula (MF) tyre (Pacejka & Bakker, 1993; Pacejka, 2006). The MF tyre requires comprehensive experimental measurement data, but the model generates fast and accurate results once the necessary coefficients are accurately identified (Sugiyama & Suda, 2009). This class of tyre models is characterized by user-friendliness and efficiency in computation time.

MF-Tyre is TNO Delft-Tyre's implementation of the world-standard Pacejka Magic Formula tyre model. Since MF-Tyres use a semi-empirical approach, fast and robust tyre-road contact force and moment simulation can be accomplished for steady-state and transient tyre behaviour. MF-Tyre has been validated through many experiments and conditions and provides a good fit for the *Fy, Fx* and *Mz* curves (Pacejka, 2006).

MF-Tyre calculates the forces (Fx, Fy) and moments (Mx, My, Mz) acting on the tyre under pure and combined slip conditions on arbitrary 3D roads, using longitudinal and lateral slip, wheel inclination angle (camber), the vertical force (Fz) as input quantities (MD Adams, 2010).

MF-Tyre is valid for large slip angles (larger than 30 degrees), longitudinal slip and large load variations. The model implements the Magic Formula to handle simulations (up to 8 Hz) on a smooth road surface (Besselink, 2006).

The MF-SWIFT (Short Wavelength Intermediate Frequency Tyre) model has the same features as the MF-Tyre model, with some extra added features. MF-Swift uses a rigid ring model in which the tyre belt is assumed to behave like a rigid body. The ring is linked to a rigid rim by circumferential and radial springs and dampers to simulate the sidewall flexibility. The brush model is used to model the horizontal tyre force characteristics, and the residual stiffness is introduced between the contact patch and the rigid ring to represent the static tyre stiffness in the longitudinal, lateral, vertical, and yaw directions (Sugiyama & Suda, 2009). For frequencies up to 60-100 Hz (depending on the tyre) bending modes can be neglected. The model is accurate in these frequency ranges. MF-Swift has been validated using measurements of a rolling tyre (7 to 40 m/s) containing frequencies up to 120 Hz.

Five main aspects of the model structure can be distinguished (MD Adams, 2010; MF-Tyre & MF-Swift 6.1 Users Manual, 2008):

- The belt can be considered as a rigid circular ring for frequencies up to 80 Hz.
- Residual stiffness and damping have been introduced between contact patch and rigid ring to ensure that the total static tyre stiffnesses in the vertical, longitudinal, lateral and yaw directions are correct.
- Horizontal tread element compliance and partial sliding can be simulated using a contact patch model.
- A generic 3D obstacle enveloping model calculates effective road inputs to enable the simulation of the tyre moving over an uneven road surface with the enveloping behaviour of the tyre properly represented.
- The Magic Formula steady-state slip model is defined by MF-Tyre 6.1, which describes the non-linear slip force and moment properties in the effective road plane. This enables an accurate response for handling manoeuvres.

2.3.6 Flexible ring models

Most ring models are limited to in-plane modes, but some more recent models can predict all modes for frequencies up to 300 Hz. (Kindt, et al., 2008) The main assumption of the model developed by Kindt et al. is that the dynamic behaviour of a tyre in this frequency range can be approximated by a flexible three-dimensional ring on an elastic foundation. The model is based on simple geometric properties and experimental modal parameters. Although the tread band by Kindt et al. was modelled as an isotropic three-dimensional ring, the tyre model still gave acceptably accurate results for tyre dynamic behaviour below 300 Hz. The sidewalls of the model were approximated by a distributed spring-damper system in radial, circumferential and axial direction.

Another non-linear elastic ring tyre model was developed by Sugiyama and Suda, 2009. Their model is capable of assessing dynamic characteristics of tyres in high frequency ranges resulting from the interaction to uneven road surfaces. The model uses circumferential and radial springs and dampers that are defined between a flexible belt and a rigid rim to account for the sidewall stiffness of tyres.

The toroidal membrane tyre model is also classified as a flexible ring model (Kilner, 1982).

The commercial FTire and RMOD-K models are also flexible models that have recently been developed. The FTire and the RMOD-K models are computer time intensive and they need a lot of data. Usually, they are used for stochastic vehicle vibrations occurring during rough road rides. These models will also be discussed in the following sections.

2.3.6.1 FTire

The tyre simulation software FTire (Flexible Ring Tire model) was first released in December 1998 (Gipser, 1999). The FTire simulation software is widely used by researchers and is generally accepted as a good tyre model (Gipser, 2007).

The tyre belt is described as an extensible and flexible ring carrying bending stiffnesses, elastically founded on the rim by distributed stiffnesses in radial, circumferential and lateral direction.

The flexible belt is provided with a large number of friction elements (to simulate tread blocks) to define lateral and longitudinal forces generated between the tread and uneven road surface. (Sugiyama & Suda, 2009) These elements are coupled to their neighbours by stiff springs and by bending stiffnesses about both the in-plane and out-of-plane direction, see Figure 2.5. Through these elements normal and frictional forces are generated. Friction functions are used that make distinction between stitching and sliding friction. The flexible belt is modelled using 80 to 200 segments that are coupled by stiff springs and by bending stiffnesses, bending stiffnesses and damping factors that may be calculated using measured static and modal tyre properties (Gipser, 2000). Each element possesses five degrees of freedom, including twist and bending (about circumferential axis) (Pacejka, 2006). This leads to a large number of degrees of freedom even for a single tyre model. The model is accurate up to about 150 Hz that correspond to almost all the first bending modes of flexible belt. This corresponds to road obstacle enveloping properties with a wavelength of minimum of 5 cm that can be modelled.

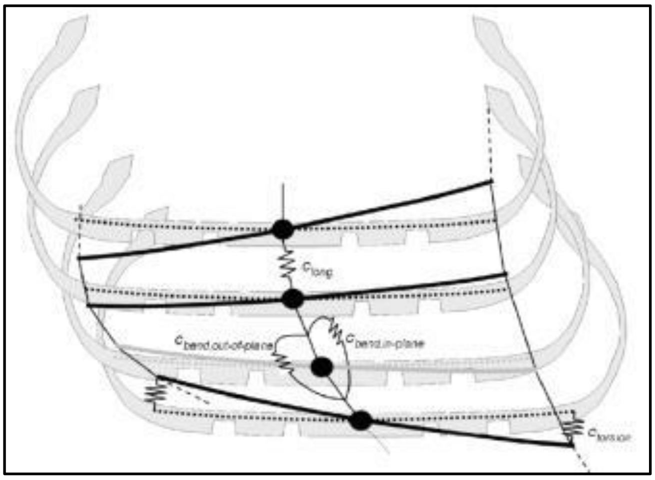

Figure 2.5: Some force elements between adjacent belt elements and rim (Gipser, 2007)

The contact patch contour and pressure distribution follow from the model's flexible properties. FTire can deal with large and/or short-waved obstacles. It works for simulations up to complete stand-still (Gipser, 2000). Parameterisation may be conducted using cleat test data, through estimation schemes or by calculations with *FETire*, a finite element detailed tyre model.

A simplified, rigid belt model is available for much faster computations but limited to 100Hz and relatively smooth roads with wavelengths larger than twice the contact patch length. (Pacejka, 2006)

2.3.6.2 RMOD-K

The model *RMOD-K* was developed by Oertel and Fandre (1999). A detailed finite element description of the actual tyre structure can be defined as shown below in Figure 2.6.

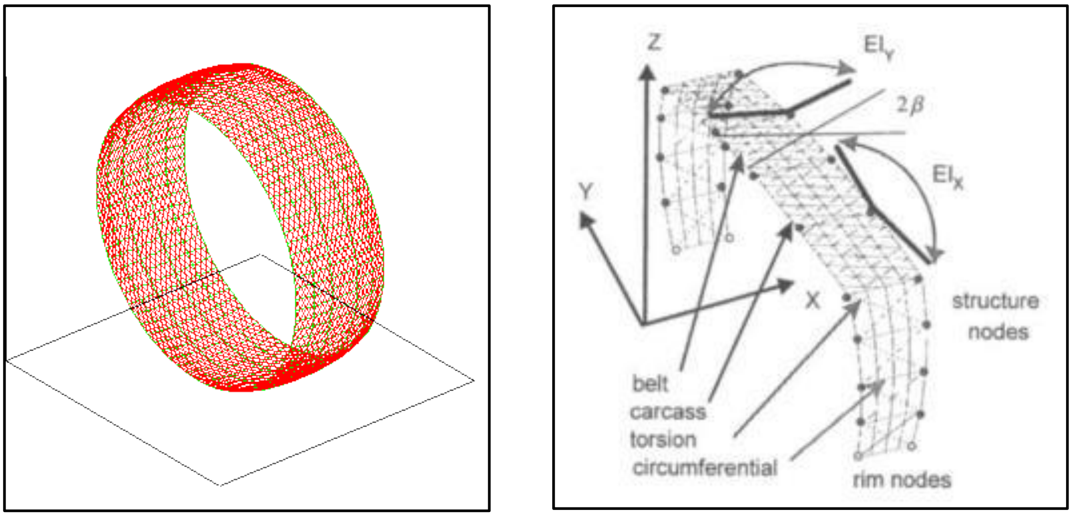

Figure 2.6: RMOD-K finite element structure representation. Belt mesh and complete cross-section element is shown on the right. (RMOD-K, 2011), (Pacejka, 2006)

Unlike the FTire model, RMOD-K uses a detailed finite element description for modelling the flexible tyre belt. The discretized flexible belt is connected to a rigid rim using circumferential and radial springs and dampers in a way similar to SWIFT and FTire models. (Sugiyama & Suda, 2009)

The system consists of two model groups with different modelling approaches to meet different requirements for tyre simulation. The driving dynamics model can be used when short wavelength disturbances can be neglected. For this model, the belt may be represented by rigid body modes only. In the case of short wavelength disturbances however, normal contact has to be calculated from the model itself. The rigid belt model is no longer valid. The tyre must be modelled using a deformable dynamic structure. Different approaches can be used, ranging from a simplified elastic beam to complex FE models. FE models will give accurate results, but it is too slow in the field of vehicle dynamics and ride comfort. (Oertel & Fandre, 1999)

The contact module contains gap sensors on the outer tyre surface. Sensor points are used to calculate the normal and frictional forces. The contact area, with possible gaps, and pressure distribution result from the rolling and compressed model calculations. (Pacejka, 2006)

In the longitudinal direction, contact forces may result from sticking or sliding which is determined from the friction value, the normal contact force, the sliding velocity and the stick/slip state monitor.

The normal force distribution is calculated using the gap sensor information and the tread stiffness. (RMOD-K, 2011)

Furthermore, friction models are included that allow the generation of both adhesion and sliding areas with friction levels that depend on temperature and contact pressure.

Since detailed finite element description is used in this model, the computational effort is much higher than that of the other tyre models discussed up to this point. (Sugiyama & Suda, 2009)

Forces from inflation pressure as well as from contact are loading the structure. At the nodes, extra bending ties are used to support the structure and to account for rubber stiffness. (Pacejka, 2006)

The most recent version of this model is the RMOD-K 7, which features a flexible belt that is connected to the rim with a simplified, pre-processed, sidewall model with pressurised air. (Pacejka, 2006) The model is designed to concentrate on the main effects like the preload giving tensile stresses in the structure and the kinematics of the belt and sidewall structure. The computational effort and accuracy can be scaled according to the type of application: from fully FE to hybrid and discretised structure representations. By specifying the choice of elements and other meshing operations (as the number of sidewall nodes), the models properties can be adjusted to the required conditions. The structure is represented by discrete finite elements based on a main cross section. The belt is modelled by one or more layers that interact with each other. There are different rebar elements used in the belt and sidewall area. The main stiffness results from the rebar elements, which are planar elements with a variable number of rebar elements used inside.

An interface between RMOD-K and ADAMS can simply be done using GFORCE and STRING statements. Adams is a multibody dynamics simulation software equipped with Fortran and C++ numerical solvers. GFORCE parameters are the MARKER IDs that define the rim base and switches controlling the choice of data files and integration method in ADAMS. STRING parameters are simply filenames of terrain and tyre data files. (Oertel & Fandre, 1999)

2.3.7 Finite elements models (FEM)

Finite element modelling of tyres dates back to 1973, when the journal *Tire Science and Technology* was established. (Zorofski, 1973) Finite element analyses are commonly used to calculate dynamic forces in tyres. (Nakashima & Wong, 1993; Darnell, et al., 1997; Ghoreishy, 2008)

Tyres have apparently symmetrical shapes, which may suggest the use of two-dimensional models. But the applicability of two-dimensional models is limited to cases in which the applied loads remain in the tyre meridional plane. These include forces due to application of inflation pressure, rim mounting, etc. Three dimensional models are required to achieve accurate and complete results for dynamic behaviour. (Ghoreishy, 2008) The profile of the tyre can be obtained by measuring the tyre dimensions and importing it into a finite element package. A CAD model can be used to update the model as required. (Korunovic, et al., 2008) The results of the axisymmetric analysis can be transferred to a 3D model. This would imply that the 3D model is built on the basis of the deformed axisymmetric model.

An accurate tyre model is needed when developing an accurate vehicle model. (Mc Allen, et al., 1996; Orteu, 2009; Ghoreishy, 2008; Mohsenimanesh, et al., 2009) The major functions of a tyre include handling, steering, traction, braking, and ride. Each of these functions plays a critical role in vehicle performance. In order to obtain an accurate tyre model for dynamic multibody simulations extensive tests must be performed in order to obtain all of the necessary information and parameters to properly characterize a tyre for vehicle dynamics studies.

The modelling of the composite cord-rubber structural components is still an area where little research has been done. The main problem of these components in the tyre is the non-linear properties and stresses in these areas. Recently, the rebar element approach has gained popularity in the modelling of the composite structures of tyres. (Korunovic, et al., 2007; Lee, 2011)

A non-linear 3D finite element (FE) tyre model, which considers the structural geometry, the anisotropic material properties of the multiple layers and the nearly incompressible property of the tread rubber block was also recently developed (using ANSYS). The element type used in the model for analysing the belt and carcass layers is SOLID 46, which has layer thickness, material direction angles, and orthotropic material properties (ANSYS, 2007). The element possesses three degrees of freedom at each node; translations along the nodal x, y and z directions. The properties of the nylon, steel belts, rubber, etc. were built into the respective layers defined in the SOLID 46 elements. (Mohsenimanesh, et al., 2009)

The nature and the complexity of a tyre model depend on the type of analysis. It is common practice in tyre finite element models found in the literature to only model circumferential grooves in tread. Previous studies showed (Ghoreishy, 2009) that if the main purpose of the tyre analysis is to study the global behaviour of the tyre such as determining the load-deflection curve, a finite element model with simply ribbed tread is sufficient. A finite element model of the tyre with detailed tread pattern is only needed when accurate computations of the stress and strain fields as well as contact pressure are studied. Simply ribbed tread still gives almost identical results for lumped variables such as tyre deformation and dynamic radius.

Most of the detailed finite element models of tyres in the recent literature use linear 8-node hexahedral (cubic) elements (Nakashima & Wong, 1993; Tönük & Ünlüsoy, 2001; Yan, et al., 2002; Hölschner, et al., 2004; Korunovic, et al., 2007; Korunovic, et al., 2008; Ghoreishy, 2009). Different areas of the tyre model can be modelled using different properties, e.g. tread, outer and inner belts, carcass, sidewall, bead, filler and bead bundle can each have its own properties assigned to. The most important factors that influence contact area and contact pressure distribution are the tyre inflation pressure and the tyre structure. (Xia, 2011)

Finite element models can be evaluated using footprint analysis, contact stresses, load deflection curves, etc. Three dimensional FE models remain complex however, and are therefore time-consuming. They have the capability to simulate full three dimensional description, but requires a large computational effort and are mostly seen as unsuitable for real-time simulations. (Senatore & Sandu, 2011)

Finite element methods are implemented to create a detailed mechanical model. For good accuracy, one has to at least resort to a coarse FE model having already many degrees of freedom. (Pacejka, 2006)

2.3.8 Conclusions from existing tyre models in literature

The characteristics of a tyre are mainly affected by (Abe & Manning, 2009; Lee, et al., 1997):

- the tyre material, construction
- geometry,
- the inflation pressure, and
- the ground/road condition

In this study, the focus is on simulating tyre deformation due to vertical/radial forces (taking material properties and inflation pressure into account). Some existing tyre models were discussed in the previous sections, and validation of the tyre models is given.

From the literature, it is now clear that a tyre is too complex to be modelled as a simple spring for refined dynamic vehicle simulations. Simple brush type models are insufficient for non-linear dynamic simulations. The MF-Swift model is fast and accurate, but it requires various inputs for the Pacejka tyre model.

Three-dimensional uneven road surfaces can be simulated very well with the sophisticated RMOD-K model. The computational effort for this model still remains relatively high (Pacejka, 2006). The FTire model is accurate for frequencies up to about 150 Hz that correspond to most of the first bending modes of flexible belt. Acquiring data input for the FTire can be laborious and time consuming however.

While more simplified approaches using the modelling technique of rigid belt dynamics are limited in frequency and disturbance wavelength, approaches using multipurpose finite element codes suffer from very large computational effort in building and assembling stiffness matrix elements regardless to their contribution to the total tyre stiffness.

Empirical methods for tyre modelling have facilitated the development of soil compaction technology and are beneficial to off-road vehicle development. However, analytical methods oversimplify the dynamic soil/wheel or soil/tyre interactions. The finite element method has the capability of modelling the tyre/terrain interaction in a very detailed manner without using many simplified assumptions in the model, especially on the dynamic contact part. (Xia, 2011)

The objective of developing different tyre models is to gain an understanding of the limitations and suitability of the various models. This includes understanding the final objective of the tyre model, the capabilities of different tyre models as well as the cost and availability of data to determine the model parameters.

The aim of this study (as indicated in the diagram in Figure 2.4) is to develop a tyre model that is less complex than conventional detailed FE models that can still maintain the same level of accuracy of conventional FE models.

2.4 Optical measuring techniques

2.4.1 Stereo photogrammetry

Photogrammetry can be defined as the practice of obtaining geometric properties of objects from photographic images at two different viewpoints. When images are used to estimate the three-dimensional coordinates of points on an object, the technique is called stereo photogrammetry.

Three-dimensional coordinates can be determined using two or more photographic images taken from different positions. Common points are identified on each image and three-dimensional locations of points can be determined using triangulation. (Orteu, 2009)

2.4.2 Digital image correlation

The shape variation of an object can be measured and tracked using a sequence of stereo images. However, in experimental mechanics, we are generally interested in the surface strain field due to deformation of an object. Digital image correlation (DIC) can be implemented to accomplish this task. DIC processes have evolved substantially the past few decades. The greatest advantage of this technique is that there is no contact between the measured object and the measuring equipment. This method tracks a stochastic pattern on a sample surface and uses a non-contact optical correlation method to measure full-field displacements.

In the early stages of DIC, it was used to measure deformation on the surface of a planar object, using one camera to image the object. The basic concept used in the DIC process is the comparison of two images of a surface. One image is usually taken of the surface in its undeformed state. This image is commonly referred to as the “reference image”. The following images of the surface measured are commonly referred to as “deformed images”. Several images can be captured in an experiment. These images are then correlated to follow the specimen’s deformation as a function of time. (Daly, 2010)

The measured specimen/sample must be covered with a stochastic pattern. After the images are taken, it is digitized into a distribution of pixel intensities. Local distributions of pixel intensities (“subsets”/”facets”) are then matched by the software. An example of such a pixel distribution is shown below in Figure 2.7.

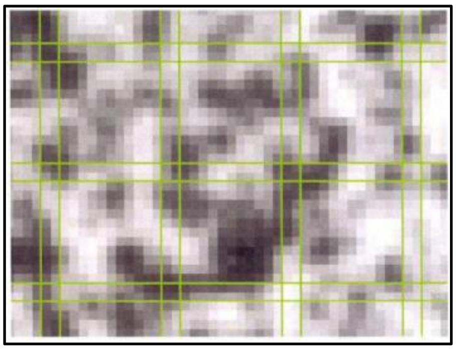

Figure 2.7: 15x15 facets with 2 pixels overlapping

To obtain a close match of facets, one needs to use a correlation function. The function S (shown below) is commonly used to obtain a displacement field by comparing how well two subsets match (Daly, 2010):

$$S\left(x,y,u,v,\frac{\partial u}{\partial x},\frac{\partial u}{\partial y},\frac{\partial v}{\partial x},\frac{\partial v}{\partial y},\right)=1-\frac{\sum[F(x,y).G(x^*,y^*)]}{[\sum F(x,y)^2.\sum G(x^*,y^*)^2]^{1/2}} \qquad [2.3]$$

The variable $F(x,y)$ denotes the grey value at point (x,y) in the undeformed (reference) image and $G(x^*,y^*)$ denotes the grey value at point (x^*, y^*) in the deformed image. The aim of the function is to find values of u, v, $\partial u/\partial x$, $\partial u/\partial y$, $\partial v/\partial x$ and $\partial v/\partial y$ that minimize the correlation coefficient (S). The variables u and v are the subset displacements along the x and y axes, and the gradients represent a measure of the subset distortion. (Daly, 2010)

Point correspondences between two images that were taken at the same instant has to be determined using DIC. The strain field can then also be computed using finite element software. (Orteu, 2009)

After calibration is successfully completed, point correspondences between the “reference” and the “deformed” stereo pair images can be determined using DIC, and the displacement field for each set of images can then be calculated using the calibration parameters. (Daly, 2010)

2.4.5 Commercial computer programs used for DIC

Aramis is a powerful non-contact optical 3D measuring system that was developed by *GOM mbH*. (GOM Optical Measuring Techniques, 2007) Deformation and strain fields of complex materials and structures can be calculated and analysed using Aramis. Aramis recognizes a surface pattern (as shown in Figure 2.7) on a measuring object from digital stereo images and allocates coordinates to the pixels.

Pontos was also developed by GOM mbH (GOM Optical Measuring Techniques, 2008). It can be used to analyse, compute and document an object’s deformations, rigid body movements and the dynamic behaviour. Pontos identifies the dynamic, synchronized and accurate position of an unlimited number of measuring markers (reference points) in 3D space. (GOM Optical Measuring Techniques, 2008)

Aramis and Pontos can both be implemented to do measurements of tyre geometry, full-field deformation profiles upon different loading conditions, etc.

2.4.6 Applications to tyre Testing

The displacements of points on samples of the sidewall and on the tread of the tyre are recorded using Pontos v6.2 as shown in Chapter 3.2.

DIC techniques can be used to measure surface displacements and strains on the sidewalls of tyres (Kostial, et al., 2007; Moser, et al., 2010; Moser & Lightner, 2006). Full-field non-contact measurements are conducted in this study using Aramis v6.1 as shown in Chapter 3.3.

2.5 Material properties

Samples were cut out of different parts of the tyre studied as shown in Figure 3.6 and Figure 3.7. The samples consist of composite materials which has anisotropic material properties. A few aspects of anisotropic materials are discussed in the following sections.

2.5.1 Poisson ratios of anisotropic materials

Poisson's ratio ν(**n**, **m**) of an elastic solid for any two specified orthogonal unit vectors **n** and **m** is the ratio of the lateral contraction in the direction **m** to the axial extension in the direction **n** due to a uniaxial tensile of the material along the direction **n** (Ting & Chen, 2004). The Poisson's ratio for isotropic materials does not depend on the choice of **n** and **m** and is bounded between −1 and 0.5 for the material to be stable (stemming from the necessary positive definiteness of the strain energy density) (Kohlhauser & Hellmich, 2012). A Poisson ratio of 0.5 would imply that the material is incompressible.

By contrast, Poisson's ratio for an anisotropic elastic material does depend on the choice of **n** and **m.** On a microscopic level, most materials are anisotropic. All anisotropic material properties can be attributed to a "mechanism" that exists within the material. A composite material consisting of rubber and steel is a good example of a material where an internal mechanism is present. Any of the six Poisson's ratios in anisotropic materials can exceed 0.5. It is then required that some of the other Poisson's ratios are correspondingly lower, so that overall the condition of total volume being either constant or increasing on deformation is met (Purslow, 2011). It is proven in various articles that the Poisson ratio of anisotropic materials can have no bounds (Boulanger & Hayes, 1998; Ting & Chen, 2004; Ting, 2004). Anisotropic materials may have very large Poisson's ratios (Ting, 2004).

2.5.2 Orthotropic material properties

Materials with different properties in different directions are called anisotropic. The composite tyre material has non-linear stiffness, due to the rubber characteristics. It also has different material properties in the orthogonal directions due to the orientations of the steel, nylon and polyester components in the tyre material. Materials that have two or three mutually orthogonal planes or axes of symmetry where material properties are independent of the direction within each plane are called orthotropic.

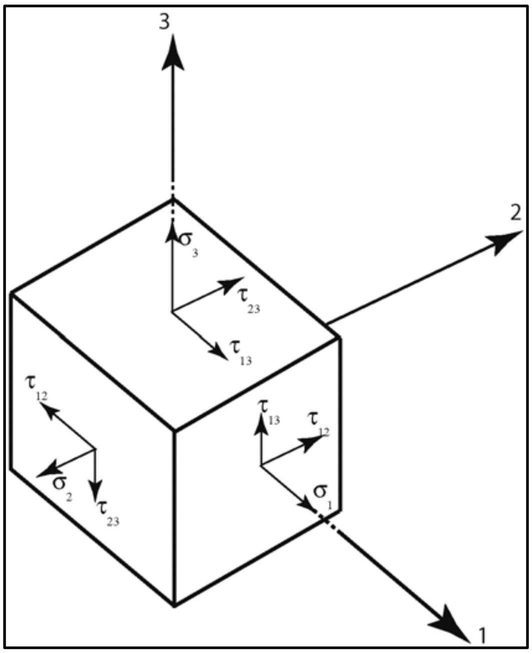

Figure 2.8 An infinitesimal element showing the stresses (Voyyiadjis & Kattan, 2005)

The stresses on a small infinitesimal element are shown in Figure 2.8. There are three normal stresses σ_1, σ_2, and σ_3, and three shear stresses τ_{12}, τ_{23}, and τ_{13}. These stresses are related to the strains ε_1, ε_2, ε_3., γ_{12}, γ_{23}, and γ_{13} as follows:

$$\begin{Bmatrix} \varepsilon_1 \\ \varepsilon_2 \\ \varepsilon_3 \\ \gamma_{23} \\ \gamma_{13} \\ \gamma_{12} \end{Bmatrix} = \begin{bmatrix} 1/E_1 & -\nu_{21}/E_2 & -\nu_{31}/E_3 & 0 & 0 & 0 \\ -\nu_{12}/E_1 & 1/E_2 & -\nu_{32}/E_3 & 0 & 0 & 0 \\ -\nu_{13}/E_1 & -\nu_{23}/E_2 & 1/E_3 & 0 & 0 & 0 \\ 0 & 0 & 0 & 1/G_{23} & 0 & 0 \\ 0 & 0 & 0 & 0 & 1/G_{13} & 0 \\ 0 & 0 & 0 & 0 & 0 & 1/G_{12} \end{bmatrix} \begin{Bmatrix} \sigma_1 \\ \sigma_2 \\ \sigma_3 \\ \tau_{23} \\ \tau_{13} \\ \tau_{12} \end{Bmatrix} \qquad [2.4]$$

In equation 2.4, E_1, E_2 and E_3 are the Young's moduli of elasticity along the 1, 2 and 3 directions respectively. The Poisson's ratios are represented by ν_{ij} (i,j = 1,2,3), while G_{12}, G_{23} and G_{13} are the shear moduli. (Voyyiadjis & Kattan, 2005)

Equation [2.4] can be written in a compact form as follows:

$$\{\varepsilon\} = [S]\{\sigma\} \qquad [2.5]$$

where $\{\varepsilon\}$ and $\{\sigma\}$ represent the 6 x 1 strain and stress vectors, respectively, and [S] is called the compliance matrix. The inverse of the compliance matrix [S] is called the stiffness matrix [C] and is given as follows:

$$\begin{Bmatrix} \sigma_1 \\ \sigma_2 \\ \sigma_3 \\ \tau_{23} \\ \tau_{13} \\ \tau_{12} \end{Bmatrix} = \begin{bmatrix} C_{11} & C_{12} & C_{13} & 0 & 0 & 0 \\ C_{21} & C_{22} & C_{23} & 0 & 0 & 0 \\ C_{31} & C_{32} & C_{33} & 0 & 0 & 0 \\ 0 & 0 & 0 & C_{44} & 0 & 0 \\ 0 & 0 & 0 & 0 & C_{55} & 0 \\ 0 & 0 & 0 & 0 & 0 & C_{66} \end{bmatrix} \begin{Bmatrix} \varepsilon_1 \\ \varepsilon_2 \\ \varepsilon_3 \\ \gamma_{23} \\ \gamma_{13} \\ \gamma_{12} \end{Bmatrix} \qquad [2.6]$$

This equation can also be written in compact form:

$$\{\sigma\} = [C]\{\varepsilon\} \qquad [2.7]$$

The elements of [C] can be calculated using the Matlab function *OrthotropicStiffness*, which is written specifically for this purpose:

$$C_{11} = \frac{1}{S}(S_{22}S_{33} - S_{23}S_{23}) \qquad [2.8]$$

$$C_{12} = C_{21} = \frac{1}{S}(S_{13}S_{23} - S_{12}S_{33}) \qquad [2.9]$$

$$C_{22} = \frac{1}{S}(S_{33}S_{11} - S_{13}S_{13}) \qquad [2.10]$$

$$C_{13} = C_{31} = \frac{1}{S}(S_{12}S_{23} - S_{13}S_{22}) \qquad [2.11]$$

$$C_{33} = \frac{1}{S}(S_{11}S_{22} - S_{12}S_{12}) \qquad [2.12]$$

$$C_{23} = C_{32} = \frac{1}{S}(S_{12}S_{13} - S_{23}S_{11}) \qquad [2.13]$$

$$C_{44} = \frac{1}{S_{44}} \qquad [2.14]$$

$$C_{55} = \frac{1}{S_{55}} \qquad [2.15]$$

$$C_{66} = \frac{1}{S_{66}} \qquad [2.16]$$

$$S = S_{11}S_{22}S_{33} - S_{11}S_{23}S_{23} - S_{22}S_{13}S_{13} - S_{33}S_{12}S_{12} + 2S_{12}S_{23}S_{13} \qquad [2.17]$$

Since the compliance matrix is symmetric, it should be clear that the material constants appearing in the compliance matrix in [2.4] are not all independent. The following equations relate the material constants:

$$\frac{\nu_{12}}{E_1} = \frac{\nu_{21}}{E_2} \qquad [2.18]$$

$$\frac{\nu_{13}}{E_1} = \frac{\nu_{31}}{E_3} \qquad [2.19]$$

$$\frac{\nu_{23}}{E_2} = \frac{\nu_{32}}{E_3} \qquad [2.20]$$

These equations are called the *reciprocity relations* for the material constants. From these relations it is now clear that there are nine independent material constants for an orthotropic material. (Voyyiadjis & Kattan, 2005)

2.5.3 Hyper elastic constitutive models

Rubber-like materials exhibit certain stress–strain characteristics called hyper elasticity. Several models are available in the literature for these materials. Ghoreishy (2008) published a very comprehensive review of finite element models of rolling tyres used in the past four decades. The most frequently used formulation for rubber in finite element tyre simulations is the Mooney-Rivlin (first and second order) and Ogden models for hyper elastic materials. These formulations give stable solutions. Other common models used for rubbers are Ogden, Yeoh, neo-Hookean. These models are implemented in several FE commercial codes. (Ghoreishy, 2008; Sasso, et al., 2008; MSC.Software, 2010)

The original first order Mooney-Rivlin model is given by the strain-energy function:

$$W = C_{10}(I_1 - 3) + C_{01}(I_2 - 3) \qquad [2.21]$$

Elastic behaviour of rubber-like materials are often modelled based on the Mooney-Rivlin model. The constants C_{10} and C_{01} are determined by fitting predicted stress values to experimental data. The recommended tests are uniaxial tension, equibiaxial compression, equibiaxial tension, uniaxial compression, and for shear, planar tension and planar compression. Ghoreishy (2009) used the Mooney-Rivlin model to simulate rubber in a finite element tyre model.

The two parameter Mooney-Rivlin model is usually valid for strains up to 100%. (Sasso, et al., 2008) However, it has been found inadequate in describing the compression mode of deformation.

Tschoegl's investigations (Tschoegl, 1971) emphasized the fact that maintaining higher order terms in the generalized Mooney-Rivlin polynomial function of strain energy led to better agreement with test data for rubbers. Some of the models along these lines integrated into MSC.Marc are (MSC.Software, 2010):

The three term Mooney-Rivlin equation is given by:

$$W = C_{10}(I_1 - 3) + C_{01}(I_2 - 3) + C_{11}(I_1 - 3)(I_2 - 3) \qquad [2.22]$$

The Neo-Hookean model:

$$W = C_{10}(I_1 - 3) \qquad [2.28]$$

which is a special case of the Mooney-Rivlin form, with $C_{01} = 0$. The model uses a single modulus ($2C_{01} = G$), and gives good correlation for experimental data up to 40% strain in uniaxial tension.

The Ogden Model:

$$W = \sum_{n=1}^{N} \frac{\mu_n}{\alpha_n} ({\lambda_1}^{\alpha_n} + {\lambda_2}^{\alpha_n} + {\lambda_3}^{\alpha_n} - 3) \qquad [2.29]$$

J is the Jacobian measuring dilatancy, defined as the determinant of deformation gradient F ($J = \lambda_1\lambda_2\lambda_3$). The Neo-Hookean and Mooney-Rivlin material models can be considered as special cases from the Ogden model. This model is implemented in MSC.Marc, and gives good correlation with test data in simple tension up to 700%.

2.5.4 Superimposed finite elements

Different non-linear material properties cannot be defined in different orthogonal directions for hexahedral (brick) elements in MSC.Marc but another set of non-linear isotropic elements can be defined and superimposed onto it. Non-linear material properties will thus have to be determined that closely simulate the tyre’s material properties in conjunction with the linear orthogonal properties of the second set of element. If only the nodes are equivalence and not the elements itself, the two sets of element will be able to simulate combined material properties.

The sidewall, for instance does not have any steel wires or materials lined up in the circumferential direction. In this case the non-linear material properties of the rubber will be represented solely by the first set of elements and a Youn’g modulus of zero will be given to the second set of elements in this direction. In the radial direction however, the polyester wires are embedded in the rubber (as described in Chapter 3.1). An additional stiffness can thus be added to the second set of orthogonal elements by defining a Young’s modulus in this direction. If the stiffnesses of the two set of elements are summed together on a stress-strain curve, the resulting stiffness should then be closely representative of the global material properties (rubber and embedded polyester) of the sidewall in the radial direction. A similar approach will also be followed for the tread of the tyre.

The use of elements with equivalent homogeneous properties is investigated (instead of inserting rebar elements or using layered composite elements to simulate the different materials in the tyre structure individually). In order to compensate for different stiffnesses caused by the steel wires, polyester and nylon threads between the rubber in the carcass and tread of the tyre, two sets (non-linear isotropic elements end linear orthotropic elements) of 8-noded hexahedral elements (see Figure 2.9) will be superimposed onto each other.

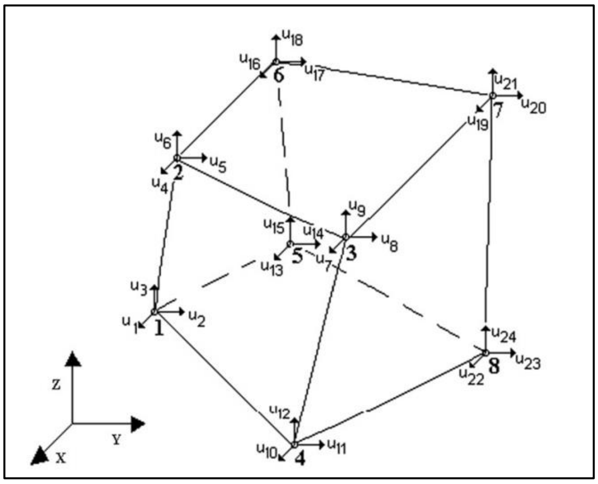

Figure 2.9: Hexahedral (8-noded brick) element (Cerrolaza & Osorio, 2012)

3 Experimental measurement of tyre properties

3.1 The tyre studied

The tyre used for the study is a Continental tyre (CONTI TRAC AT). The investigation of this tyre can give insight on the behaviour of off-road tyres. The tyre used in this study was a 235/85 R 16 110S tyre:

235 = Section width of the tyre in millimeters.

85 = Aspect ratio between the section height and section width in %.

R = Construction of the tyre; radial ply tyre.

16 = Diameter of the rim in inches.

110 = Load index: the maximum nominal wheel load is 10’400 N.

S = Speed rating: the maximum velocity is 180 km/h.

3.2 Material characteristics of the tyre

The tyre was cut open using a hacksaw and a utility knife. Samples were also cut out of different parts of the tyre studied as shown in Figure 3.6 and Figure 3.7. The following observations were made.

A steel cord is present where the tyre makes contact with the rim. The sidewall consists of rubber with 2 plies of polyester threads embedded into the rubber (see Figure 3.1). The sidewall thickens at the shoulder, where it meets the tread area. The tread of the tyre consists of 6 plies (2 Polyester, 2 steel, 2 Nylon), embedded into the rubber, of which the orientations are shown in Figure 3.2. The steel cords are at 26° with the longitudinal direction, while the nylon threads are lined up along the circumference of the tyre. The polyester threads are oriented 90° with the nylon threads.

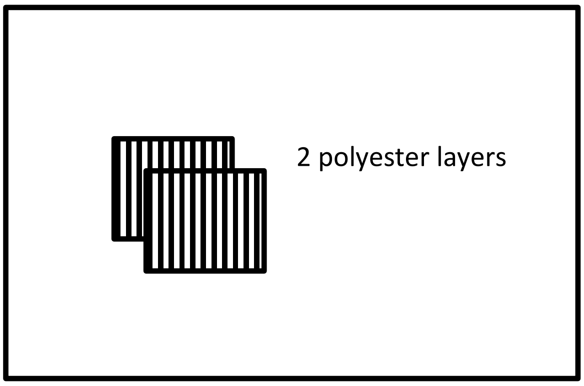

Figure 3.1: Stacking of plies in the sidewall

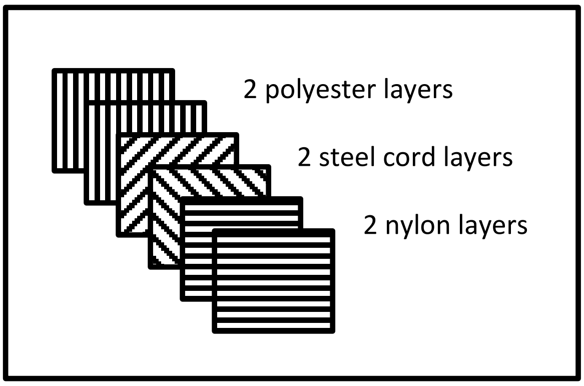

Figure 3.2: Stacking of plies in the tread

Modelling all the detail of the different plies present in the tyre as well as the bonds between the different materials will result in a very complex model that will not solve fast enough for dynamic simulations. Since gathering data of the exact material properties of each ply (steel wires, bead fillers, nylon wires, etc.) and all the different rubber materials in the tyre are also time consuming, the use of large elements with equivalent homogeneous properties is investigated. The tyre will be divided into different regions with similar material properties.

In order to obtain an estimate how many different kinds of rubber is present in the tyre, a Shore durometer is used. This estimate gives insight into how many different regions the tyre structure must be divided into for the purpose of this study.

3.2.1 Shore Hardness Tests

Durometers are commonly used to measure hardness in polymers, elastomers and rubbers. The durometer used to measure the hardness of the rubbers in the tyre is a Shore D Hardness Tester TH210 (Figure 3.3).

Figure 3.3: TH210 Shore D Durometer

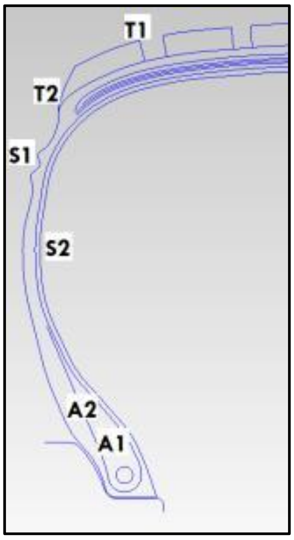

Figure 3.4: Regions measured on the tyre for Shore D hardness

Different regions of the tyre are measured, using the durometer, as shown in Figure 3.4. For each region, 6 samples are used, and an average of three readings is tabulated in Table 3.1 for each sample. The average of the 6 samples for each region is then calculated to obtain an estimate of the hardness of the rubber.

Table 3.1: Shore D hardness readings

Region	Description of region	Sample no.						AVG of 6 samples
		1	2	3	4	5	6	
A1	**Apex (beside bead)**	23.3	24.1	26	23	24.9	24.8	**24.4**
A2	**Apex (15mm from bead)**	26.3	23.3	24.5	25.2	26.2	24.1	**24.9**
S1	**Sidewall (measured inside)**	21.2	16.4	16.3	17	20.2	17.6	**18.1**
S2	**Sidewall (sidewall, outside)**	17.7	15.6	16.3	16	16.1	15	**16.1**
T1	**Tread**	32.2	30.3	31.3	32.4	32.9	32.7	**32.0**
T2	**Side of tread**	16.7	16.6	17.8	20.3	17	16.6	**17.5**

From the results listed in Table 3.1 it was concluded that the sidewall of the tyre mostly consists of the same rubber. The apex region is made of harder rubber, while the rubber in the tread blocks is the hardest.

Figure 3.5 shows a sectioned view of the tyre on the left. The tread will be considered as one region with homogeneous material properties. The rubber in the sidewall is softer and will be considered as a second region. The bead wire consists of a steel rope (about 10 mm in diameter). The bead filler (also called the apex) consists of a harder rubber than the rubber in the sidewall. A third region is thus defined in the tyre structure (which will be referred to as the bead region for the purpose of this study) to simulate the stiffness caused by bead wire and the bead filler material.

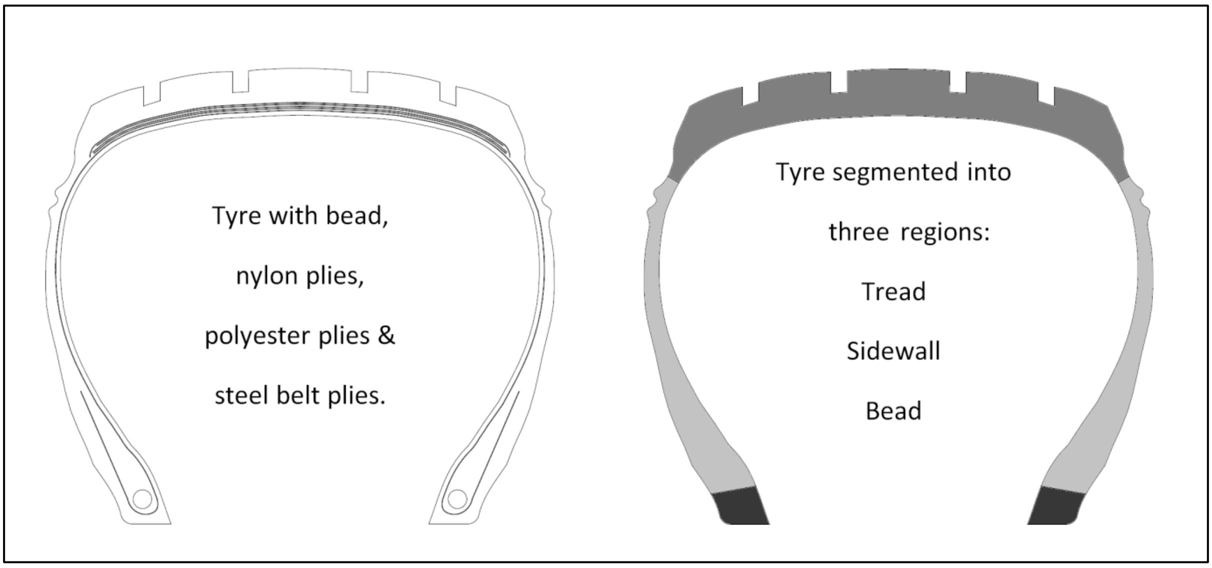

Figure 3.5: Sectioned view of tyre showing nylon, polyester & steel belts (left) and the segments that the tyre is divided into (right).

3.2.2 Tensile tests on segments of the tyre

In order to obtain an accurate FE model of the tyre, the material properties of the tyre regions first had to be determined. Tensile tests were performed to characterize the global material properties of the regions in its respective orthogonal directions.

A water jet cutting machine was used to cut segments out of the tread, sidewall and apex of the tyre, as seen in Figure 3.6. This method of obtaining samples for uniaxial tension tests was also used previously by Kondé, et al., 2013.

Figure 3.6: Segments of the tread and sidewall being cut using a water jet cutting machine

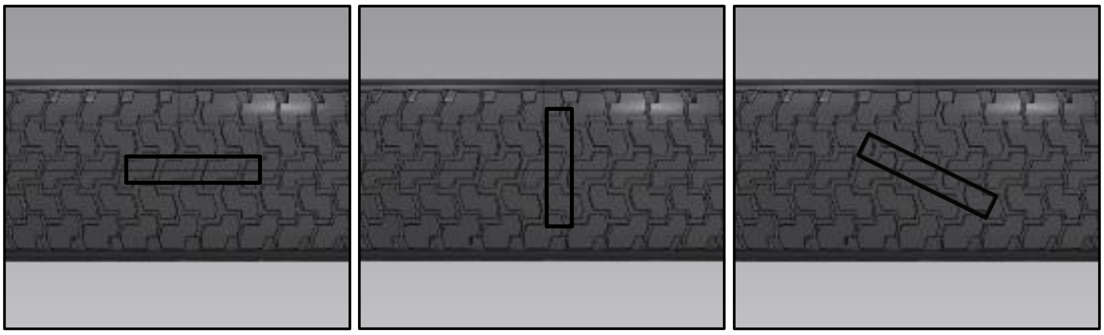

Figure 3.7: Three different samples cut out of the tread area, from left to right, longitudinal, lateral, diagonal (26 degrees)

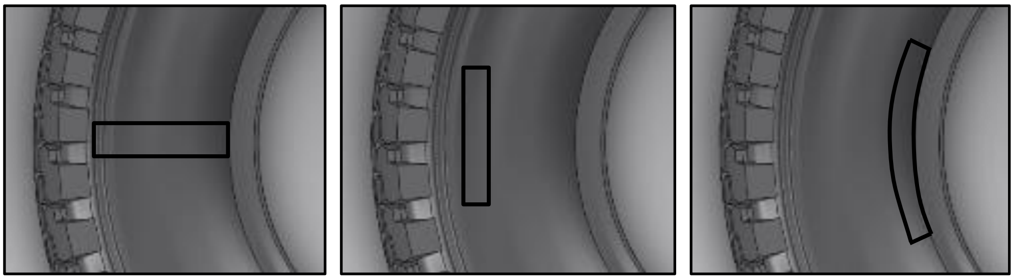

Figure 3.8: From left to right, sidewall radial sample, sidewall circumferential sample, apex sample

As demonstrated in Figure 3.7 to Figure 3.9, tensile tests were done on six different segments of the tyre. On the tread, longitudinal and lateral samples are cut. Samples are also cut diagonally (26° from the longitudinal direction, in line with the steel wires). Radial and circumferential samples were taken from the sidewall and samples of the apex region were also tested.

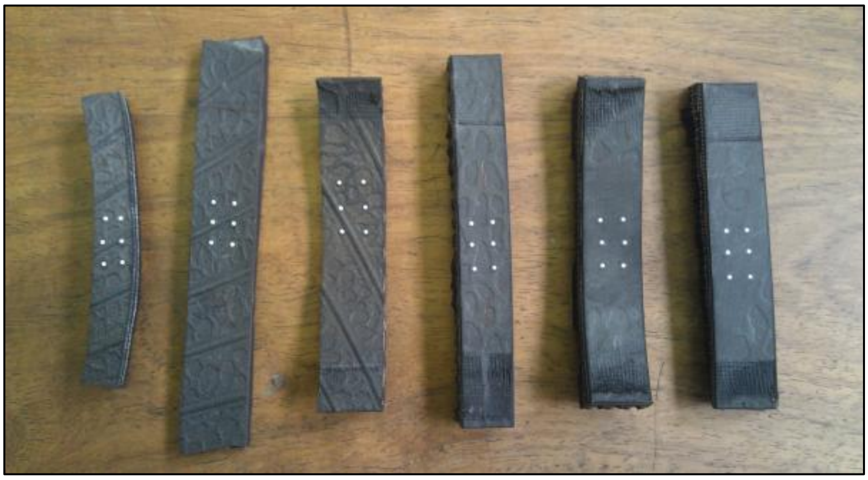

Figure 3.9: Sections cut from the tyre for tensile testing. From left to right, Apex, Sidewall (circumferential), Sidewall (radial), Tread (longitudinal), Tread (lateral), Tread (diagonal)

The engineering stress in the samples was obtained from tensile tests, by dividing the measured force by the initial cross-sectional area of the samples (tabulated in Table 3.2).

$$\sigma = \frac{F}{A_i} \qquad [3.1]$$

Table 3.2: Cross section of samples

	Thickness (mm)	Width (mm)	Cross sectional area (mm^2)
Sidewall - Circumferential	6.5	25	162.5
Sidewall - Radial	6.5	25	162.5
Apex - Radial	15	15	225
Tread - lateral	11	25	275
Tread - longitudinal	11	22	242
Tread - diagonal	11	25	275

The strain in the vertical direction (in line with the length of the samples) was calculated using the displacements of the white dots on the samples. An average of the deformation was calculated at each time interval, using Equation 3.2, and the engineering stress for the samples was plotted against the strain.

$$\boldsymbol{\varepsilon = \frac{\Delta L}{L} = \frac{l-L}{L}} \qquad [3.2]$$

The sample cross section dimensions are listed in An additional load cell is used (as shown in Figure 3.10) to record the load together with the stereo photogrammetry data of the samples (shown in Figure 3.9). The measured load is then imported into GOM Pontos as an external input signal whiles the deformation of the samples is measured using the stereo photogrammetry images. The displacement of the dots (as seen in Figure 3.9) is calculated using Pontos software. The load is then plotted against the strain obtained using Pontos software. The results are shown in Figure 3.11 to Figure 3.16.

An EZ50 (50 kN) Universal Materials Testing Machine was used to perform the tensile tests as indicated in Figure 3.10. The loads applied to the samples were recorded using the EZ 50's software.

As the samples were axially extended using the EZ50, the samples became thinner due to the lateral compression. The samples then slip out of the clamps when the deformation measured with the EZ50 becomes large, causing inaccurate measurement of the true extension of the samples. For this reason, the deformation calculated from the stereo photogrammetry images (using DIC) gave a more accurate representation of the deformation of the samples than the EZ50 testing machine output.

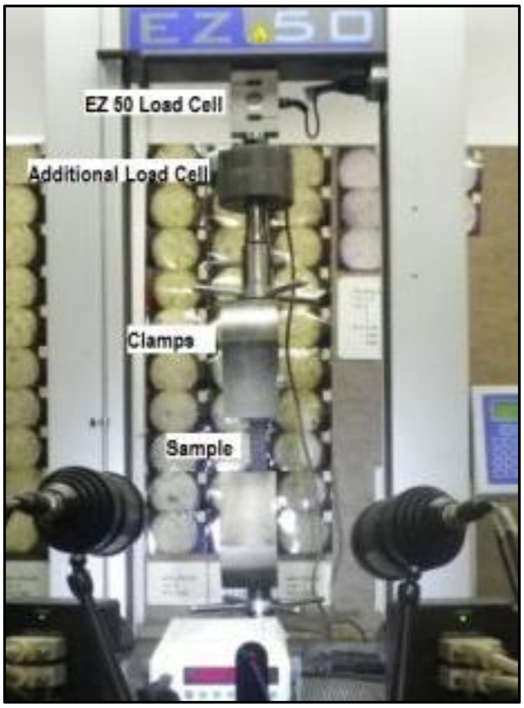

Figure 3.10: Test setup for tensile tests of samples

An additional load cell is used (as shown in Figure 3.10) to record the load together with the stereo photogrammetry data of the samples (shown in Figure 3.9). The measured load is then imported into GOM Pontos as an external input signal whiles the deformation of the samples is measured using the stereo photogrammetry images. The displacement of the dots (as seen in Figure 3.9) is calculated using Pontos software. The load is then plotted against the strain obtained using Pontos software. The results are shown in Figure 3.11 to Figure 3.16.

The stress vs. strain curves show hysteresis which can be attributed to the rubber in the samples. The effect of the hysteresis can clearly be seen in Figure 3.12. On the right hand side of Figure 3.15 one can also see the effect of hysteresis which occurred when the clamps started to loose grip on the samples and it slipped out of the clamps.

The investigation tyre model developed only accounts for quasi-static effects, therefore, the hysteresis effect of the rubber is neglected in this study.

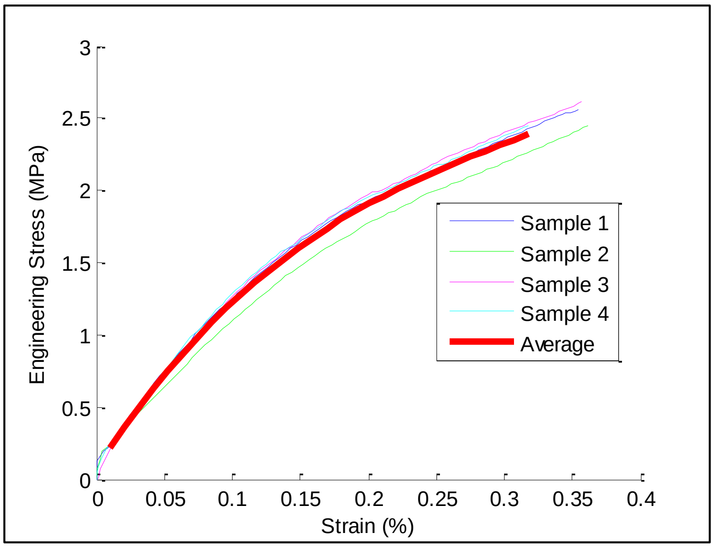

Figure 3.11: Engineering stress vs. strain in the Apex region

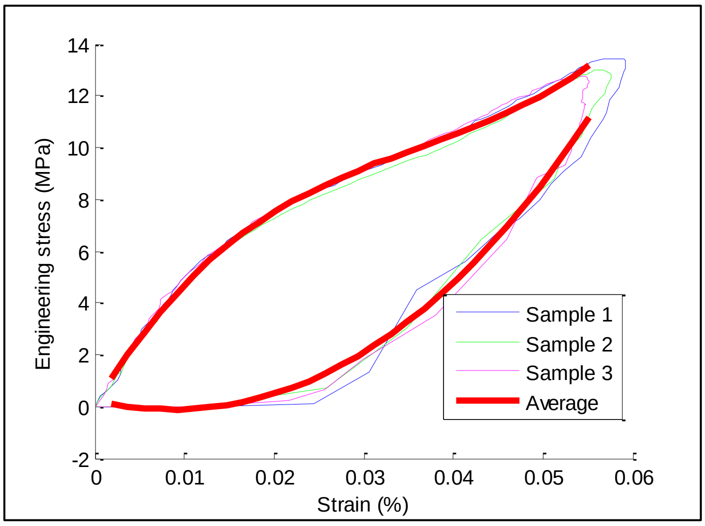

Figure 3.12: Engineering stress vs. strain for the sidewall in the radial direction

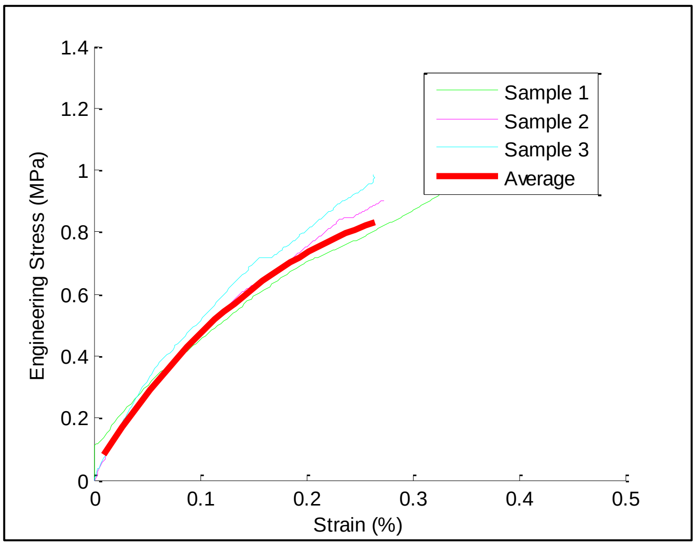

Figure 3.13: Engineering stress vs. strain for the sidewall in the circumferential direction

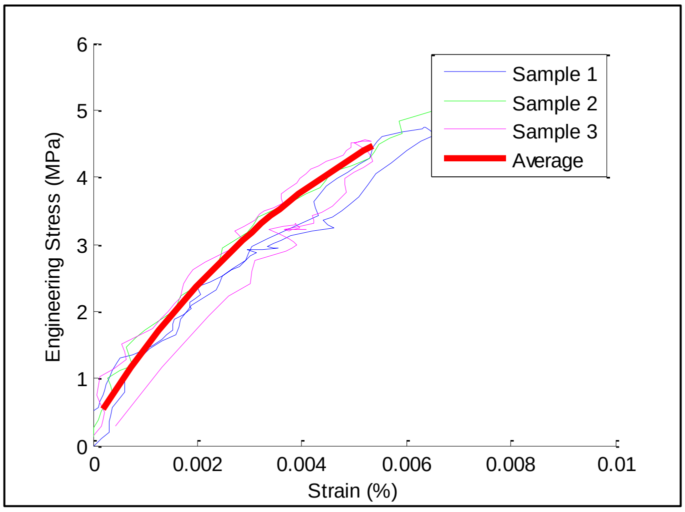

Figure 3.14: Engineering stress vs. strain for the tread, 26 degrees diagonal with the longitudinal direction

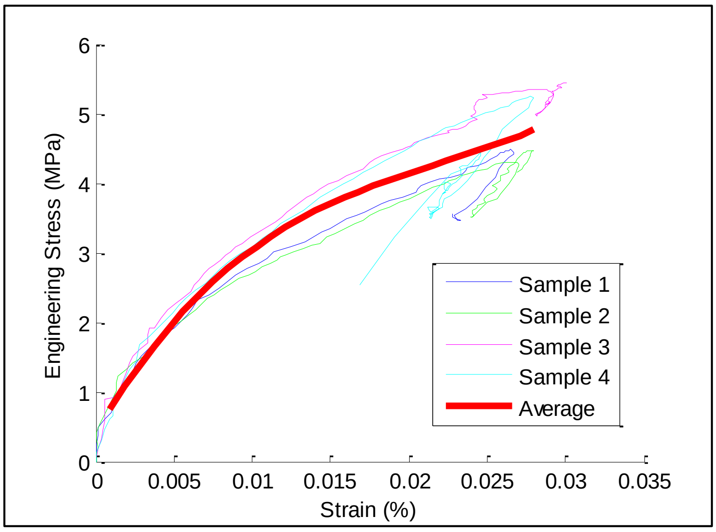

Figure 3.15: Engineering stress vs. strain for the tread in the lateral direction

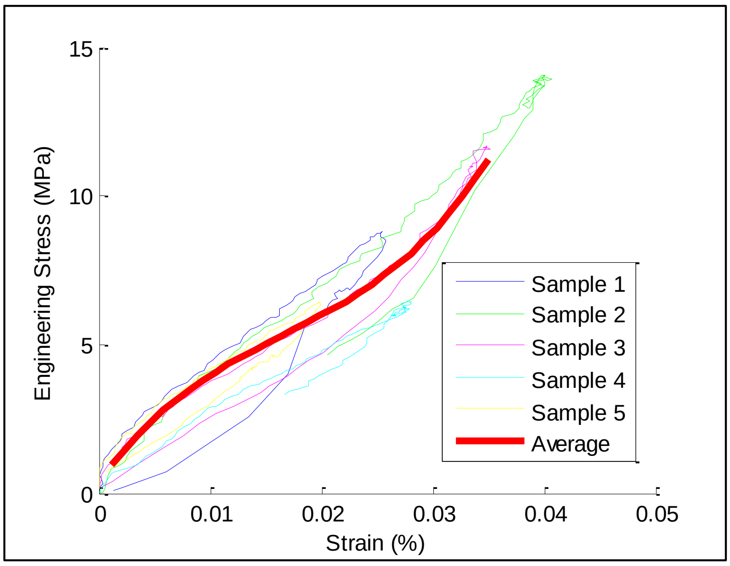

Figure 3.16: Engineering stress vs. strain for the tread in the longitudinal direction

The resolution of the photogrammetry cameras was too low to capture the lateral displacements of the points accurately. Therefore, a digital camera was also used to capture images of the samples. A Matlab program is used to record the positions of the points as they are picked (see Figure 3.17). . The first image is taken when the sample is at zero load and the position of the points on the images with loads applied are determined relative to its original positions. The images were processed using Matlab. The Poisson ratios are then calculated using the deformation values in the different orthogonal directions.

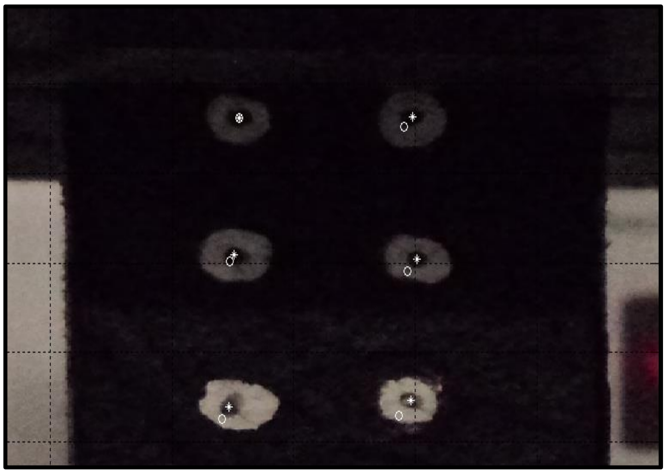

Figure 3.17: Example of photo captured using stereo photogrammetry

Tyres consist of composite materials as one can clearly see in the Young's Moduli and Poisson's ratios obtained in Table 3.3. The Poisson's ratios for the segments of the tyre clearly indicate that the material for both the tread and the sidewall are not isotropic, since Poisson ratios larger than 0.5 are measured.

The reciprocity relations (equations 2.18 – 2.20) are valid for the relationship between the radial and circumferential values for the sidewall and for the relationship between the lateral and longitudinal values for the tread.

The large differences in the Young's Moduli can be explained by the direction of the plies embedded into the rubber in the tyre. In the sidewall the polyester threads are lined up radially. The measured stiffness is thus much larger radially than the circumferential stiffness as expected. Since the polyester threads are lined up radially, it has little influence on the stiffness in the circumferential direction. The Young's moduli for rubbers used in tyres are typically between 0.77 and 7 MPa. (Edeskär, 2004; Koutný, 2007; Drescher, et al., 1999) The Young's modulus in the circumferential direction is measured as 4.98 MPa in the side wall and as 13.45 MPa in the apex region. These values mostly represent rubber stiffness since no threads/wires are aligned with the circumferential direction.

Table 3.3: Material Properties obtained for tyre segments

	Apex Region	Sidewall Radial	Sidewall Circum-ferential	Tread Lateral	Tread Longitudinal
Young's Modulus (MPa)	13.45	490.3	4.98	335.7	432.3
Poisson's Ratio	$\nu_{a-r} = 0.12$	$\nu_{r-t} = 5.05$	$\nu_{t-r} = 0.13$	$\nu_{la-lo} = 0.49$	$\nu_{lo-la} = 0.62$

3.3 Geometry of the tyre

3.3.1 Laser measurement

In order to obtain good finite element results, the geometry of the object needs to be captured as accurately as possible. The tyre needs to be measured, since the complete geometry of the tyre is not made available by the manufacturer. For this purpose an accurate laser displacement transducer (Acuity AR700) and a linear string potentiometer are used to measure the geometry of the tyre. The tyre is put down on a flat surface for measurements. Both the laser displacement transducer and the string potentiometer are mounted on an X-Y platform that is placed over the tyre as shown below in Figure 3.18.

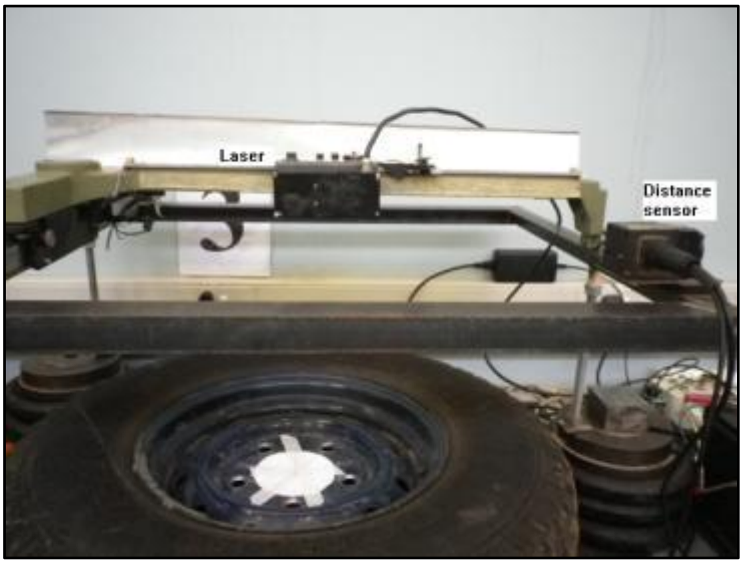

Figure 3.18: Laser profile measurement of the tyre - experimental setup

The Acuity AR700 laser displacement transducer is used to measure the vertical coordinates while the string potentiometer is used to measure the horizontal coordinates (X and Z coordinates of the tyre). The centre of the tyre/wheel is determined, and the profile of the tyre is measured across the tyre centreline.

The Acuity AR700 laser displacement transducer was calibrated using the linear digital scale on a lathe as reference for displacement and a Fluke 117 Multimeter to measure the voltage output of the transducer. The laser displacement transducer gives 20.376 mm/V (see Figure 3.19). The calibration values are verified by taking measurements using a vernier together with the output voltage given by a SOMAT eDaq data acquisition system. An eDaq is a standalone rugged mobile acquisition system designed for lab and field testing as well as unattended monitoring in harsh environments. The string potentiometer is also calibrated using a vernier and the multimeter together with the output voltage given by the eDaq.

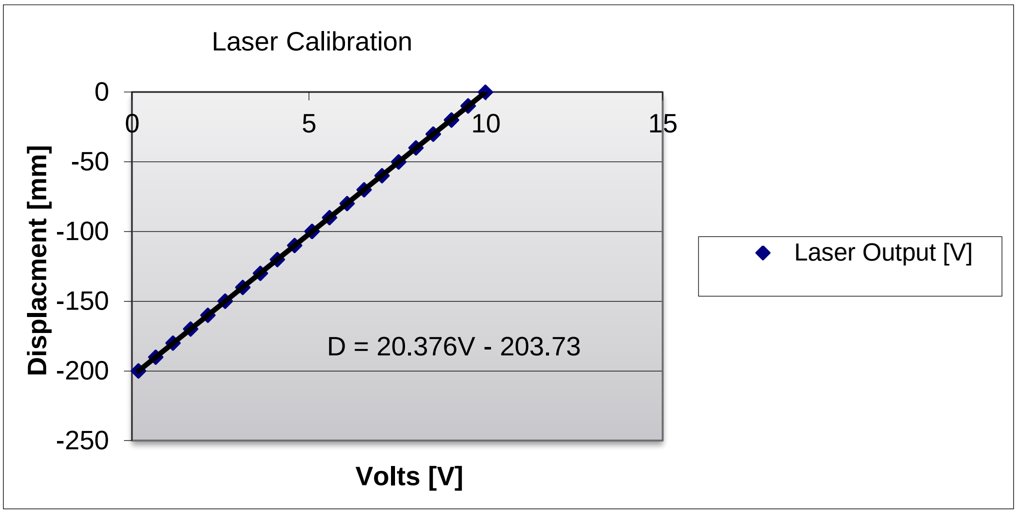

Figure 3.19: Laser calibration

The output voltage signals of the laser and the string potentiometer are captured using the eDaq. The tyre pressure was measured to be 200 kPa during these measurements. Measurements are taken over the diameter of the tyre. First, the laser is moved forward and backwards over the centreline. Thereafter the same is done sideways (90° with respect to the first set of measurements). The results are shown below in Figure 3.20.

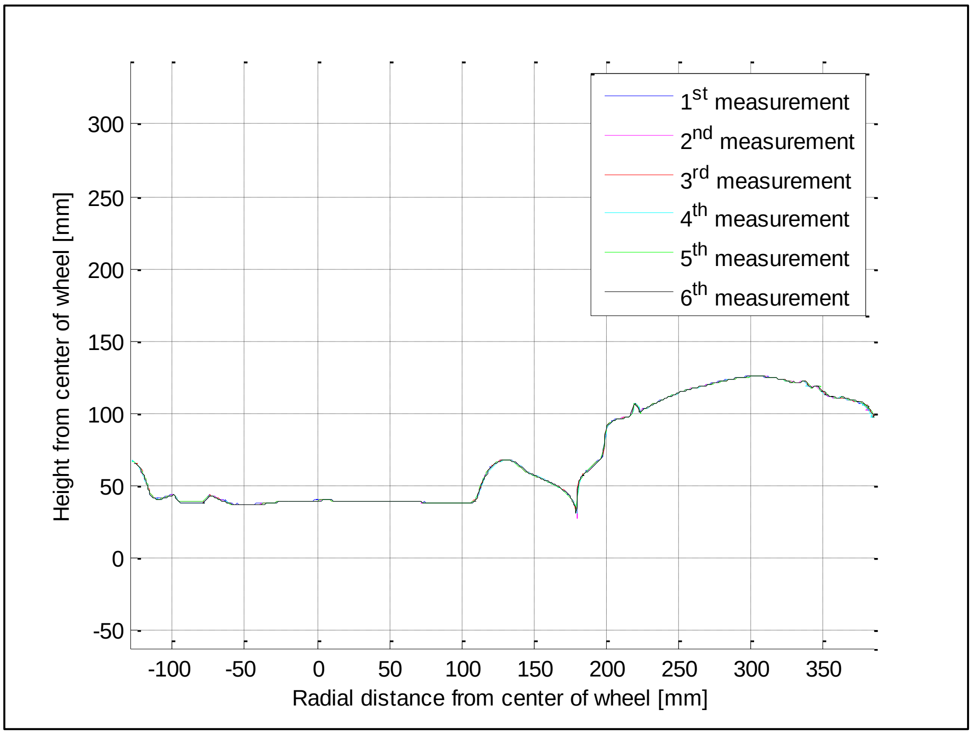

Figure 3.20: Profile measured using laser

The apparent discontinuity between 150 mm and 200 mm in Figure 3.20 is the point where the inside part of the rim is welded to the outside part of the rim and is in fact not a discontinuity. The Root Mean Square (RMS) of the difference between the averaged profile and the actual individually measured profiles is 0.26 mm. The maximum difference between the measured profiles and the average of the profiles is 4.7 mm.

3.3.2 Stereo photogrammetry measurement

To verify that the measurement results obtained with the laser is accurate, stereo photogrammetry was also used to measure the sidewall profile of the tyre.

In order to obtain good results the tyre had to be prepared for measurements first. The sidewall was made smooth. Letters on tyre sidewall were removed using a hand grinder. The surface was then treated with a thin layer of silicon-based glue to make it even smoother.

The surface is sprayed with a black and white stochastic, random pattern. With tyre pressure still at 200 kPa, a picture is taken with the tyre mounted in front of the cameras. Two high definition cameras are used to do the measurements. The cameras were first calibrated to synchronize them.

After the picture is taken, GOM Aramis (GOM Optical Measuring Techniques, 2007) is used to process the results. The sidewall profile is then imported into Matlab to be compared with the measurements described in the preceding section. The blue and red points on the profile in Figure 3.22 indicate the data points obtained using GOM Aramis. In order to compare the results, it is checked how much each point of the stereo photogrammetry deviates from the laser profile. Red points indicate a high deviation, while blue indicate zero deviation. From Figure 3.21 it can be seen that it is only at the shoulder of the tyre that the measurements differ up to about 5 mm. This can be ascribed to the tread blocks at the shoulder of the tyre. The silicon glue could also have attributed to the deviations in the measured profile of the sidewall.

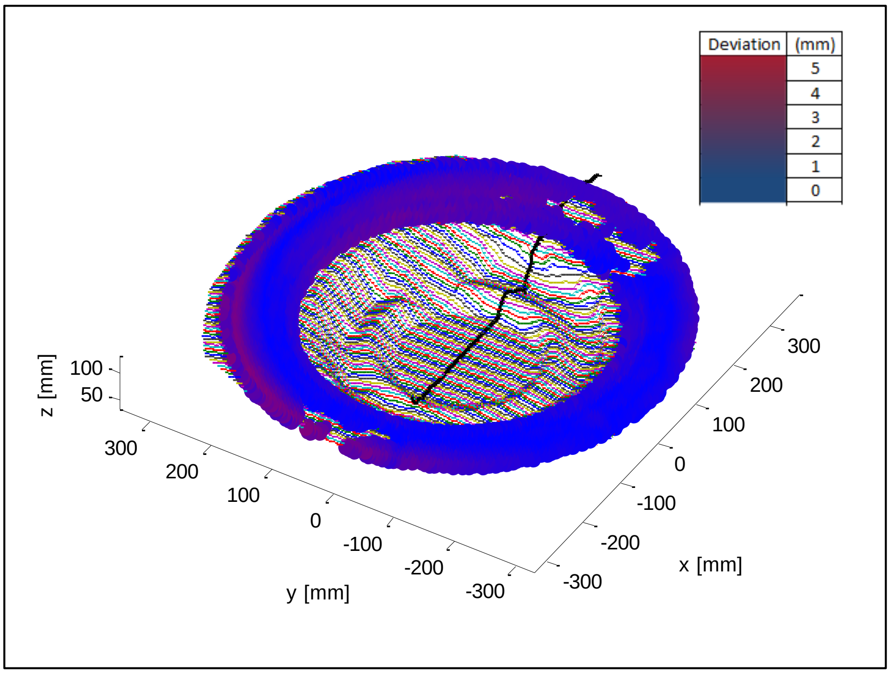

Figure 3.21: Aramis and Laser comparison

The deviations between the laser measurements and the stereo photogrammetry are plotted on a histogram as shown in Figure 3.22. Overall, one can see from these results that good correlation is found between the laser measurements and stereo photogrammetry. The profile obtained using the laser displacement transducers was used to build a 3D model of the tyre.

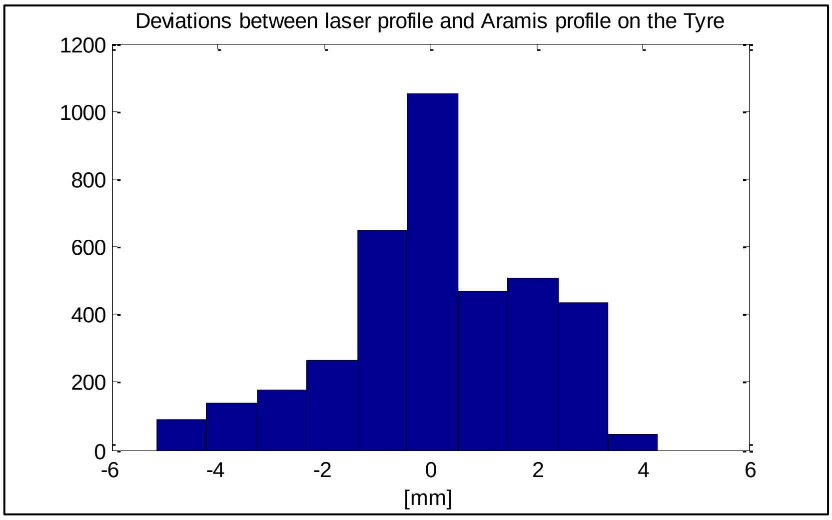

Figure 3.22: Deviations between the measurements obtained using stereo photogrammetry and a profiling laser.

3.3.3 Tread profile measurement

The tread profile of the tyre also had to be measured. The tyre was first mounted together with its rim, to a hub. The hub was mounted to a large solid frame. The instruments needed to measure the tread profile were the following:

- Solid frame for mounting of tyre
- X-Y platform
- Laser displacement transducer (Acuity AR700)
- Shaft encoder (Heidenhain ROD320)
- Linear string potentiometer
- eDaq data acquisitioning system
- A computer
- Battery

The laser was mounted to the X-Y platform together with the string potentiometer. The X-Y platform was then positioned to line up with the centre of the tyre. A spirit level was used to check that the X-Y platform was lined up correctly. The laser was lined up with the centre of the tyre. A spirit level was used to check that the X-Y platform is lined up horizontally.

The experimental setup is shown below in Figure 3.23.

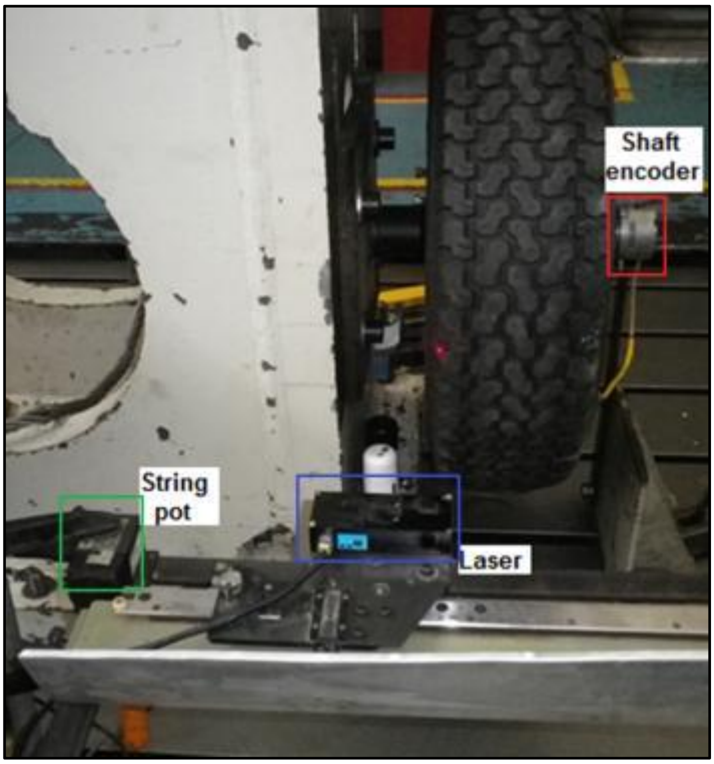

Figure 3.23: Tread profile measurement experimental setup

The tread of the tyre was measured radially using the laser. A shaft was machined to fit onto the centre of the rim. The diameter of the shaft was measured to be 38.9 mm in diameter. A vernier was used as demonstrated in Figure 3.24 to zero the laser at a specific distance from the centre of the wheel.

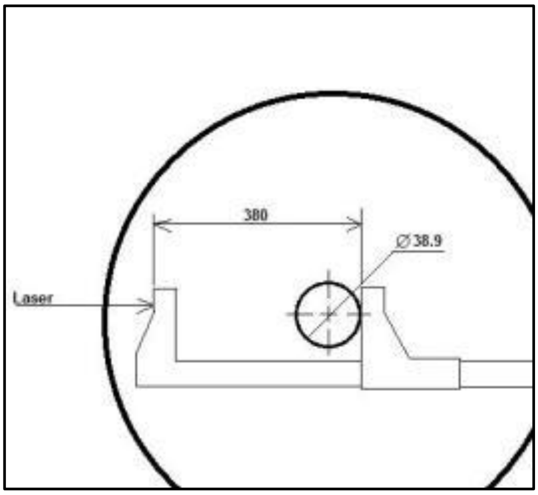

Figure 3.24: Vernier used to zero the laser for radial measurements

The string potentiometer was used to measure the lateral coordinates, the laser to measure the radial coordinates, while the shaft encoder was used to measure the angle while the tyre was rotated. The shaft encoder, laser, and the string potentiometer were connected to the eDaq which was connected to a laptop to read the output signals of the encoders.

The shaft encoder gives a voltage output signal. The signal is a block signal that changes 5000 times per revolution between 0.0 V and 3.5 V. At each change in voltage, coordinates are extracted and then plotted. The tread profile measurements are shown superimposed on the previous plots of the sidewall measurements in Figure 3.25.

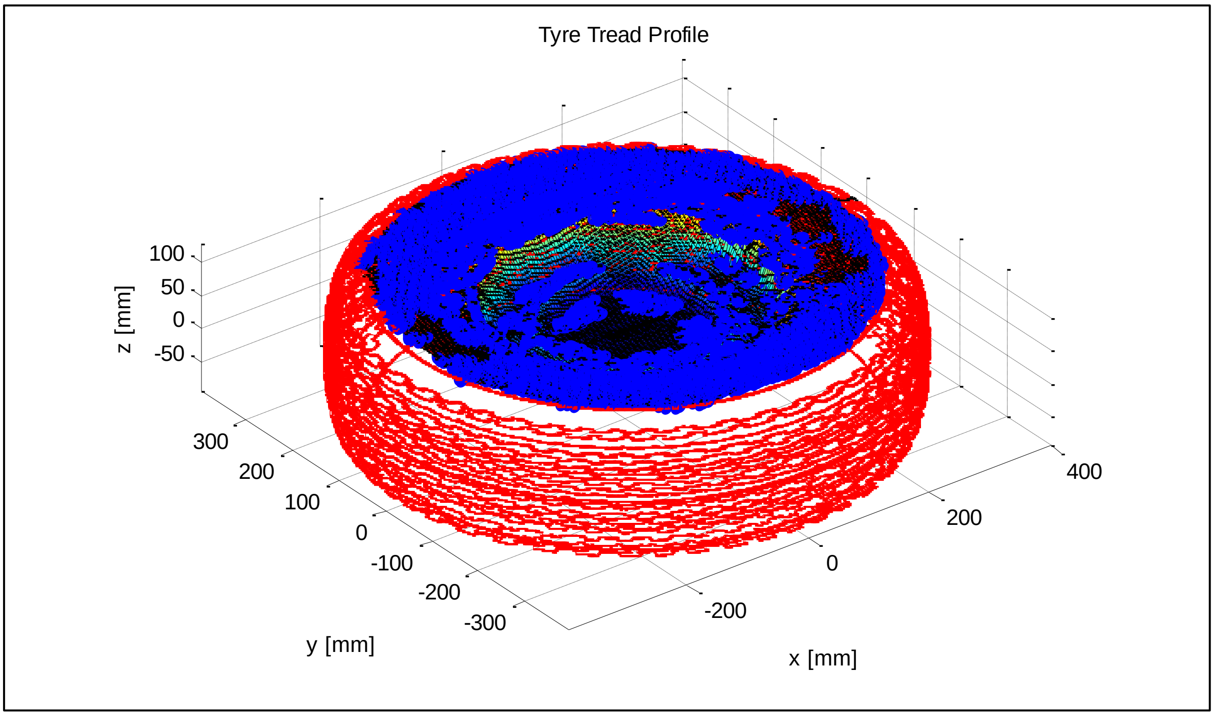

Figure 3.25: Superimposed laser measurements and stereo photogrammetry measurements

3.3.4 Solid Works Model

The geometry measured as described in this chapter is imported into SolidWorks, and a model is constructed from it. A generic tread pattern is generated to match the real tread pattern. The model is shown below in Figure 3.26.

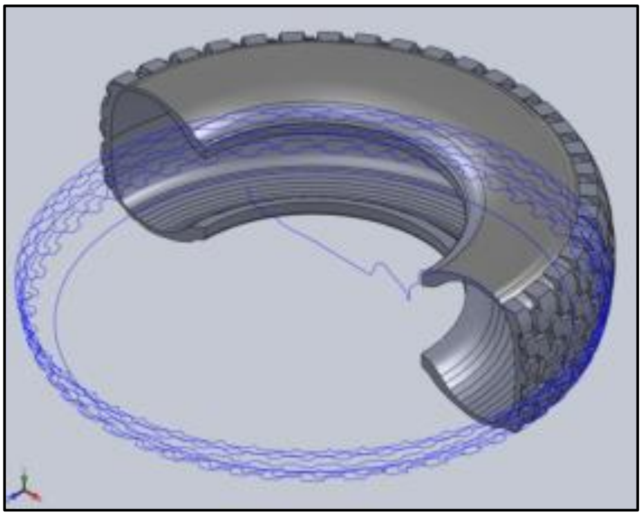

Figure 3.26: SolidWorks model of the tyre studied (shown sectioned with some laser tread and sidewall profiles from measurements)

This geometry is imported as a parasolid file into MSC.Patran for meshing. A finite element model with a simply ribbed tread is developed, using the cross-sectional area of the measured profile (see Figure 3.27). The profile is revolved around the centreline of the tyre and meshed as described in Chapter 4.

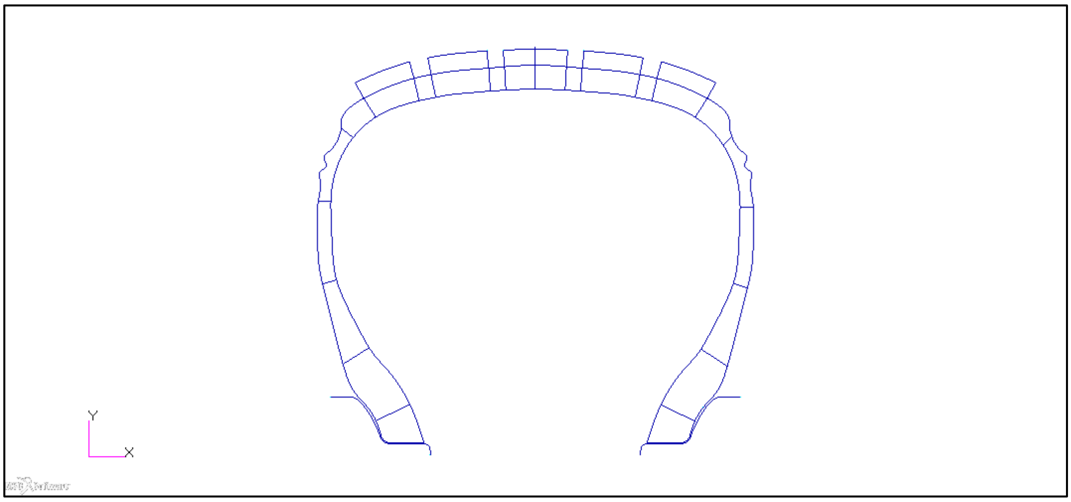

Figure 3.27: Curves imported into MSC.Patran

4 Development of the FE tyre model

Before a FE tyre model of the full tyre could be attempted, it had to be verified if the material properties obtained in Chapter 3 could be successfully incorporated in the FE model. The tensile tests, performed as described in Chapter 3, are replicated in simulation to accomplish this.

4.1 Methodology followed in the tyre segment testing models

Simple models, similar in shape to the tyre segments tested in Chapter 3, are built in MSC.Marc with the same dimensions as the samples tested as described in Chapter 3. The models are constrained at one end, while it is pulled on the other end using a RBE2 connection (The displacement of the nodes on the one surface of the model are dependent of the displacement of the node where the load is applied, shown in red in Figure 4.1 to Figure 4.4) to distribute the applied force evenly across the surface it is applied to. The tyre is modelled using 8-noded hexahedral elements.

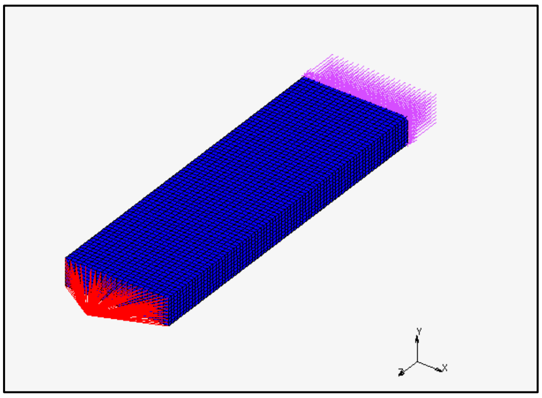

Figure 4.1: Pulling of sidewall sample in the radial direction

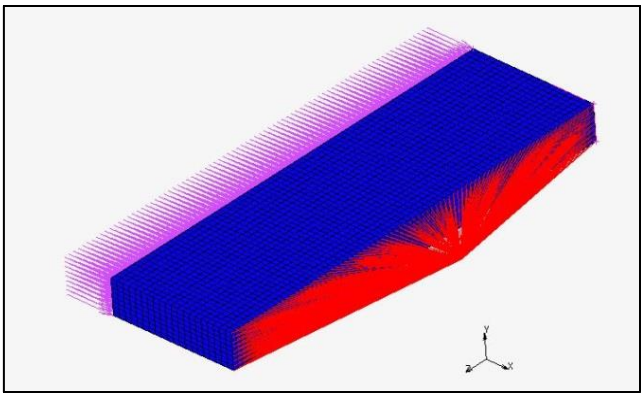

Figure 4.2: Pulling of sidewall sample in the circumferential direction

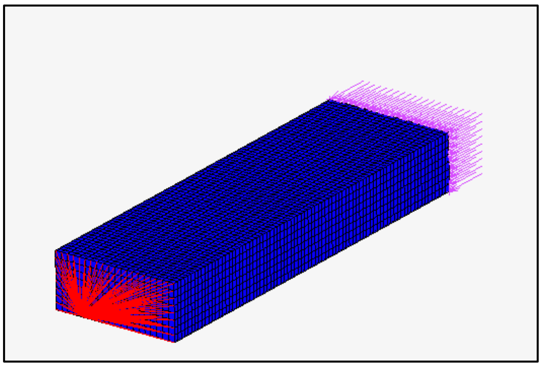

Figure 4.3: Pulling of tread sample in the lateral direction

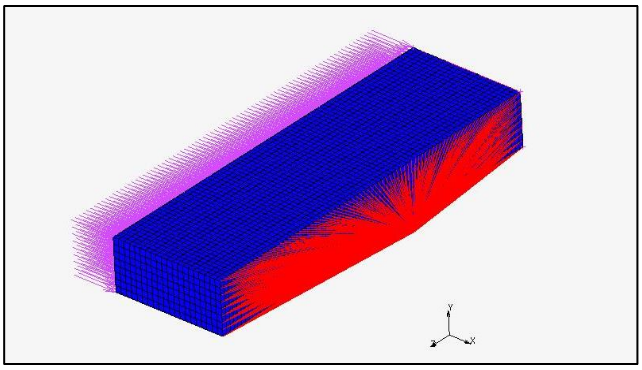

Figure 4.4: Pulling of tread sample in the longitudinal direction

Since the global material properties of the tyre segments differ in each direction, the material properties of the model had to be set up in such a way to have different stiffnesses in the different orthogonal directions. The finite elements in the models consist of two sets of elements superimposed onto each other. The one set of elements contain orthotropic material properties with a linear stiffness in each orthogonal direction. The other set of elements has non-linear isotropic material properties.

The sidewall section of the tyre has 2 plies polyester that lines up with the radial direction. To simulate the material properties of the sidewall, the results from the tensile tests in the circumferential direction (perpendicular to the direction of the polyester) are used for the rubber characteristics in the sidewall. An experimental data fit is obtained using MSC.Marc (shown in Figure 4.5). The Ogden model gave a good fit for the experimental data with two pairs of coefficients. The first coefficient being $\mu_1 = 5.03715e{+}08$, with its corresponding exponent $\alpha_1 = 0.0028661$, and the second coefficient $\mu_2 = 5.52802e{+}08$ with its corresponding exponent $\alpha_2 = 0.00295897$. This defines the non-linear rubber properties of the sidewall region.

To compensate for the extra stiffness in the radial direction (caused by the polyester), another set of elements with orthogonal material properties is superimposed onto the existing non-linear isotropic elements as discussed in Chapter 2.5.3. The orthogonal material properties of these elements are set up using a Young's Modulus of 320 MPa in the radial direction (Stress vs. strain graph shown in Figure 4.6). No stiffness is added in the other two orthogonal directions. The superimposed elements in the model can then use the combined material properties of both the nonlinear isotropic properties and the linear orthogonal properties. Adding the linear orthotropic stiffness to the experimental circumferential stiffness of the sample gives a stress-strain curve that approximates the stress-strain values of the sidewall's radial stiffness as shown in Figure 4.7.

$$\sigma_{\substack{sidewall,radial\\experimental}} \approx \sigma_{\substack{sidewall,tangential\\experimental}} + \sigma_{\substack{Orthotropic\\Young'sModulus=320MPa}} = \sigma_{\substack{sidewall,radial\\approximation}} \qquad [4.1]$$

The Ogden material properties used are defined in the first set of elements to define the non-linear rubber properties in the FE model of the sample. In the second set of superimposed elements, the stiffness due to the polyester is simulated by giving it a Young's Modulus equal to 320 MPa in the radial direction. The summed stiffness of the sidewall in the radial direction then becomes closely representative of the values tabulated in Table 3.3.

$$\sigma_{\substack{sidewall,radial\\FE\ Model}} = \sigma_{\substack{sidewall,tangential\\Ogden\ fit}} + 320\ MPa \cdot \varepsilon \qquad [4.2]$$

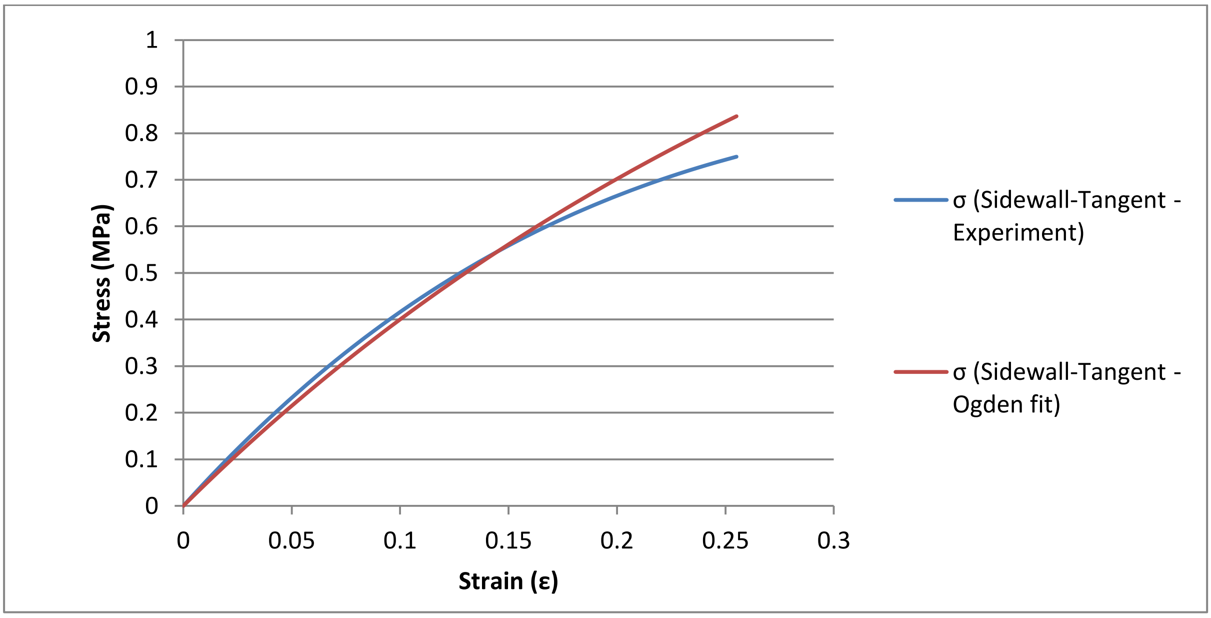

Figure 4.5: Ogden experimental data fit for sidewall rubber

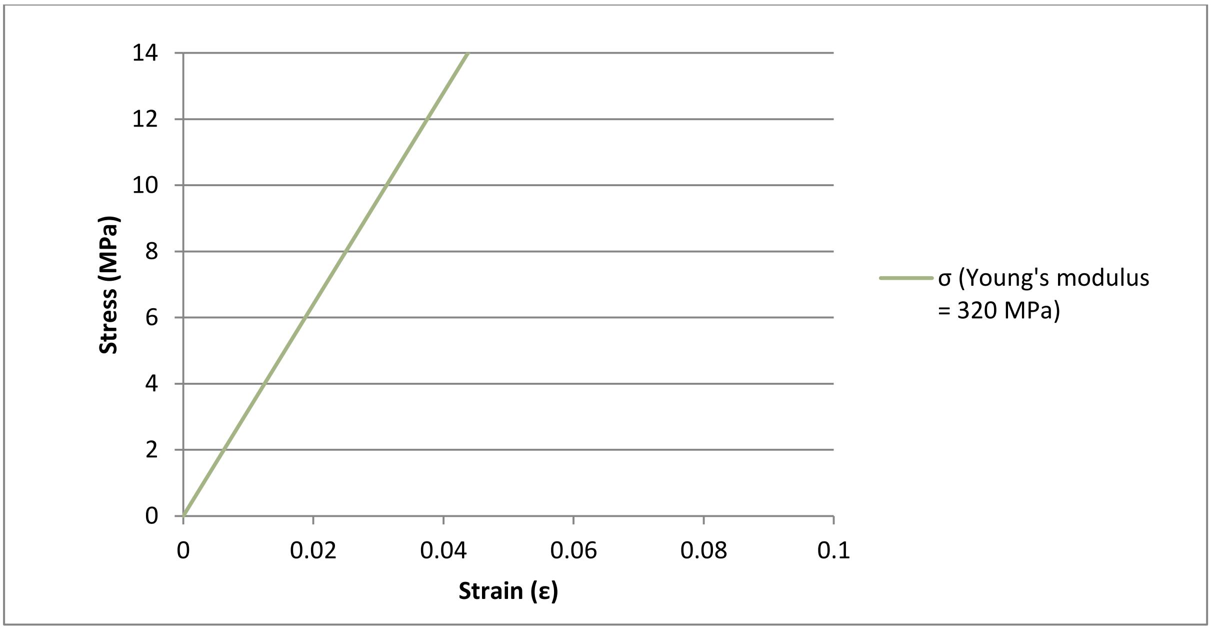

Figure 4.6: Orthotropic stiffness component for sidewall radial stiffness

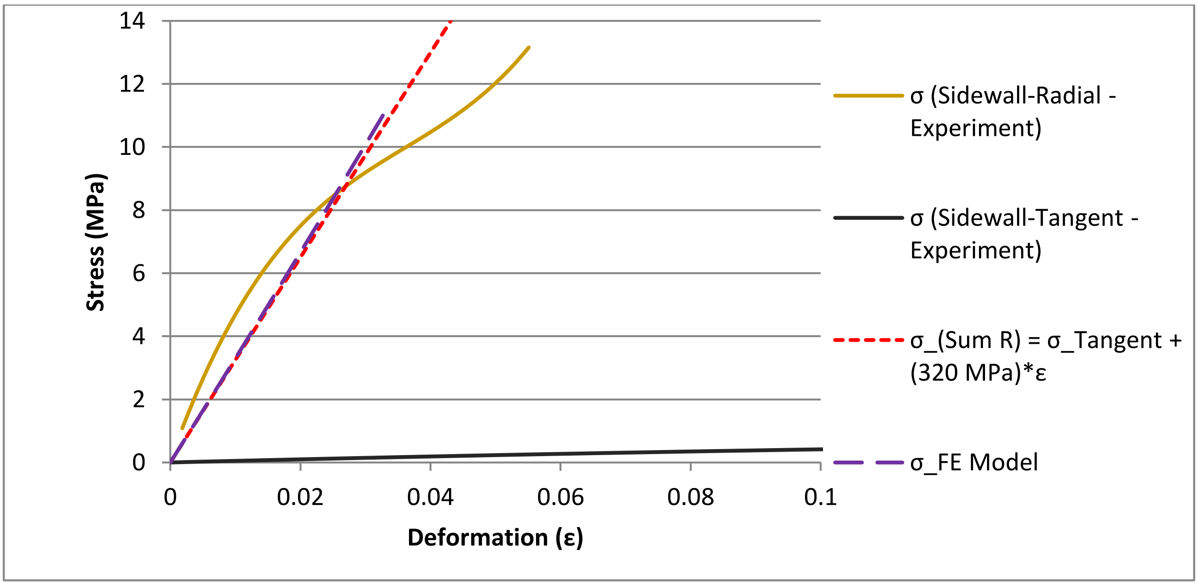

Figure 4.7: Sidewall material properties in radial direction

Figure 4.7 show the experimental values for the stress vs. strain from the tests done on the samples of the sidewall.

The rubber in the tread of the tyre is harder than the rubber in the sidewall, as shown in Table 3.1. Since no tests are done on the tread in the radial direction, the experimental stress-strain values from the tests on the apex region are used. The apex region also consists of a harder rubber, similar to the rubber in the tread region. A Neo-Hookean model with C10 = 1.80282e+06 is used for the elements simulating the rubber in the model (shown in Figure 4.8).

The superimposed orthogonal elements are then used to simulate the effect of the steel wires in the tread. To compensate for the extra stiffness in the lateral and longitudinal directions, another set of elements with orthogonal material properties is superimposed onto the existing non-linear isotropic elements. The orthogonal material properties of these elements are set up with a Young's Modulus of 200 MPa in the lateral direction and 350 MPa in the longitudinal direction (Stress vs. strain graph shown in Figure 4.9 and Figure 4.10). No stiffness is added in the radial direction, since none of the embedded wires line up radially in the tread region. The superimposed elements in the model can then use the combined material properties of both the nonlinear isotropic properties and the linear orthogonal properties. Adding the linear orthotropic stiffness to the experimental circumferential stiffness of the apex sample gives a stress-strain curve that approximates the stress-strain values of the tread's lateral and longitudinal stiffness as shown in Figure 4.11 and Figure 4.12. The summed stiffness of the tread in the lateral direction then becomes closely representative of the values tabulated in Table 3.3.

$$\sigma_{\substack{Tread,lateral\\experimental}} \approx \sigma_{\substack{Apex,circumferential\\experimental}} + \sigma_{\substack{Orthotropic\\Young'sModulus=200MPa}} = \sigma_{\substack{Tread,lateral\\approximation}} \qquad [4.3]$$

$$\sigma_{\substack{Tread,longitudinal\\experimental}} \approx \sigma_{\substack{Apex,circumferential\\experimental}} + \sigma_{\substack{Orthotropic\\Young'sModulus=350MPa}} = \sigma_{\substack{Tread,longitudinal\\approximation}} \qquad [4.4]$$

The Neo-Hookean material properties used are defined in the first set of elements to define the non-linear rubber properties in the FE model of the sample. In the second set of superimposed elements, the stiffness due to the polyester, nylon and steel wires is simulated by giving it a Young's Modulus equal to 200 MPa in the lateral direction and 320 MPa in the longitudinal direction. The summed stiffness of the tread in the circumferential direction then becomes closely representative of the values tabulated in Table 3.3.

$$\sigma_{\substack{Tread,lateral\\FE\ Model}} = \sigma_{\substack{Apex,circumferential\\Neo-Hookean\ fit}} + 200\ MPa \cdot \varepsilon \qquad [4.5]$$

$$\sigma_{\substack{Tread,longitudinal\\FE\ Model}} = \sigma_{\substack{Apex,circumferential\\Neo-Hookean\ fit}} + 350\ MPa \cdot \varepsilon \qquad [4.5]$$

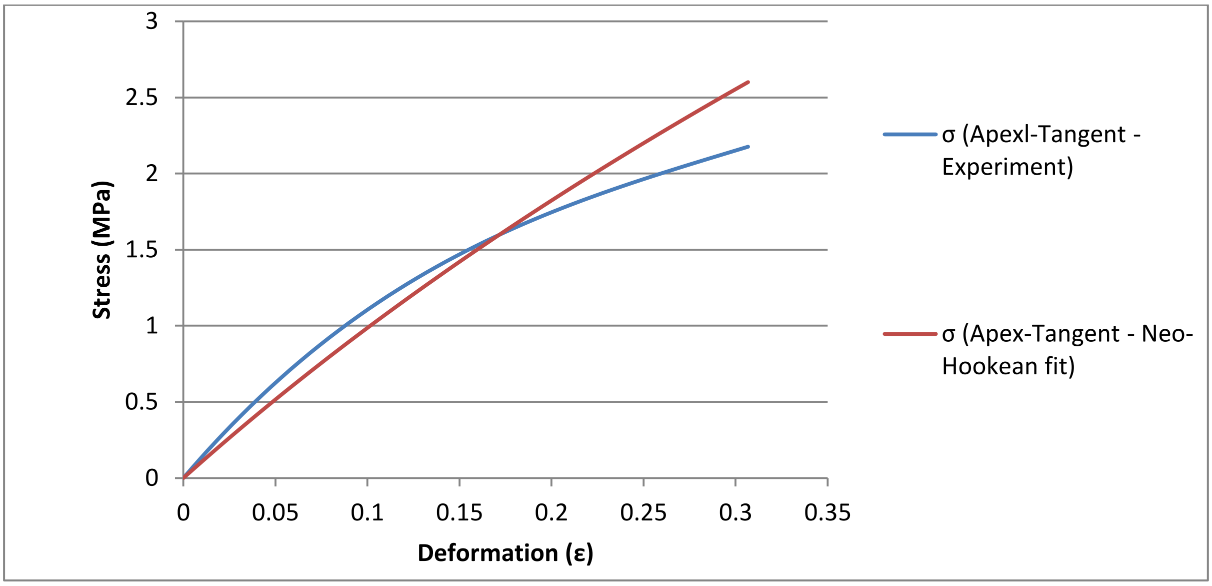

Figure 4.8: Neo-Hookean experimental data fit for tread rubber

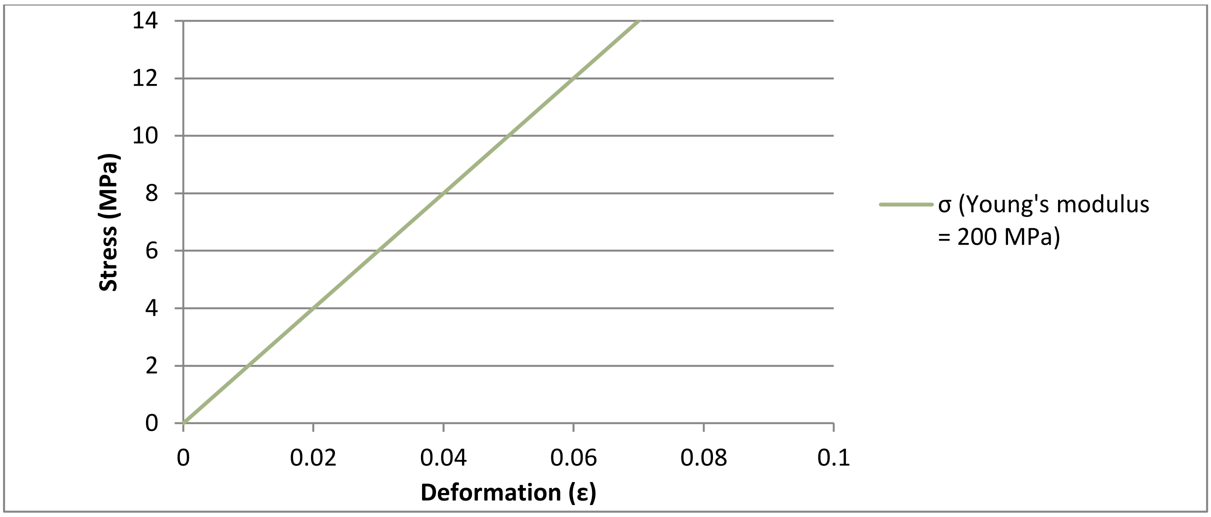

Figure 4.9: Orthotropic stiffness component for tread lateral stiffness

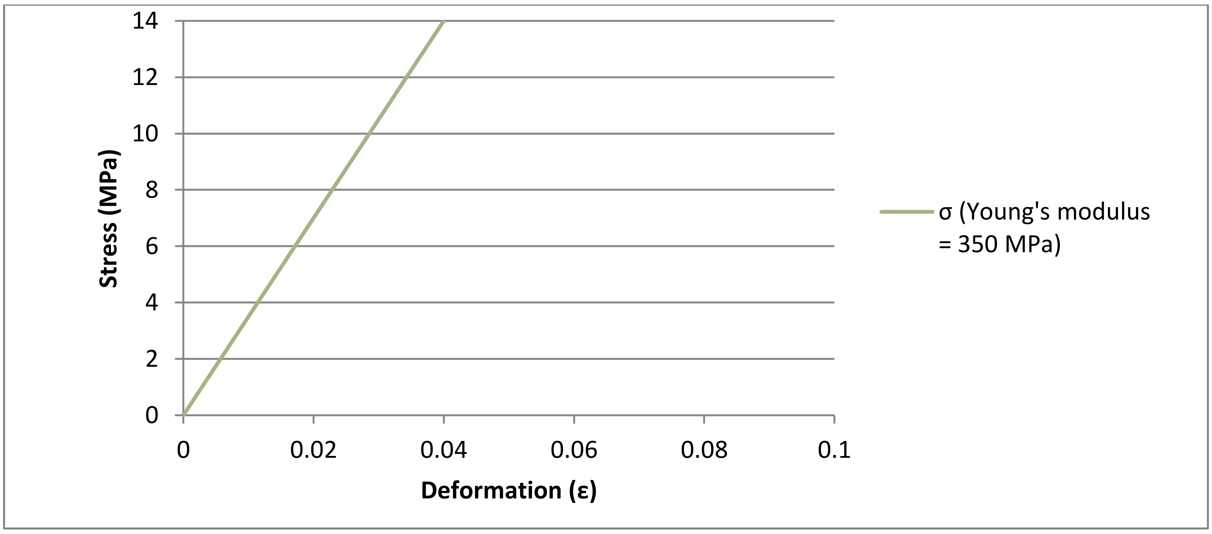

Figure 4.10: Orthotropic stiffness component for tread longitudinal stiffness

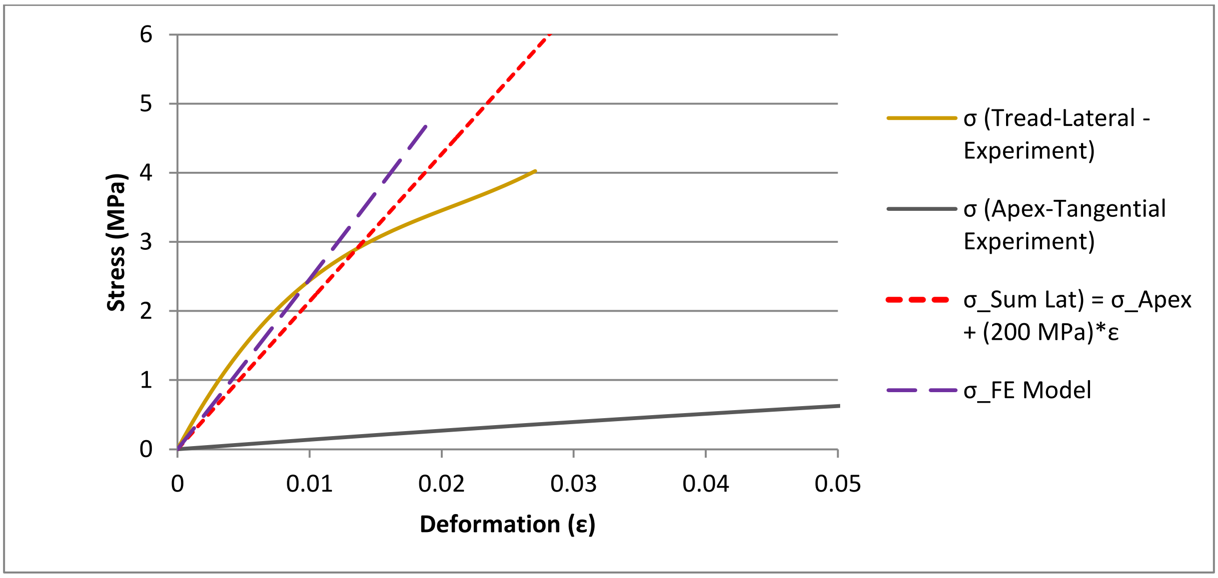

Figure 4.11: Tread material properties in lateral direction

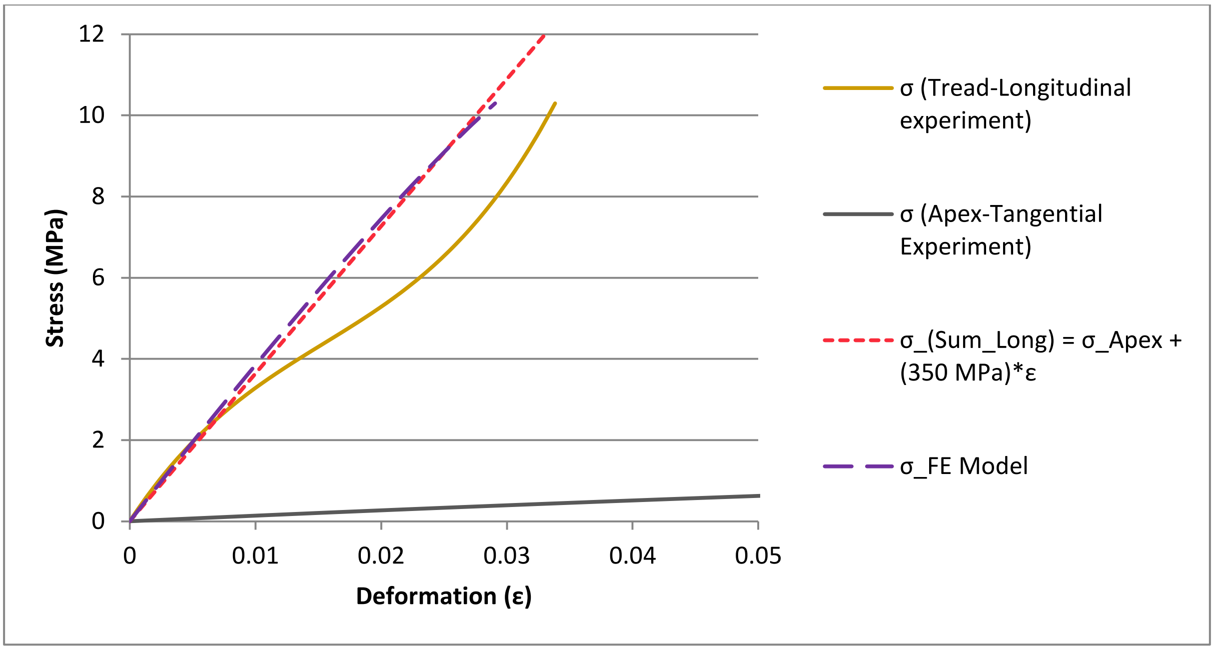

Figure 4.12: Tread material properties in longitudinal direction

The material properties correlate fairly well with the experimental values obtained from the tensile tests done on the samples of the sidewall and the tread of the tyre. The material properties used in the test samples developed in Marc are used in the full tyre model developed. The material properties can be adjusted until the tyre model generated gives the most accurate output for the deformation upon loading.

The material properties used in the tyre segment models are copied into the tyre model developed. A two-dimensional model of the tyre is first developed as described in the following section.

From this model, a three-dimensional model of the tyre is developed by revolving the tyre profile with its properties around the centre axis of the tyre.

4.2 The two-dimensional model of the tyre

A two dimensional model of the tyre (cross-section) is first developed to determine if the material properties used in the models developed of the test segments would give a similar tyre profile when inflated to 2 kPa in the FE model.

4.2.1 Material properties

The orientations of the elements are aligned with the profile of the tyre as shown below in Figure 4.13 in order to align the orthogonal material properties accordingly.

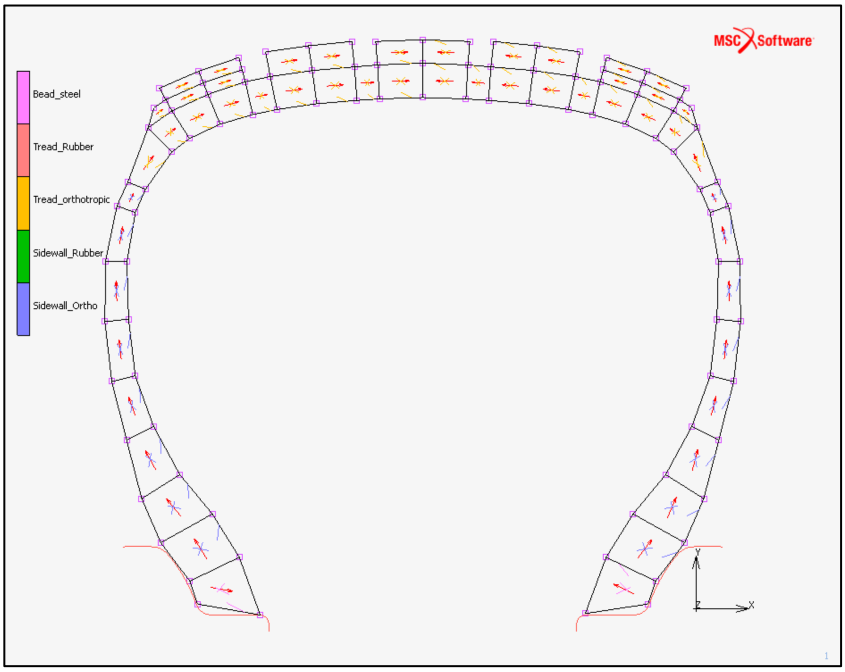

Figure 4.13: Material properties orientation in 2D FE model

The finite elements in the models consist of two sets of elements superimposed onto each other (with the exception of the elements in the bead area). The one set of elements contain orthotropic material properties with a linear stiffness in each orthogonal direction. The other set of elements has non-linear isotropic material properties as described in Chapter 2. Figure 4.14 shows the material properties as applied to the three different segments in the model. The non-linear rubber properties (defined by the colours red and green) cannot be seen since the orthogonal elements are superimposed directly over it.

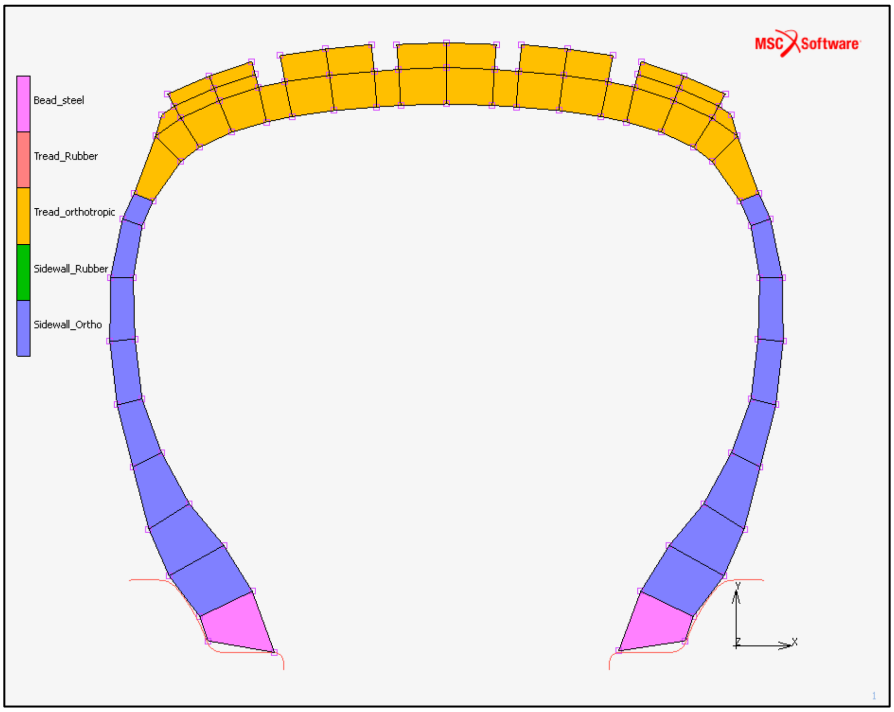

Figure 4.14: Segments in the two dimensional axisymmetric model

4.2.1 Constraints

The tyre is defined as a deformable body in the model, while the curves representing the rim are defined as a rigid body as shown in Figure 4.15.

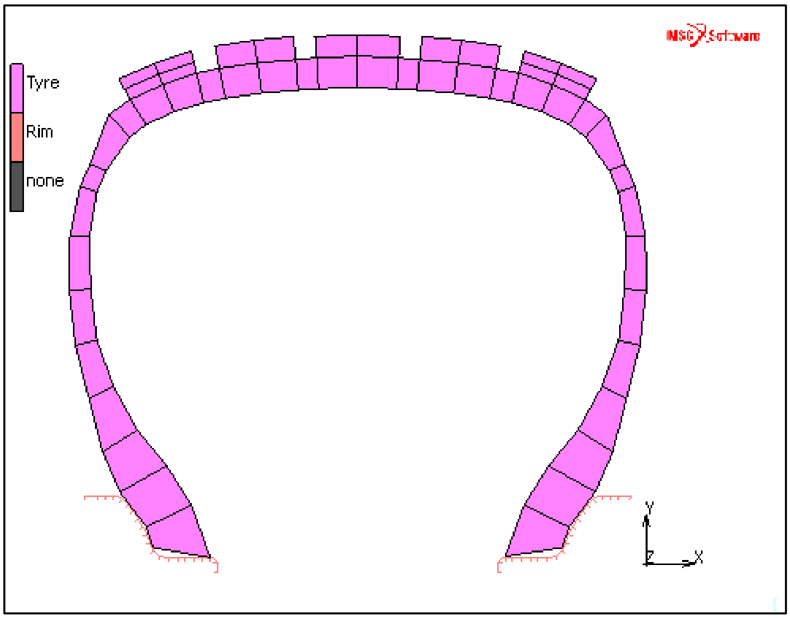

Figure 4.15: Contact defined in the model.

The model is constrained from moving horizontally at the nodes aligned with the centreline of the tyre for the inflation analysis.

4.2.3 Loads applied

A pressure of 200 kPa is applied to the inside of the tyre (as shown in Figure 4.16) to simulate inflation.

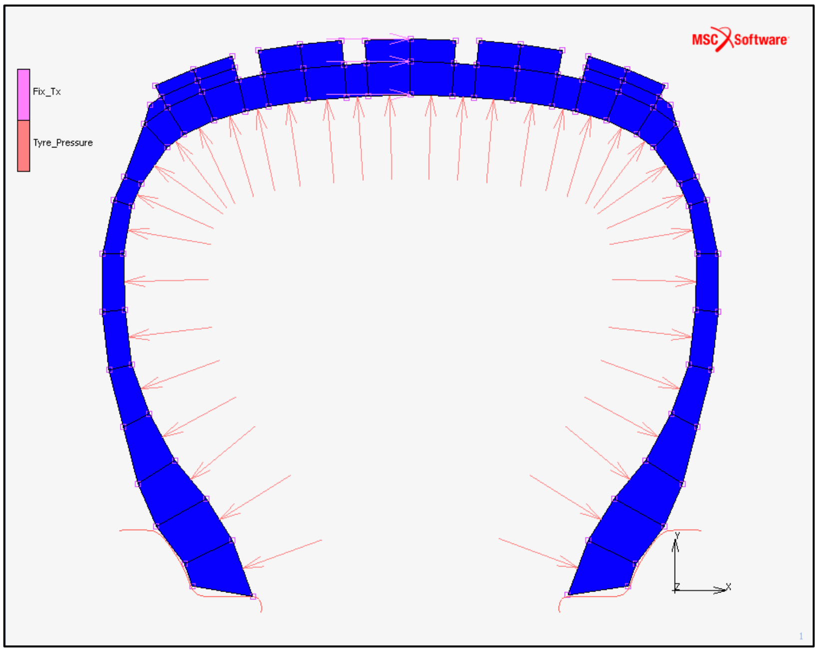

Figure 4.16: Pressure applied to the inside of the tyre.

4.2.4 Results

The displacement upon inflation in the model is shown below in Figure 4.17.

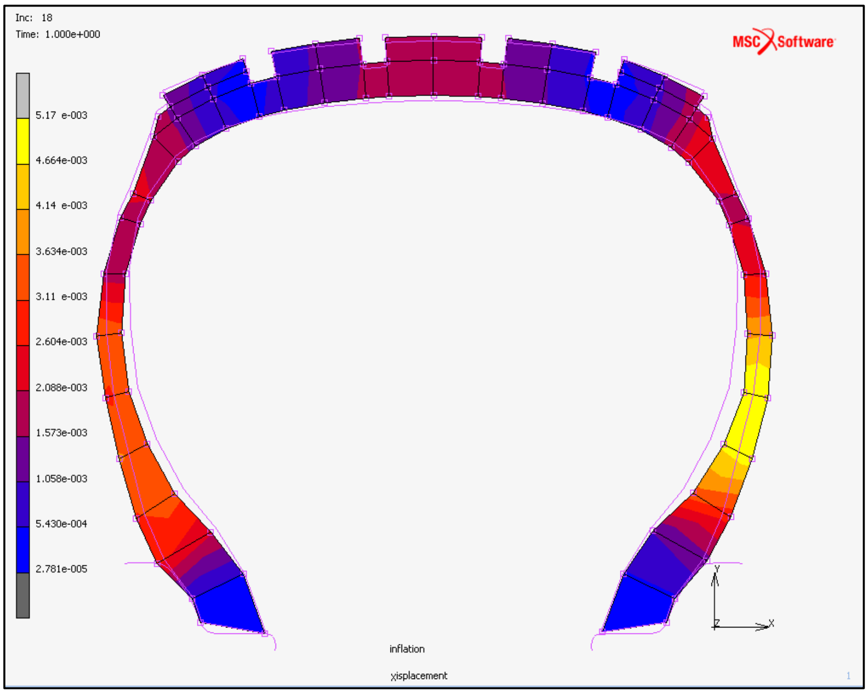

Figure 4.17: Displacement of 2d model inflated to 200 kPa.

The sidewall profile of the inflated 2D model differed slightly from the measured sidewall profile due to the fact that the FEA geometry was measured while the tyre was inflated to 200 kPa and lying flat on a surface.

Because the tyre will eventually be used for dynamic analyses, we are only interested in the global behaviour (such as determining the load-deflection curve or dynamic radius of rolling) of the tyre. A full three dimensional model is developed that can simulate the effect of radial forces.

As discussed in the literature, a finite element model with simply ribbed tread is sufficient for determining lumped variables such as tyre deformation and dynamic radius. For these reasons, the 2 dimensional model is revolved around its central axis to create the three dimensional model. The three dimensional model can be used to compare the results of the FE model to experimental results.

4.3 The three-dimensional model of the tyre

A three dimensional model is required to achieve accurate and complete results for all radial, lateral and longitudinal forces and moments in a dynamic analysis. A three dimensional model is developed.

4.3.1 Material Properties

The non-linear material properties and the orthogonal properties in the three dimensional model are both transferred around the centre axis when the 2 dimensional model is revolved. The sizes of the elements around the contact patch are 3 times as small as the rest of the elements in the tyre since this is the region where large deformation is expected. The number of elements for each region of the 3D tyre is indicated in Table 4.1 below.

Table 4.1: Element used in the 3D model

Region	**Material type**	**Element type**	**Number of elements**
Bead	Isotropic	Hex8	84
Tread	Neo-Hookean	Hex8	1428
Tread	Orthotropic	Hex8	1428
Sidewall	Ogden	Hex8	672
Sidewall	Orthotropic	Hex8	672
Total			**4282**

The orientation of elements in the three dimensional model is shown below in Figure 4.18. The superimposed set of elements can simulate the behaviour of the tyre since the different stiffnesses in the respective orthogonal directions are all accounted for.

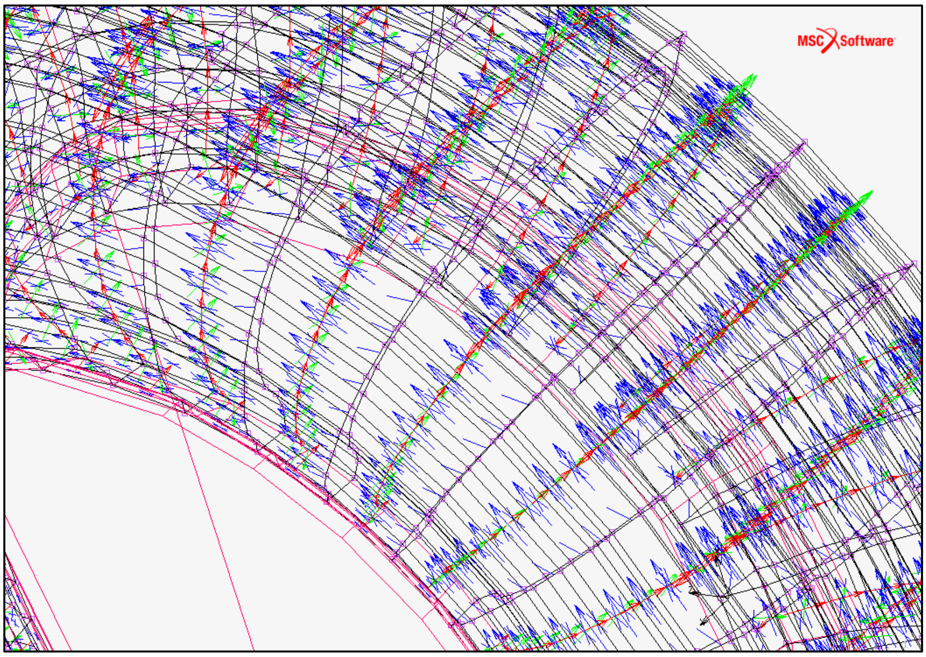

Figure 4.18: Orientation of elements in the three dimensional tyre model.

4.3.2 Constraints

In the 3-dimensional model, the plate (or plate with cleat) used later in the experimental tests in Chapter 5 is also modelled as a rigid body. The plate is given a constant velocity towards the tyre as input to simulate the movement of the actuator pushing the plate against the tyre. The contact bodies are shown in Figure 4.19. The contact between the rim and the tyre are defined as a ‘glued’ connection in a contact table used by MSC.Mentat. The contact between the tyre and the plate, and the contact of the tyre with itself are defined as ‘touching’.

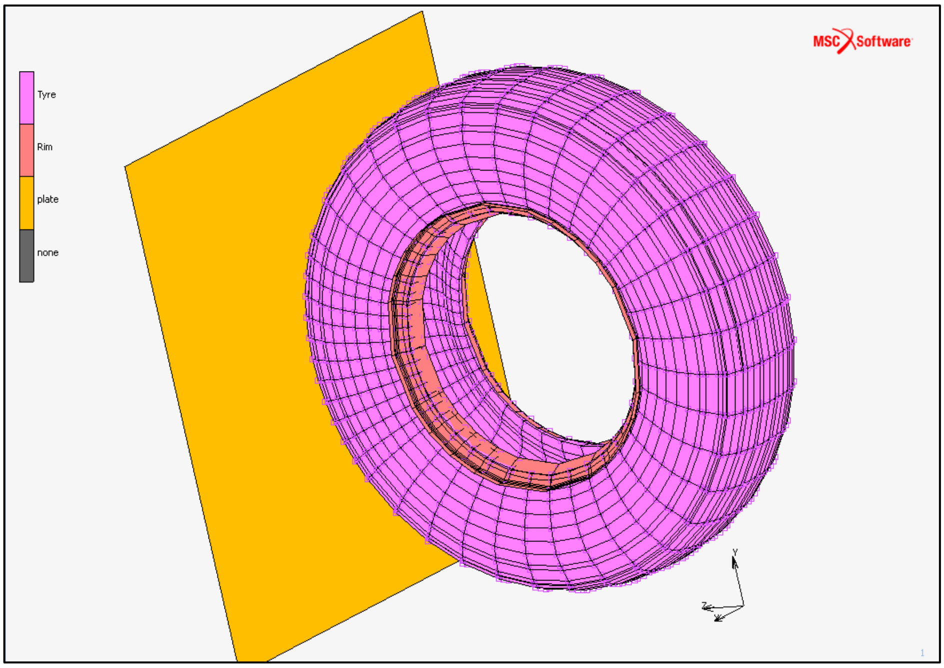

Figure 4.19: Contact bodies in the 3-dimensional FE model

4.3.3 Loads applied

Since road profiles will almost never cause symmetric deformation in the tyre, the fixed constraint in the middle of the tyre is removed for the 3-dimensional model. The tyre pressure of 200 kPa is applied to the inside faces of the elements in the model (see Figure 4.20).

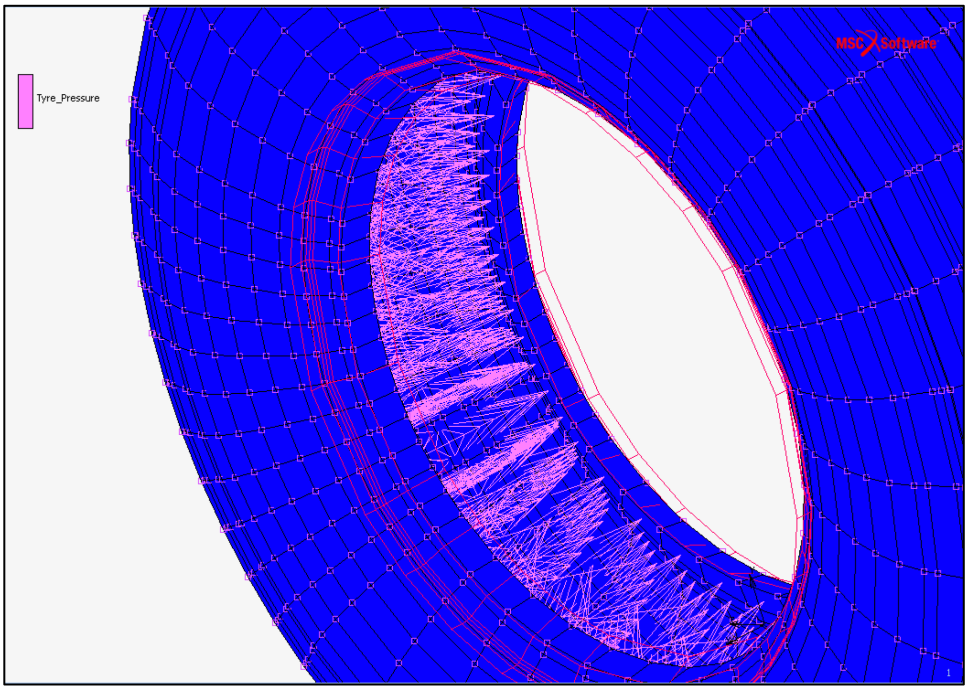

Figure 4.20: Inflation pressure applied to the inside of the three dimensional tyre

The geometry of the inflated tyre model is representative of the actual geometry of the tyre when inflated to 200 kPa.

5 Tyre experimental testing

As discussed in Chapter 2.3.4, extensive tests must be performed in order to obtain all of the necessary information and parameters to properly characterize a tyre for quasi-static simulations of vertical forces.

The tyre studied is characterized using the material properties obtained in Chapter 3.

Various tests are performed to determine the load vs. displacement curves for various loading conditions as described in the following sections. The displacement curves of the sidewall are also measured with lasers at the point of contact with a flat surface and various cleats. The experimental setups of these measurements are described in this chapter.

5.1 Cleat tests

Global tyre stiffness can be represented by the slope of a force vs. displacement graph. The vertical stiffness of a tyre influences the forces transmitted to a vehicle while driving. The characteristics of a tyre can be influenced, amongst other factors, by the following:

- Tyre and rim size
- Tyre pressure
- Tyre construction
- Tyre age
- Tyre orientation
- Shape of indenter plate (cleat)

If one could match the behaviour of a tyre for obstacles in a finite element model, it stands to reason that a fairly accurate model can be generated to simulate tyre behaviour. For this reason, cleats are used to simulate obstacles in a road.

5.1.1 Radial load vs. displacement

An experimental test was set up to measure the global stiffness of the tyre being investigated. First, the tyre was deflated, and the valve was removed, enabling measurement of the global stiffness (load vs. displacement) of the tyre without the influence of the pressurized air. The tyre was first tested at zero inflation pressure to determine if the material properties used in the model were representative of the tyre being investigated.

Thereafter, the tyre was also tested at an inflation pressure of 200 kPa to obtain radial force vs. displacement data for different loading conditions.

The tyre was mounted to a rigid frame. An actuator was lined up with the tyre (as seen in Figure 5.1 and Figure 5.2) to supply the input force to the tyre. The actuator was driven by a sine wave with amplitude of 1.15V and sample frequency of 1000 Hz, with an application frequency of 0.02 Hz. The tyre was deflected by this input signal from its unloaded position.

The displacement and output from the actuator was measured and recorded during tests. The equipment used in the experimental measurements was as follows:

- Schenck PL100 Actuator
- 100 kN load cell
- Laser displacement transducer (Acuity AR700)
- eDaq data acquisitioning system
- K7500 Zurich Bell Servo controller
- Rigid frame for mounting of tyre
- X-Y platform for mounting the lasers

Figure 5.1: Experimental setup for tyre stiffness and cleat tests (side view of tyre) – 51mmx51mm cleat lined up laterally

Figure 5.2: Experimental setup for tyre stiffness and cleat tests (seen from above)

The load cell was mounted between the tyre and the actuator to measure the reaction force generated by the tyre upon loading. A laser displacement transducer was also mounted to a fixed distance from the centre of the wheel. The displacement of the plate mounted to the load cell was directly measured. It is plotted in Figure 5.3 for the deflated tyre end in Figure 5.6 for the inflated (200 kPa) tyre. This was done to get a more accurate displacement measurement of the tyre's deformation. The difference in displacement measurement with the laser and with the actuator can clearly be seen in Figure 5.6 for the inflated tyre. This difference in displacement is caused by the bending of the mounting the tyre was mounted to. The displacement obtained from the laser is thus used, since it gives a more accurate representation of the deformation of the tyre.

The tests were done using six different cleats with different dimensions: 19mm x 19mm, 25mm x 25mm, 38mm x 38mm, 51mm x 51mm, 76mm x 76mm, 100mm x 50mm. The tests were performed with the cleats lined up laterally and longitudinally with the centre line of the tyre.

Figure 5.4 and Figure 5.5 show the force (output signal obtained from the actuator) against displacement graphs (stiffness graphs) for the tyre while deflated to 0 kPa. The quantization in Figure 5.4 and Figure 5.5 are due to very low loading (a maximum load of 2.5 kN measured with a 100 kN load cell) that was applied to the deflated tyre.

Figure 5.7 and Figure 5.8 give the stiffness graphs for the tyre inflated to 200 kPa. The loads reported for the displacements of the surface are of the same magnitude order as reported by Lee, et al., 1997. Therefore, it can be assumed that the results obtained are realistic values.

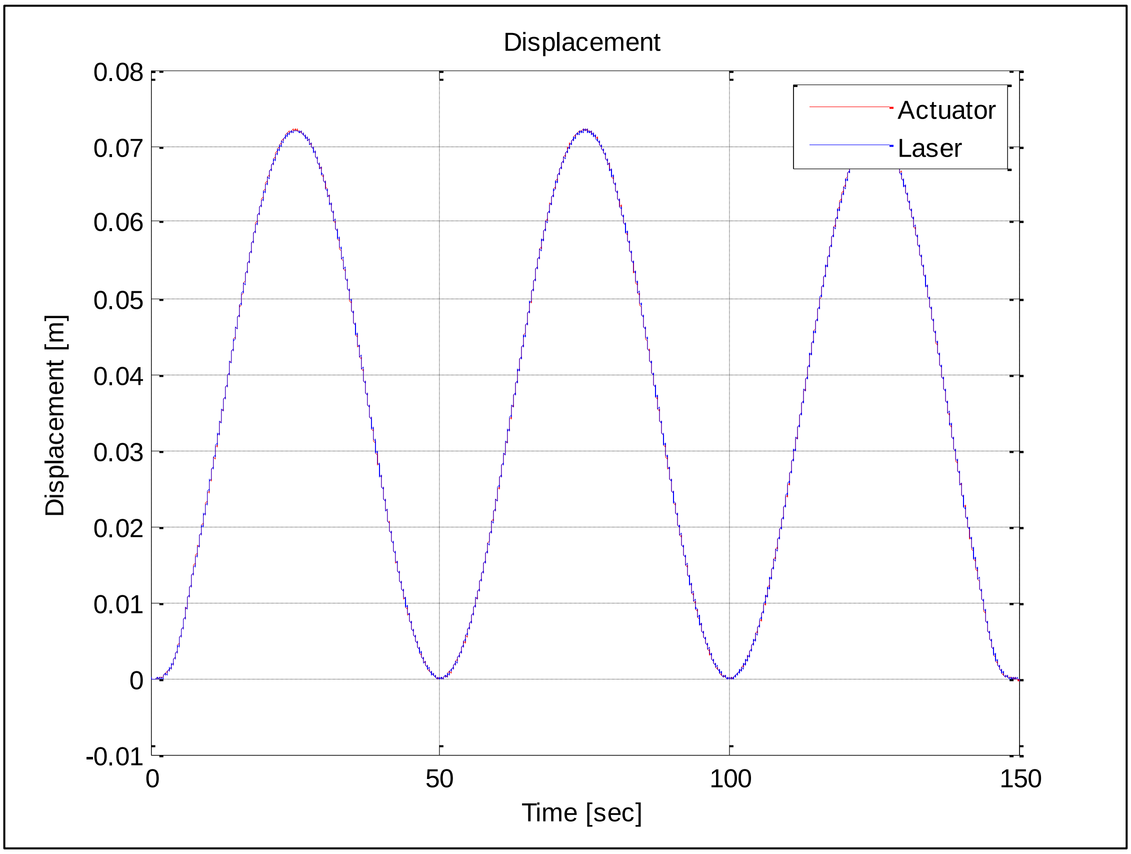

Figure 5.3: Displacement measured with deflated tyre on a flat surface

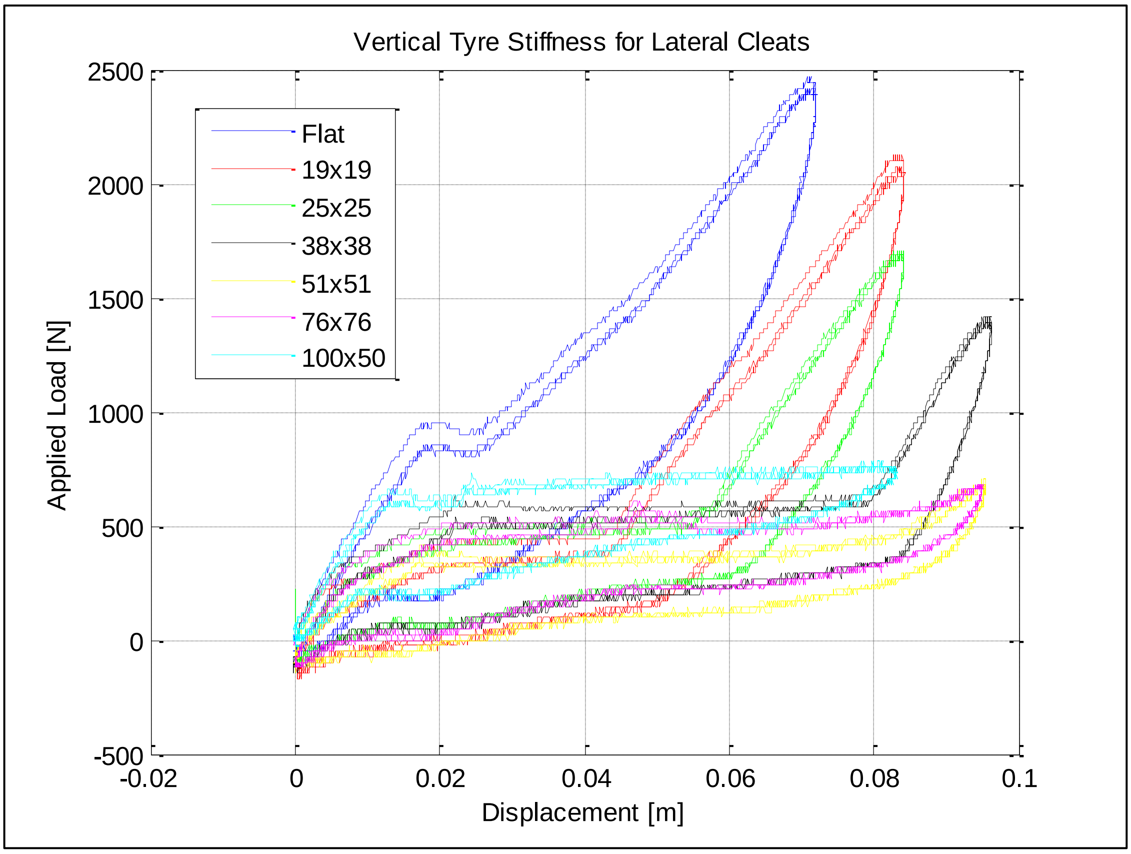

Figure 5.4: Radial tyre stiffness for lateral cleats at 0 kPa

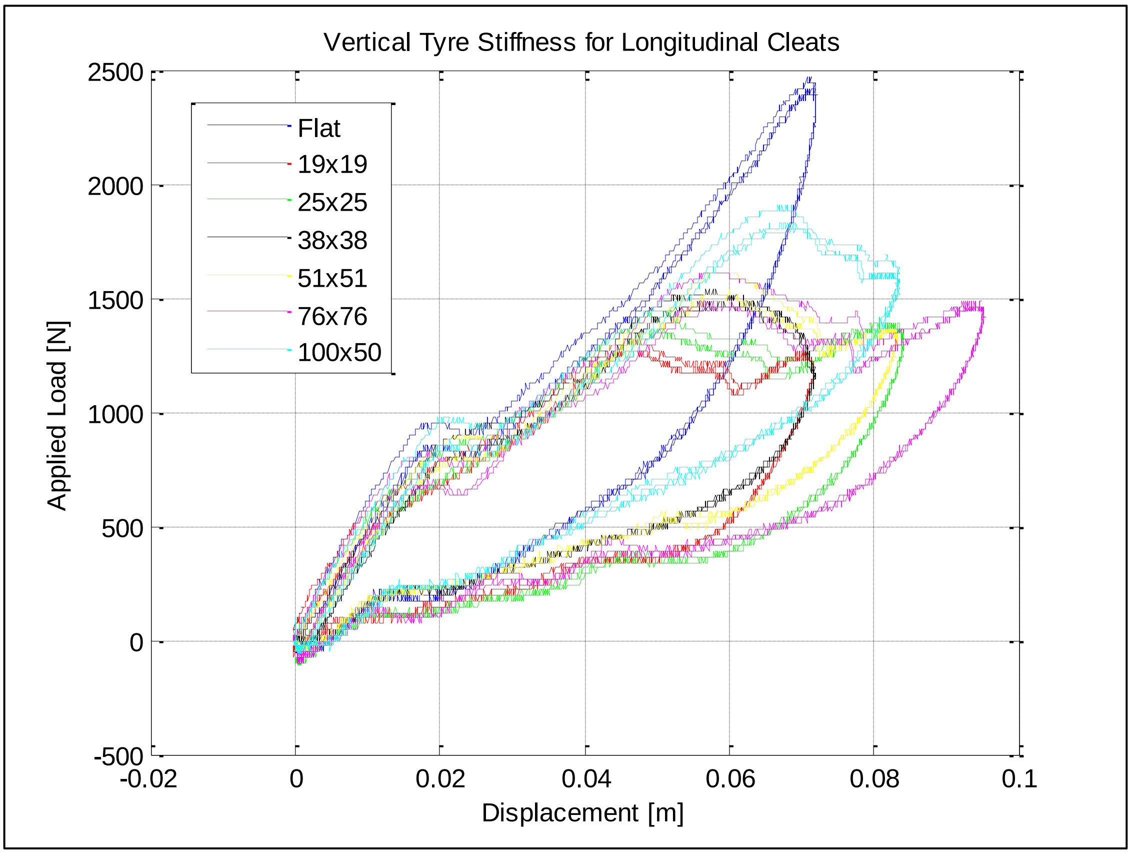

Figure 5.5: Radial tyre stiffness for longitudinal cleats at 0 kPa

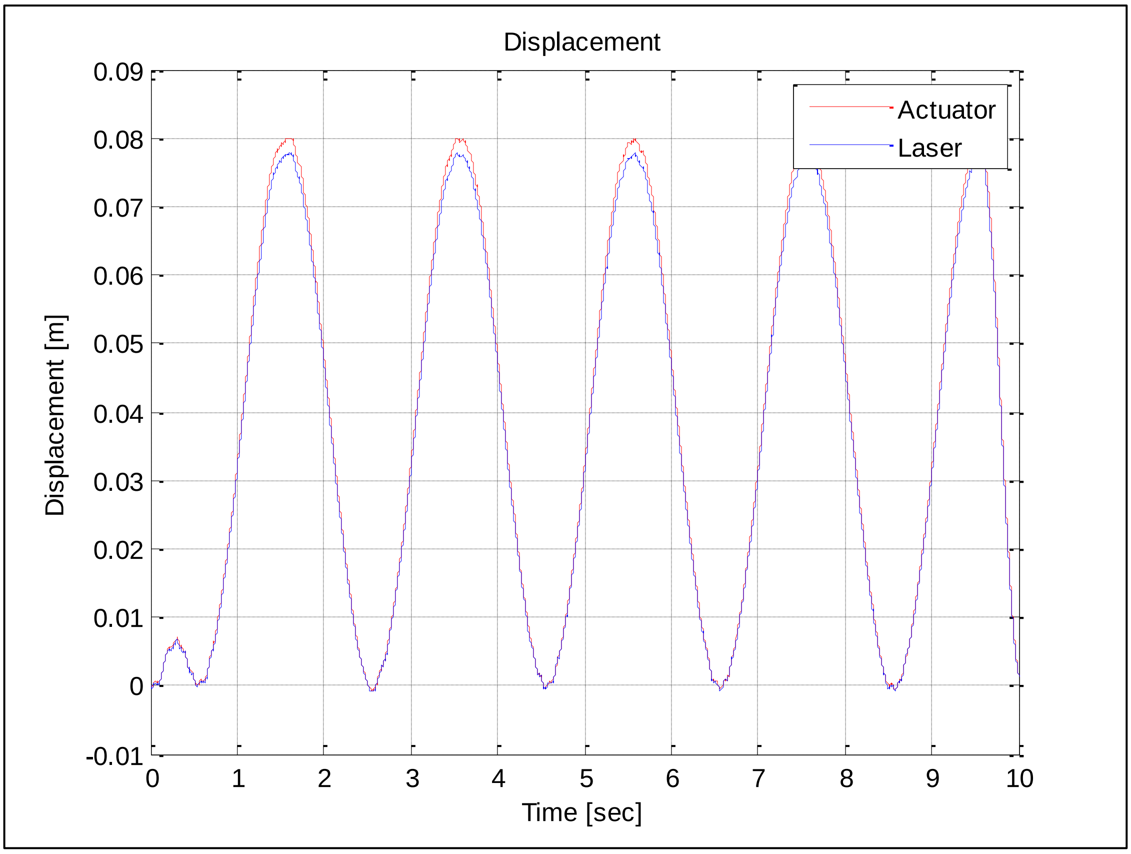

Figure 5.6: Displacement measured with inflated tyre (200 kPa) on a flat surface

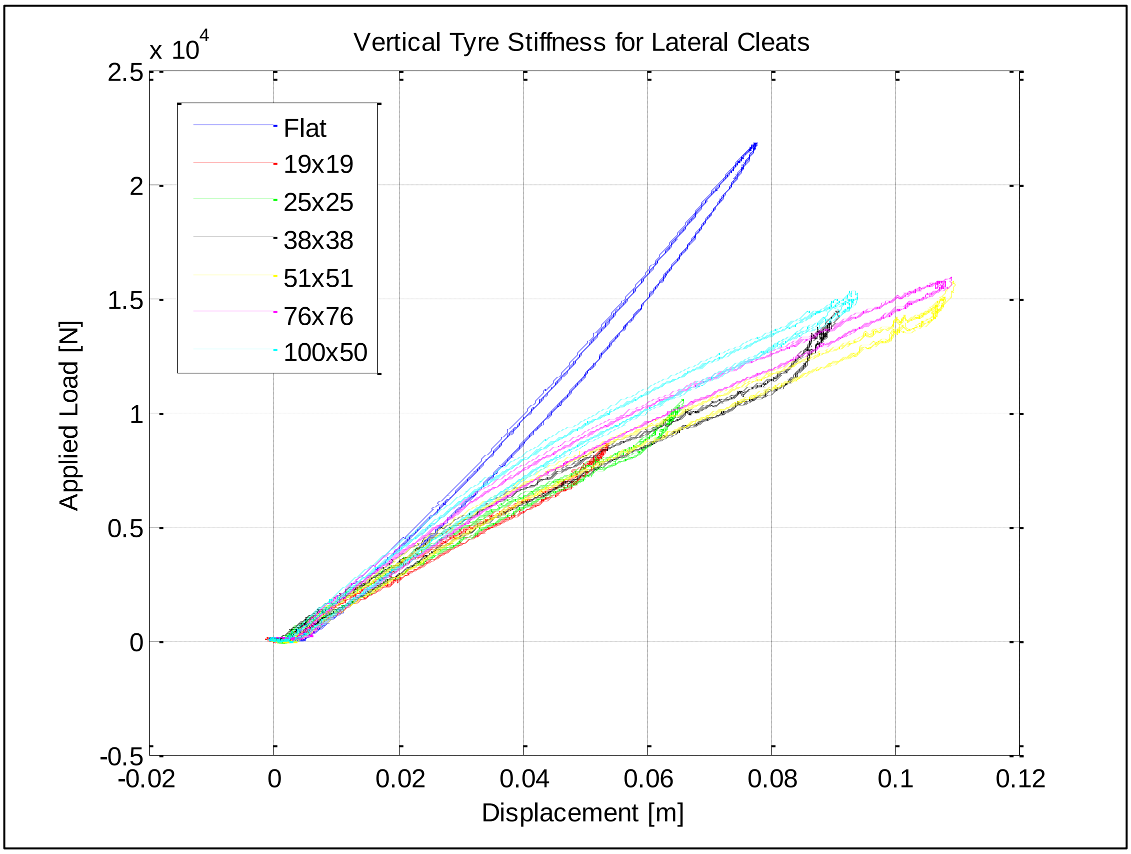

Figure 5.7: Radial tyre stiffness for lateral cleats at 200kPa

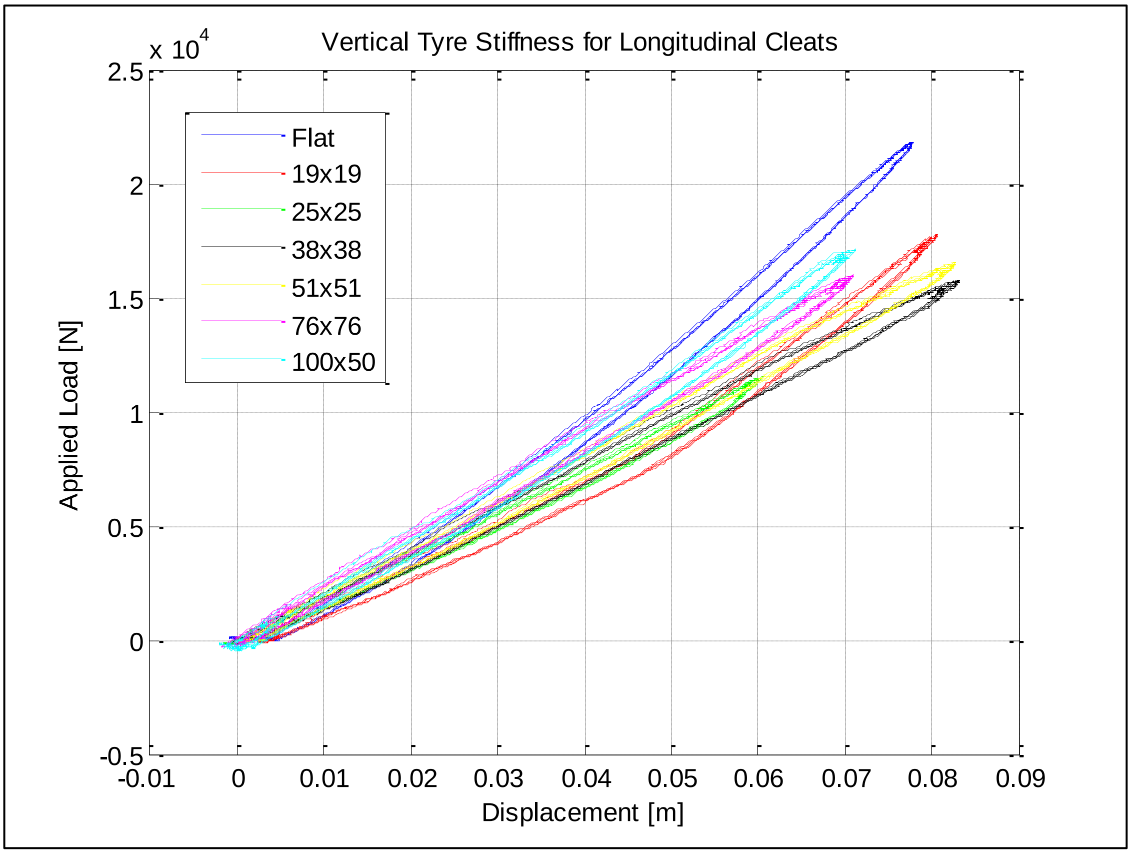

Figure 5.8: Radial tyre stiffness for longitudinal cleats at 200 kPa

The quantization seen in the load vs. displacement graphs for the deflated tyre is due to the low loading conditions. Since it will only be used to confirm that the material properties are realistic values for the tyre structure it was accepted as sufficient.

The load vs. displacement curves for the inflated tyre showed little hysteresis effect of the rubber. For static analysis it will thus be acceptable to disregard the hysteresis effect for the tyre model developed and to use the averaged profile to validate and update the FE model.

Accurate sidewall profiles were also obtained to validate the tyre model.

5.1.2 Sidewall deformation profiles

Using the same experimental setup, with the same cleats, the tyre sidewall profiles were measured at the centre of indentation (due to the cleats) at different loading conditions, using two Acuity AR700 lasers. Again, the tests were performed on a deflated tyre, and a tyre inflated to 200 kPa. The lasers were mounted to an X-Y platform. One laser was moved over the profile (lateral measurement) while the other measured the distance it travelled in a perpendicular direction (longitudinal measurement). The experimental setup can be seen below in Figure 5.9. The profiles measured are plotted in Figure 5.10 to Figure 5.13.

Figure 5.9: Tyre deformation measured using two lasers.

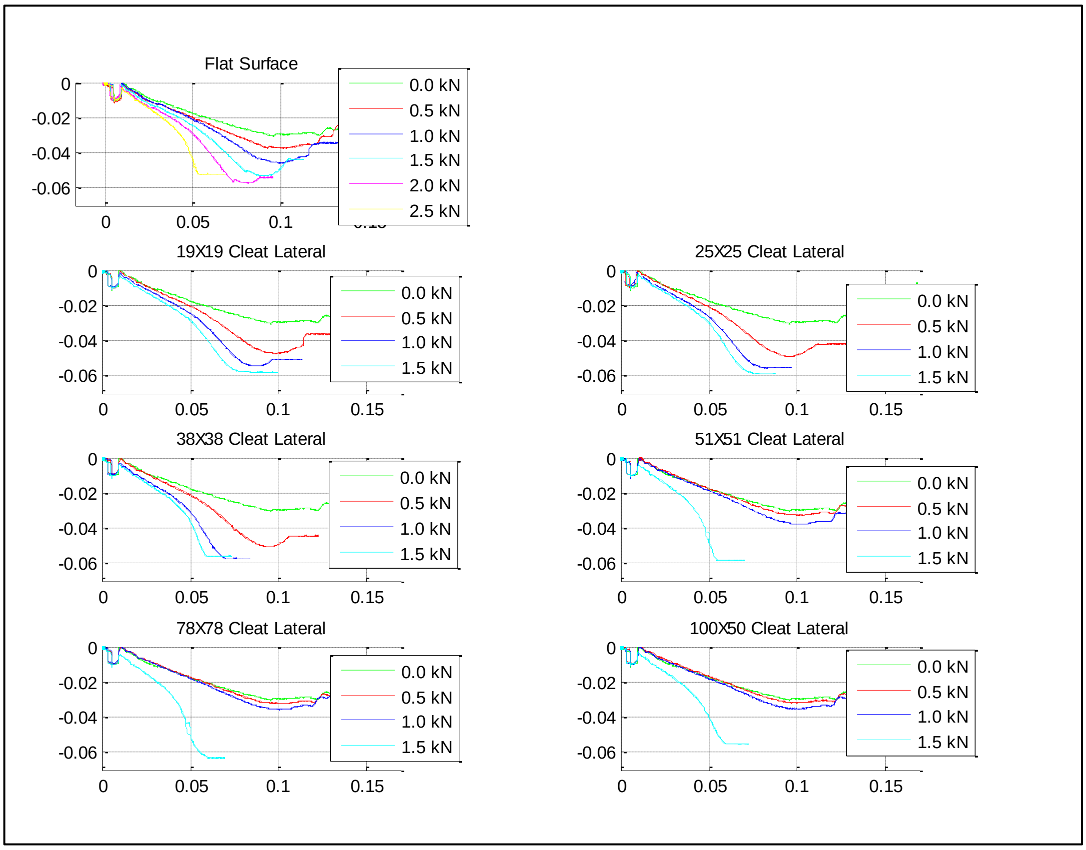

Figure 5.10: Displacements of tyre profile with lateral cleats at 0 kPa [m]

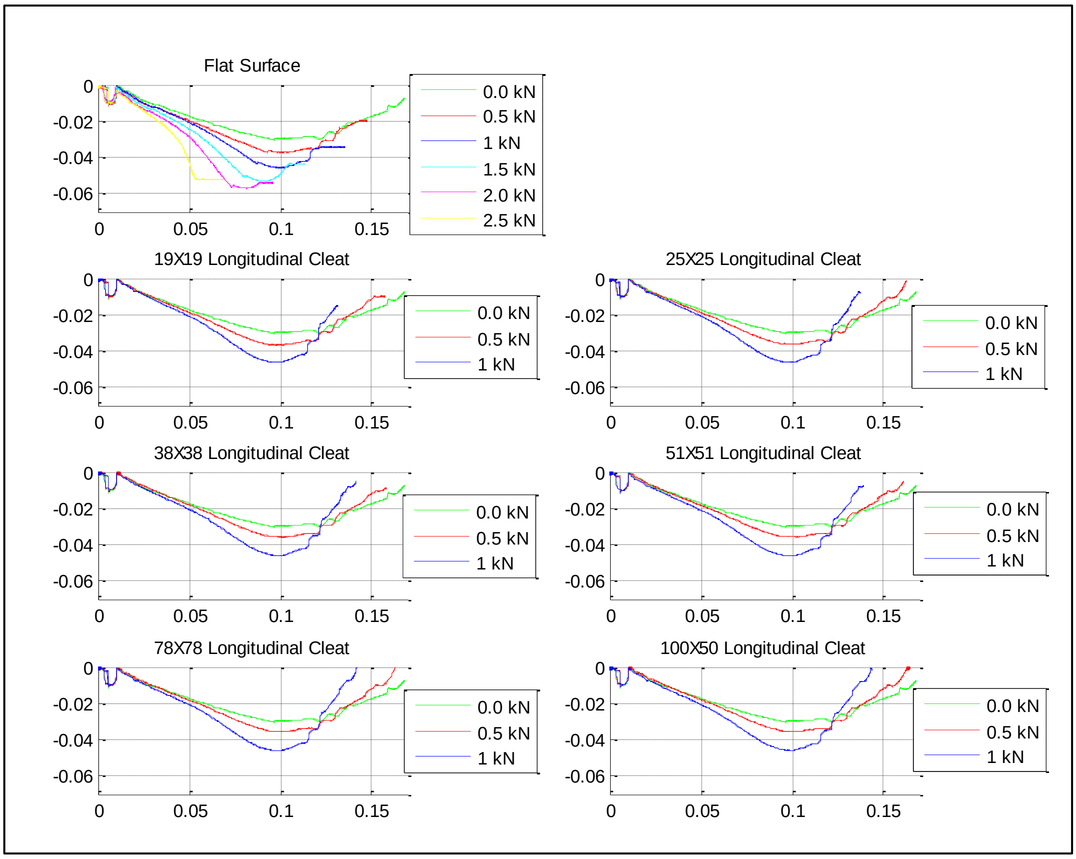

Figure 5.11: Displacements of tyre profile with longitudinal cleats at 0 kPa [m]

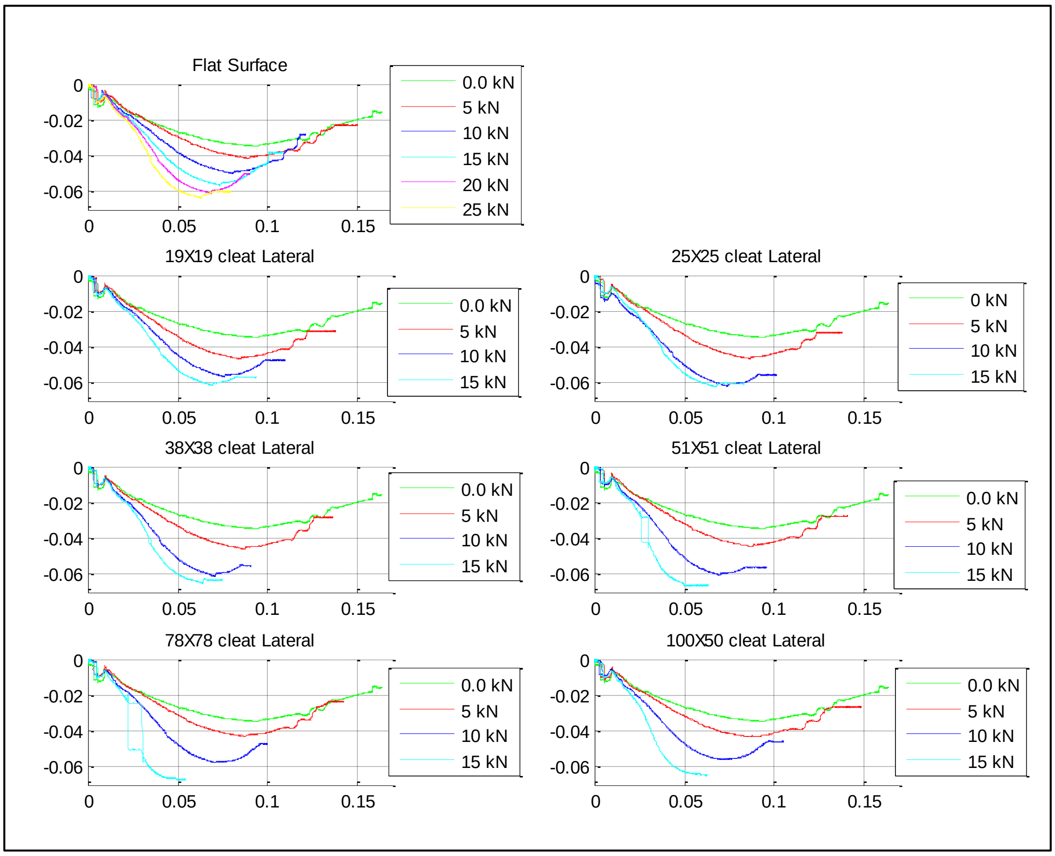

Figure 5.12: Displacements of tyre profile with lateral cleats at 2 kPa [m]

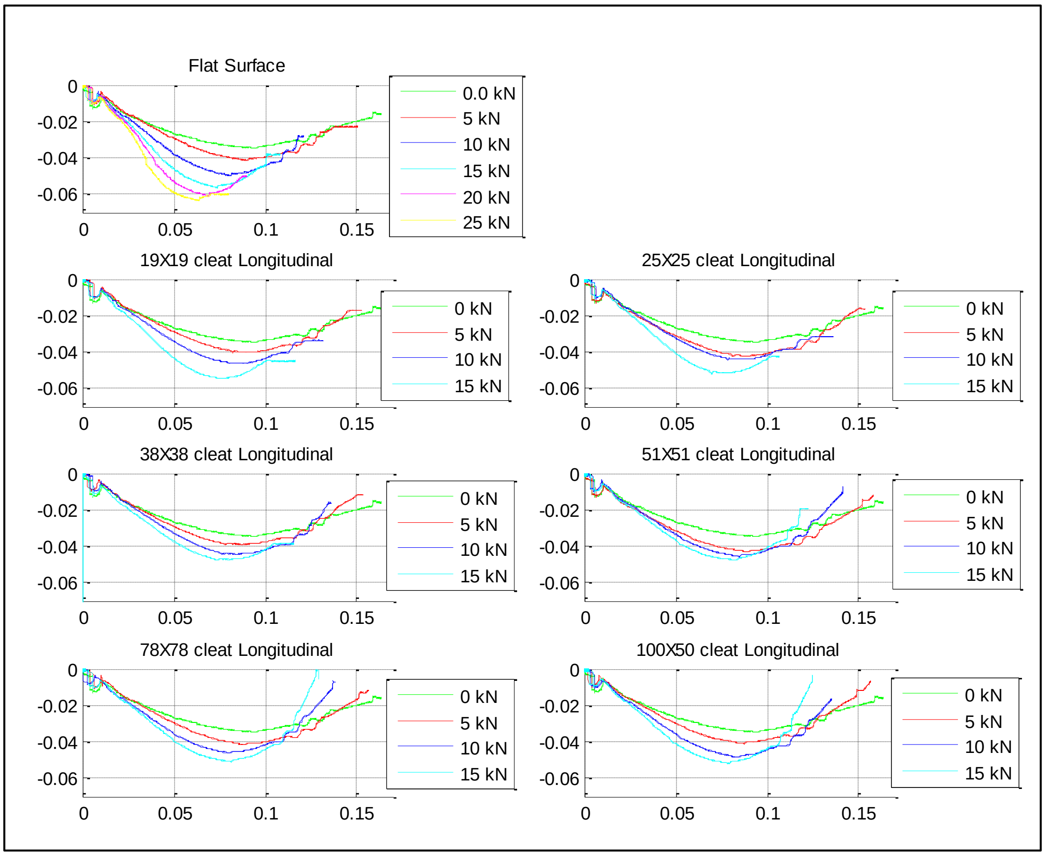

Figure 5.13: Displacements of tyre profile with longitudinal cleats at 2 kPa [m]

6 Correlation of FE tyre model with experimental results

6.1 Validation of material properties in tyre model

The validity of the material properties in the three dimensional tyre model was first checked by analysing the model with no internal pressure (simulating the deflated tyre). The experiments described in the previous chapter were simulated using the three dimensional model.

The load vs. displacement graphs obtained from some of the FE analyses are shown in Figure 6.1 to Figure 6.5. The global stiffness of the FE model is higher than the experimental values. This can be attributed to the glued contact constraint used in the FE model between the tyre and the rim. The modelled tyre can thus not 'fold in' at the rim as it is compressed by the radial load. A glued contact is used because it converges faster. In reality, the tyre sidewall rolled around the edge of the rim while the load was applied to the tyre in the experiment. This can be explained by the absence of internal pressure that normally pushes the tyre against the rim.

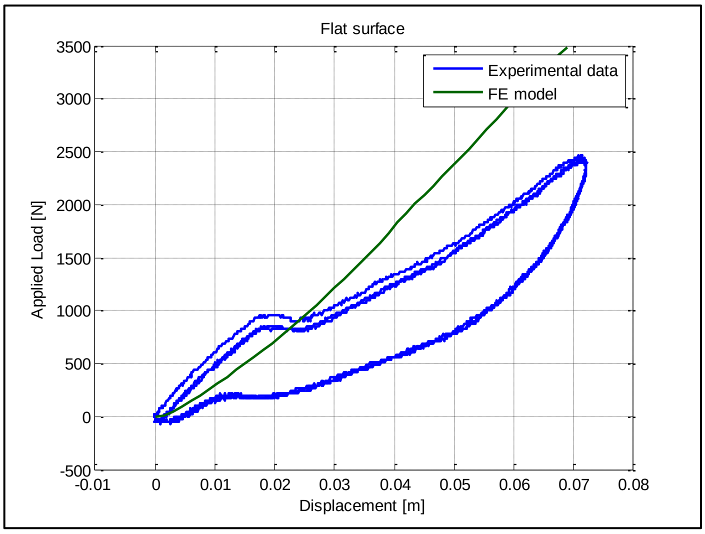

Figure 6.1: Radial load vs. displacement with a flat surface (deflated)

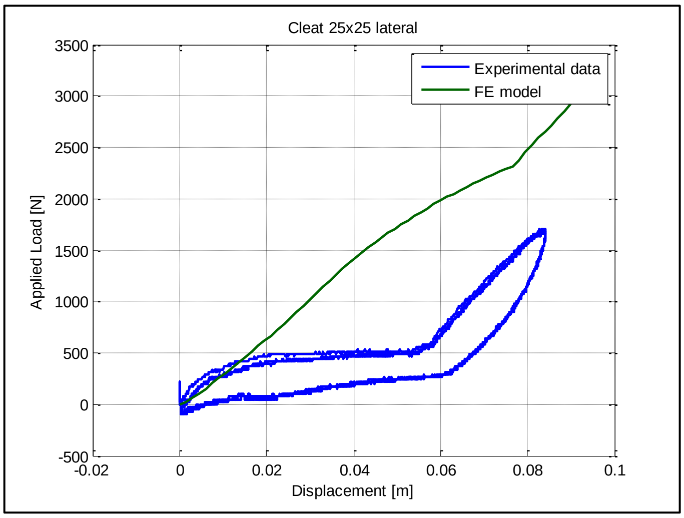

Figure 6.2: Radial load vs. displacement with a 25x25 lateral cleat (deflated)

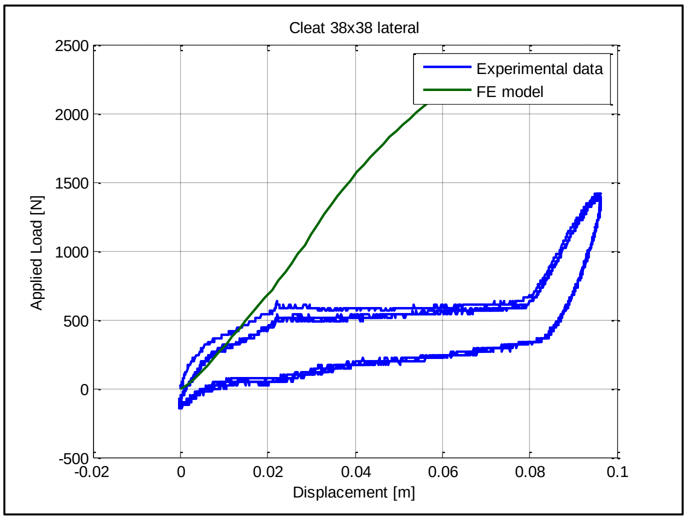

Figure 6.3: Radial load vs. displacement with a 25x25 longitudinal cleat (deflated)

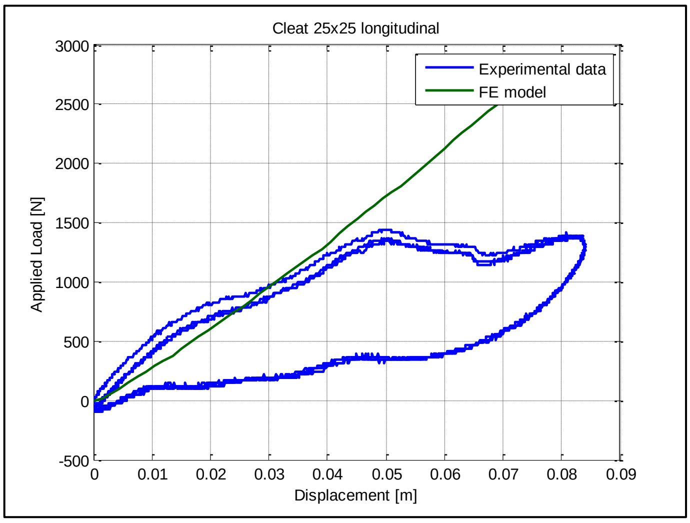

Figure 6.4: Radial load vs. displacement with a 38x38 lateral cleat (deflated)

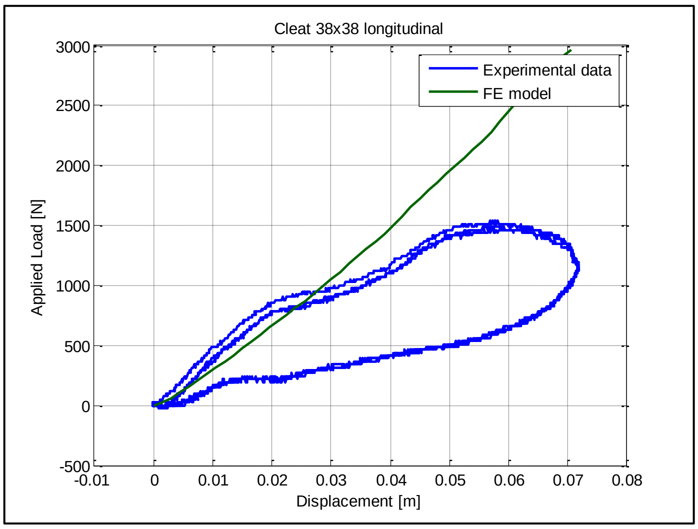

Figure 6.5: Radial load vs. displacement with a 38x38 longitudinal cleat (deflated)

6.2 Analysis cases analysed

The results from the analyses with the deflated tyre indicated load vs. displacement curves with higher stiffness (2 to 3 times higher) than the experimental values measured for the first part of the analyses. The FE model resulted in a stiffer model after the point where the real (deflated) tyre started to fold around the edge of the rim due to the glued contact used. This effect was ignored since tyre simulations will almost always be carried out with inflated tyres that maintains contact with the rim, and not with deflated tyres.

The difference in the stiffness can also be attributed to the linearization about the $0 - 10$ micro-strain point when the values tabulated in Table 3.3 were determined.

Six different cleats are used, each aligned with the lateral and the longitudinal direction as described in Chapter 5. Several different geometry models are used for the different cleats. In the analyses, the plate (with cleats) is moved radially towards the inflated tyre while the rim is fixed in space. The models used in the analysis cases are listed in Table 6.1 with the relevant sizes and orientation of the cleats.

Table 6.1: Geometry models

Geometry model	Cleat	Cleat orientation
GeomA	None	-
GeomB	19 mm x 19 mm	Lateral
GeomC	19 mm x 19 mm	Longitudinal
GeomD	25 mm x 25 mm	Lateral
GeomE	25 mm x 25 mm	Longitudinal
GeomF	38 mm x 38 mm	Lateral
GeomG	38 mm x 38 mm	Longitudinal
GeomH	51 mm x 51 mm	Lateral
GeomI	51 mm x 51 mm	Longitudinal
GeomJ	76 mm x 76 mm	Lateral
GeomK	76 mm x 76 mm	Longitudinal
GeomL	100 mm x 50 mm	Lateral
GeomM	100 mm x 50 mm	Longitudinal

For the sidewall of the tyre model the Ogden model is used for one set of elements, with the first coefficient $\mu_1 = 5.03715e + 008$, its corresponding exponent $\alpha_1 = 0.0028661$, and the second coefficient $\mu_2 = 5.52802e + 008$, with its corresponding exponent $\alpha_2 = 0.00295897$. Another set of elements with orthogonal material properties with a Young's Modulus of 320 MPa in the radial direction is superimposed on the non-linear isotropic elements. A Neo-Hookean model with $C10 = 1.80282e + 006$ is used for the elements simulating the rubber in the tread. Orthogonal elements are superimposed onto it to simulate the effect of the steel wires in the tread. The Young's Modulus used for the orthogonal elements is 200 MPa in the lateral direction and 350 MPa in the longitudinal direction.

These material properties (as obtained in Chapter 4.1) are used as default values and variance in sidewall radial stiffness, tread longitudinal stiffness and tread lateral stiffness are investigated by changing the respective orthogonal stiffnesses. The different combinations of stiffnesses investigated are listed in Table 6.2.

Table 6.2: Material properties investigated

Material property deviation	Youngs modulus in radial orthogonal direction of the sidewall (MPa)	Youngs modulus in lateral orthogonal direction of the tread (MPa)	Youngs modulus in longitudinal orthogonal direction of the tread (MPa)
MatDev0	320	200	350
MatDev1	220	200	350
MatDev2	270	200	350
MatDev3	370	200	350
MatDev4	320	100	350
MatDev5	320	300	350
MatDev6	320	200	250
MatDev7	320	200	450

The load cases analysed to determine how the material characteristics influence the model are shown in Table 6.3.

Table 6.3: Load cases analysed

Model nr	Geometry	Material Properties
A0	GeomA	MatDev0
A1	GeomA	MatDev1
A2	GeomA	MatDev2
A3	GeomA	MatDev3
A4	GeomA	MatDev4
A5	GeomA	MatDev5
A6	GeomA	MatDev6
A7	GeomA	MatDev7
B0	GeomB	MatDev0
B1	GeomB	MatDev1
B2	GeomB	MatDev2
B3	GeomB	MatDev3
B4	GeomB	MatDev4
B5	GeomB	MatDev5
B6	GeomB	MatDev6
B7	GeomB	MatDev7
C0	GeomC	MatDev0
C1	GeomC	MatDev1
C2	GeomC	MatDev2
C3	GeomC	MatDev3
C4	GeomC	MatDev4
C5	GeomC	MatDev5
C6	GeomC	MatDev6
C7	GeomC	MatDev7
D0	GeomD	MatDev0
D1	GeomD	MatDev1
D2	GeomD	MatDev2
D3	GeomD	MatDev3
D4	GeomD	MatDev4
D5	GeomD	MatDev5
D6	GeomD	MatDev6
D7	GeomD	MatDev7
E0	GeomE	MatDev0
E1	GeomE	MatDev1
E2	GeomE	MatDev2
E3	GeomE	MatDev3
E4	GeomE	MatDev4
E5	GeomE	MatDev5
E6	GeomE	MatDev6
E7	GeomE	MatDev7
F0	GeomF	MatDev0
F1	GeomF	MatDev1
F2	GeomF	MatDev2
F3	GeomF	MatDev3
F4	GeomF	MatDev4
F5	GeomF	MatDev5
F6	GeomF	MatDev6

Model nr	Geometry	Material Properties
F7	GeomF	MatDev7
G0	GeomG	MatDev0
G1	GeomG	MatDev1
G2	GeomG	MatDev2
G3	GeomG	MatDev3
G4	GeomG	MatDev4
G5	GeomG	MatDev5
G6	GeomG	MatDev6
G7	GeomG	MatDev7
H0	GeomH	MatDev0
H1	GeomH	MatDev1
H2	GeomH	MatDev2
H3	GeomH	MatDev3
H4	GeomH	MatDev4
H5	GeomH	MatDev5
H6	GeomH	MatDev6
H7	GeomH	MatDev7
I0	GeomI	MatDev0
I1	GeomI	MatDev1
I2	GeomI	MatDev2
I3	GeomI	MatDev3
I4	GeomI	MatDev4
I5	GeomI	MatDev5
I6	GeomI	MatDev6
I7	GeomI	MatDev7
J0	GeomJ	MatDev0
J1	GeomJ	MatDev1
J2	GeomJ	MatDev2
J3	GeomJ	MatDev3
J4	GeomJ	MatDev4
J5	GeomJ	MatDev5
J6	GeomJ	MatDev6
J7	GeomJ	MatDev7
K0	GeomK	MatDev0
K1	GeomK	MatDev1
K2	GeomK	MatDev2
K3	GeomK	MatDev3
K4	GeomK	MatDev4
K5	GeomK	MatDev5
K6	GeomK	MatDev6
K7	GeomK	MatDev7
L0	GeomL	MatDev0
L1	GeomL	MatDev1
L2	GeomL	MatDev2
L3	GeomL	MatDev3
L4	GeomL	MatDev4
L5	GeomL	MatDev5
L6	GeomL	MatDev6
L7	GeomL	MatDev7
M0	GeomM	MatDev0
M1	GeomM	MatDev1
M2	GeomM	MatDev2
M3	GeomM	MatDev3
M4	GeomM	MatDev4
M5	GeomM	MatDev5
M6	GeomM	MatDev6
M7	GeomM	MatDev7

For each load case investigated the load vs. displacement (of the flat surface) of the tyre was plotted and analysed. All the load vs. displacement curves are given in Appendix A. The influence of radial sidewall stiffness, the tread lateral stiffness and the tread's longitudinal stiffness on the global stiffness of the tyre is shown in Appendix B. Three graphs are shown in Appendix B for the flat surface and for each cleat in the lateral position and in the longitudinal position. The first graph shows how changing the radial stiffness of the sidewall influences the tyre characteristic, while the second and the third graph on each page shows how changing the tread's lateral and longitudinal stiffness influences the tyre's characteristic.

Numerous analyses are performed with different combinations of values for the sidewall stiffness in the radial direction and for the tread of the tyre model in the lateral and longitudinal direction. The influence of sidewall and tread stiffness in its respective orthogonal directions is investigated.

6.3 Final model analysis results

The sidewall deformation profiles obtained from the experiments performed are used to validate the tyre model further. Deformation profiles of the sidewall at the different loads (no load, 5 kN, 10 kN, 15 kN) are compared to the experimental measurements. The radial force of the tyre pushing against the plate was plotted against the displacement of the plate for each load case.

The load vs. displacement curves and the sidewall profiles from the rim up to the point where the surface makes contact with the tyre are shown in Figure 6.6 and Figure 6.7 for the flat surface. The material properties obtained in Chapter 3 were first used and the load vs. displacement graphs for these values are labelled as “default values” in the graphs. For each load case the following data was obtained as output:

- Load vs. displacement curve (of surface/cleat pushing against the tyre)
- Sidewall profiles different loads investigated

It is also shown for the lateral 25mm x25 mm cleat in Figure 6.8 and Figure 6.9; for the longitudinal 25mm x 25mm cleat in Figure 6.10 and Figure 6.11; for the lateral 100mm x 50mm cleat in Figure 6.12 and Figure 6.13 and for the longitudinal 10mm x 50mm cleat in Figure 6.14 and Figure 6.15.

The load vs. displacement curves obtained was very accurate at displacements (of the plate or plate with cleat relative to the tyre) below 20 mm. At higher displacement values, the deviated from the experimental values obtained. The material properties that gave the best fit for the entire load vs. displacement graphs at the different load conditions investigated are shown in Table 6.4.

The displacement profiles of the sidewall (of the final model) matched the experimental profiles. The force vs. displacement graphs and the sidewall profile for these values are also shown in Figure 6.6 to Figure 6.15. A full set of results of the load vs. displacement curves for each analysis case is given in Appendix C. The sidewall profiles from the experiments are also compared with the final model for each case analysed in Appendix C.

Table 6.4: Material properties for final FE model of tyre

Sidewall						
Non-linear Ogden model	mu1	alpha1	mu2	alpha2		
	5.037E+08	0.002866	5.528E+08	0.0029589		
Linear Orthotropic	E1	E2	E3	Nu12	Nu23	Nu31
	3.20E+08	1.00E+03	2.00E+06	0	0	0.05
Tread						
Neo-Hookean model	C10					
	1.803E+06					
Linear Orthotropic	E1	E2	E3	Nu12	Nu23	Nu31
	2.00E+08	1.00E+07	2.50E+08	0.1	0.1	0.623

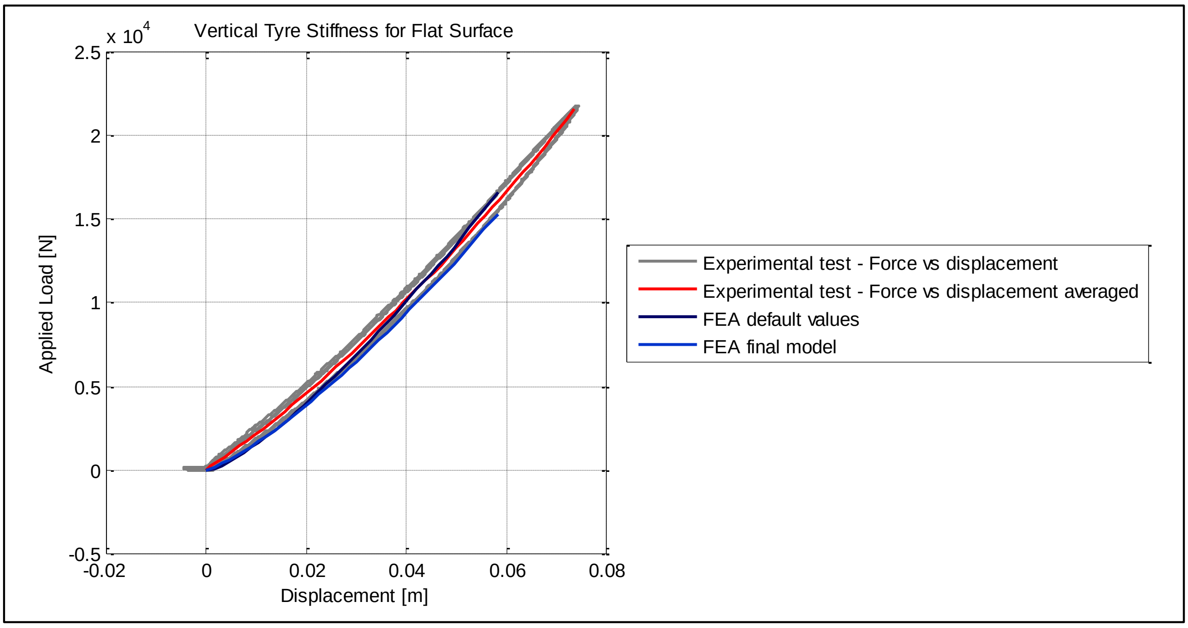

Figure 6.6: Radial load vs. displacement with a flat surface

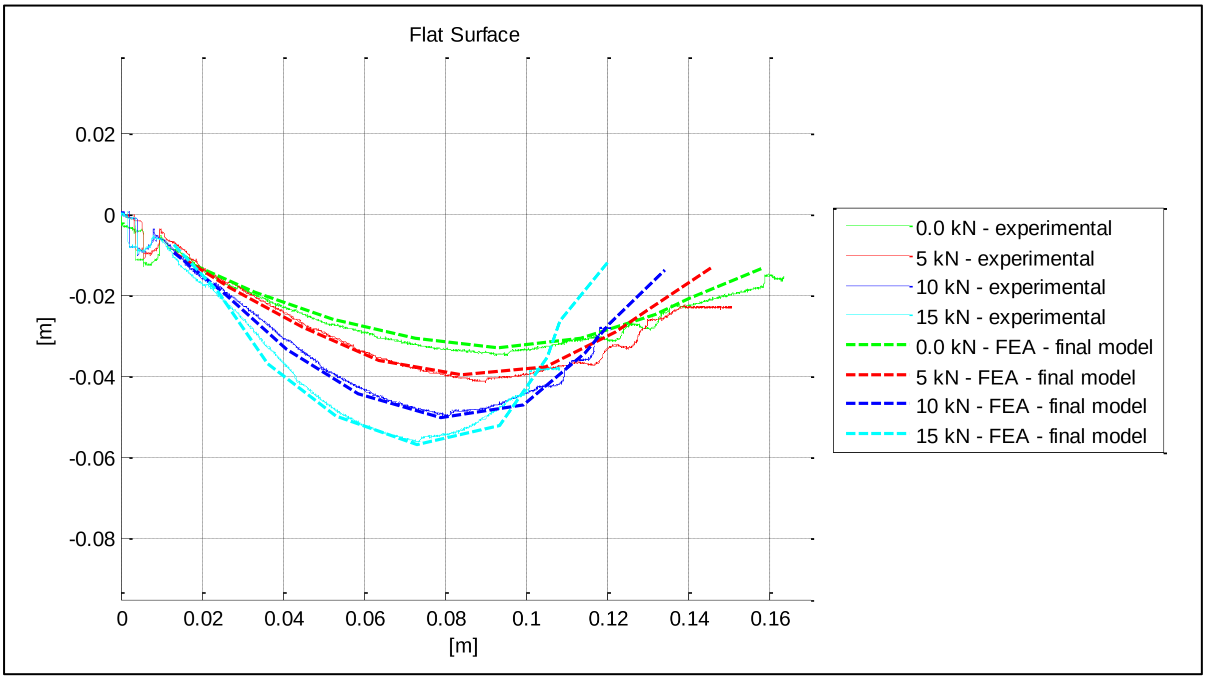

Figure 6.7: Sidewall profiles for a flat surface

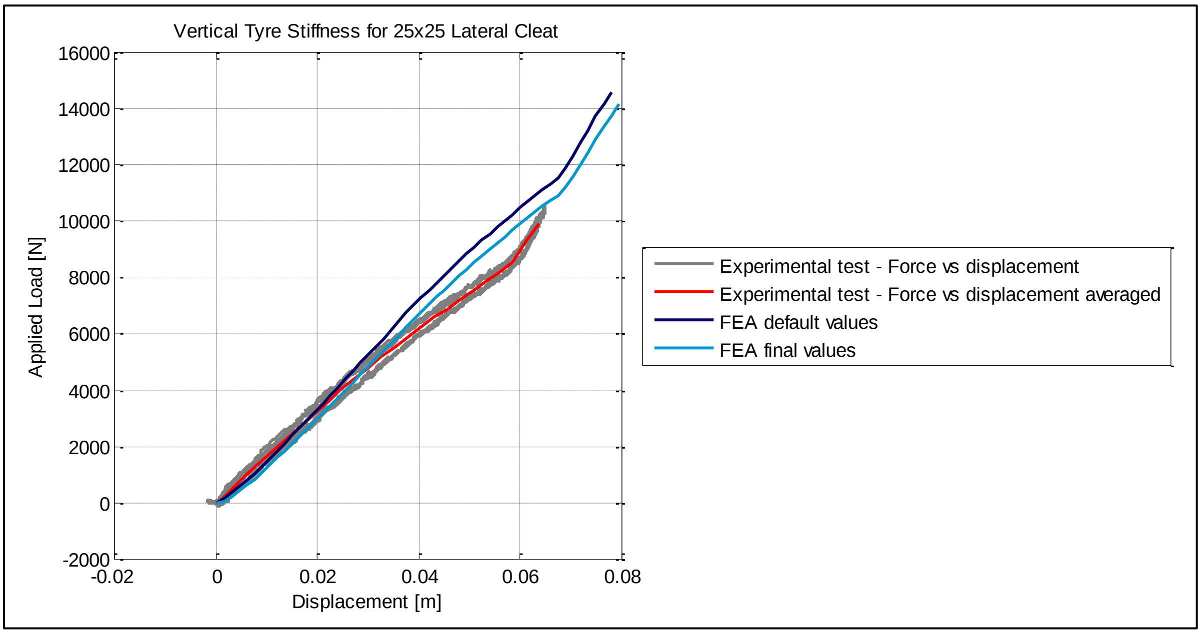

Figure 6.8: Radial vs. displacement with a 25x25 lateral cleat

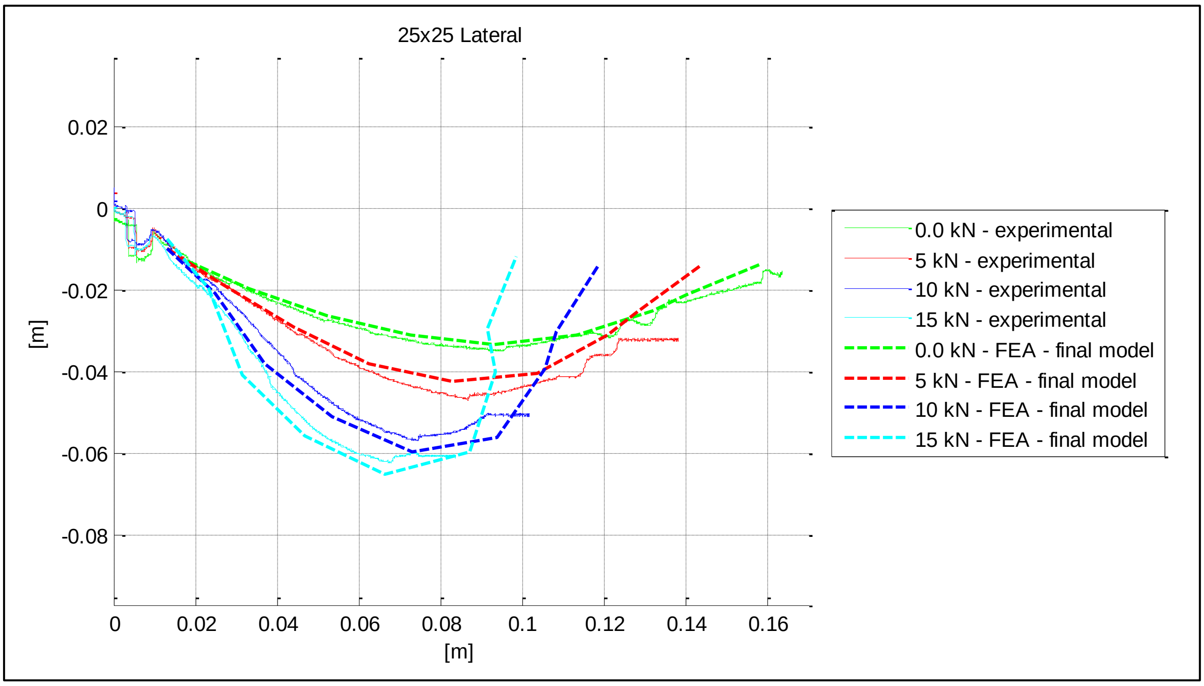

Figure 6.9: Sidewall profiles for a 25x25 lateral cleat

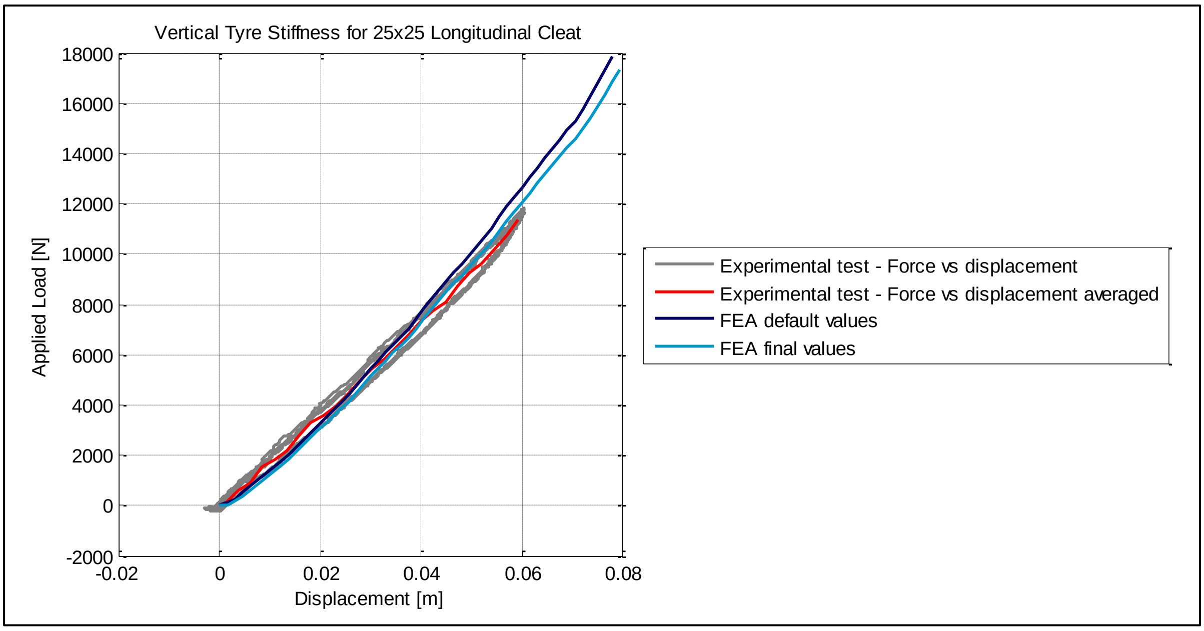

Figure 6.10: Radial vs. displacement with a 25x25 longitudinal cleat

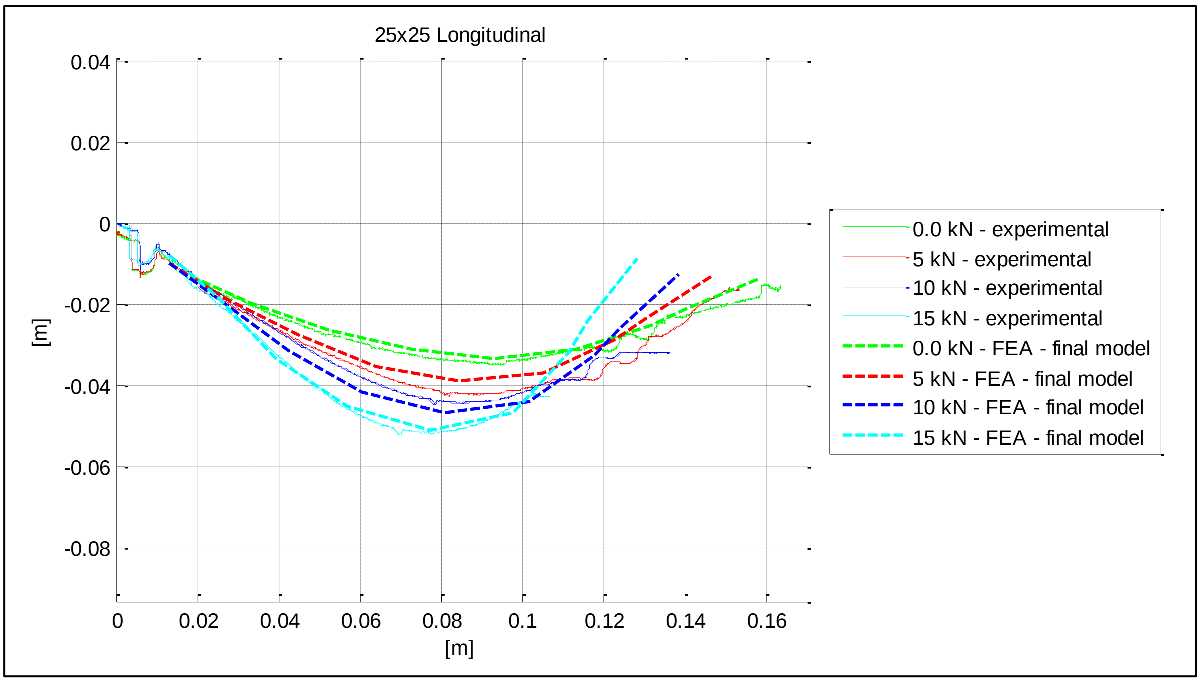

Figure 6.11: Sidewall profiles for a 25x25 longitudinal cleat

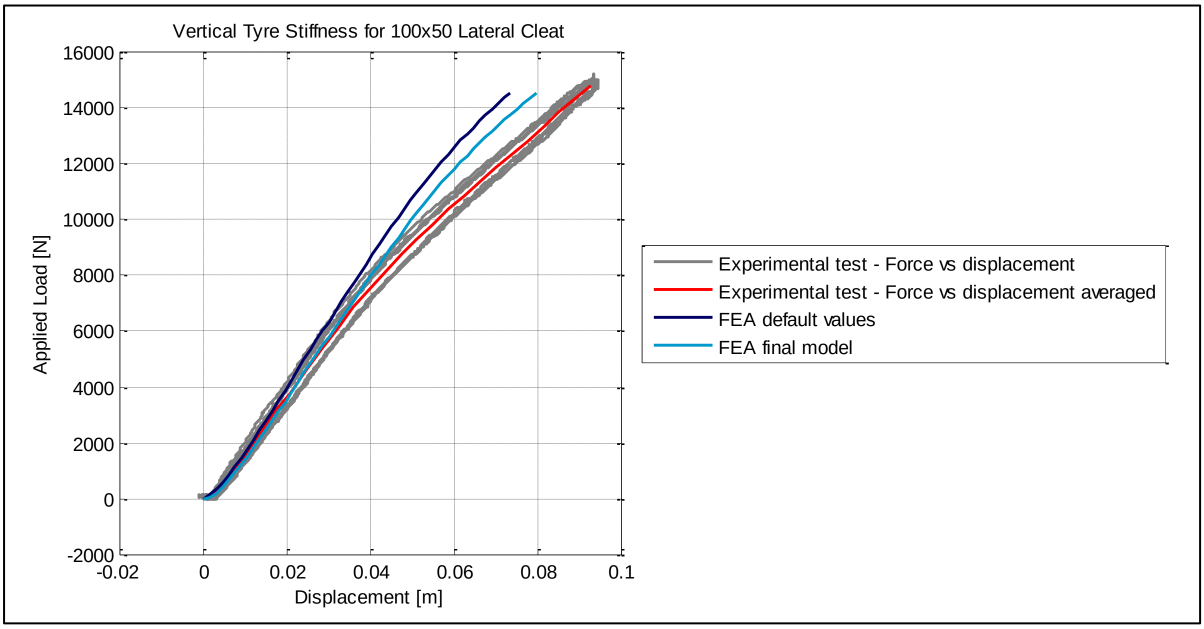

Figure 6.12: Radial vs. displacement with a 100x50 lateral cleat

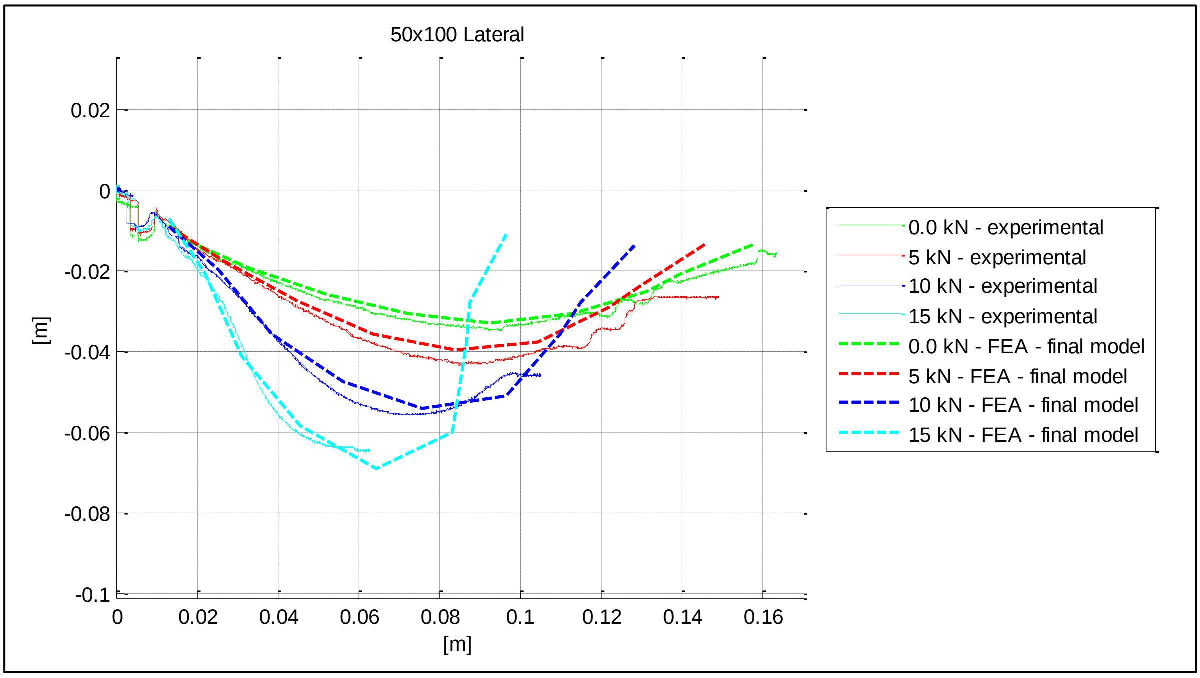

Figure 6.13: Sidewall profiles for a 100x50 lateral cleat

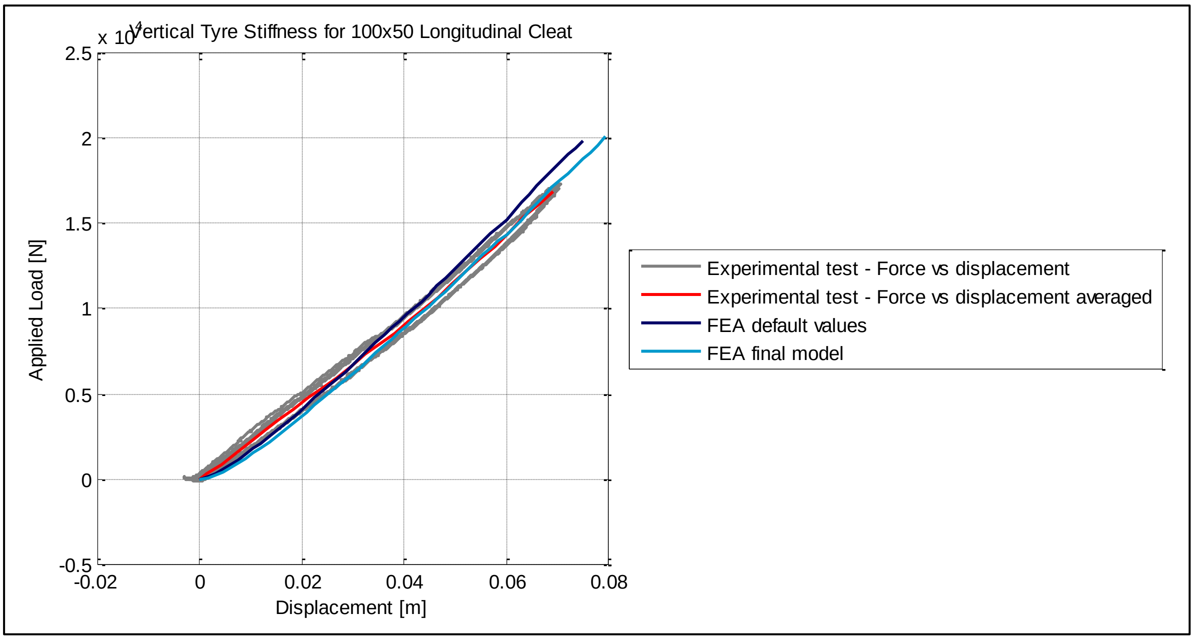

Figure 6.14: Radial vs. displacement with a 100x50 longitudinal cleat

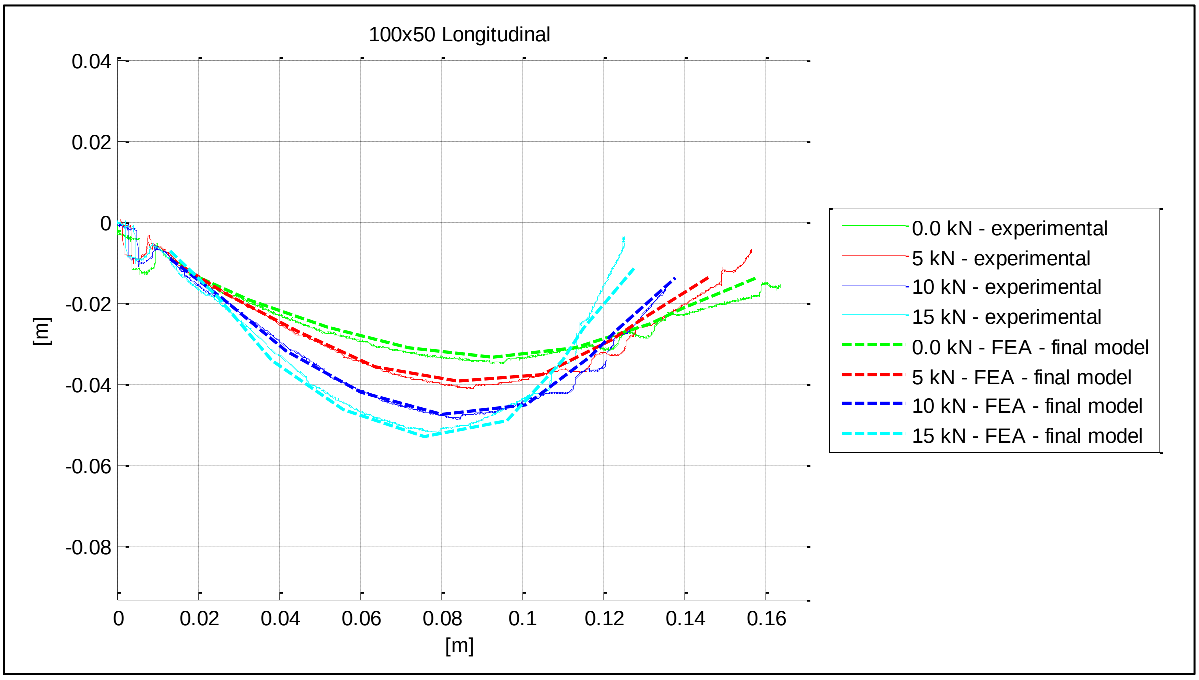

Figure 6.15: Sidewall profiles for a 100x50 longitudinal cleat

6.4 Conclusions

Various load cases (as listed in Table 6.3) were investigated to determine the best possible combination of material properties for good correlation with the experimental results. Differences in sidewall radial stiffness, tread lateral and tread longitudinal stiffnesses were investigated.

The results significantly improved with the alterations of the material properties. The combination of material properties that gave the best fit for all the load cases investigated were determined. The results obtained proved to be adequately accurate for the simulation of a tyre.

The FE model developed correlated well with the load vs. displacement graphs and sidewall displacement profiles determined experimentally.

The direct solver that was used for solving the tyre model is the Paradiso Direct Sparse solver, using 4 processors in parallel.

The solving time still fairly high (about 10 min for 1.5s real time simulation) and is thus not suitable for real-time dynamic simulation. However, it solves faster than more complicated tyre models where details of steel wires, etc. is included in the model (Ghoreishy, 2009).

7

Conclusions and recommendations

The most recent developments in tyre modelling were investigated. Tyre models developed to date require a fair amount of data before an accurate representation of the tyre can be obtained. Possibilities of the development of a simplified FE model using data from experiments were investigated in this work.

Global behaviour of “off-road” model was analysed by performing various experimental tests. A model was developed that can accurately represent static tyre behaviour on a flat surface with different cleats. The model was validated using sidewall deformation profiles of the tyre upon loading and load vs. displacement curves (obtained experimentally) for different loading conditions.

The tyre studied was a Continental “off-road” tyre. Laser displacement transducers were used to measure profiles of the tread and the sidewall of the tyre. The sidewall profile was also validated using stereo photogrammetry. The values obtained from the measurements were used to develop a solid model that was used as input for the geometry of the FE model of the tyre.

Initial material characteristics were determined experimentally. Shore hardness tests were performed to gain an idea of how many different rubber materials exist in the tyre. Tensile tests were performed on segments of the sidewall, the tread, and the apex region of the tyre. The non-linear stiffnesses in different orthogonal directions of the sidewall and tread of the tyre were obtained.

Simple FE models of the samples were built to test the superimposing of elements to simulate different material properties in the three different orthogonal directions for the tread and for the sidewall of the tyre. Non-linear material properties were used to represent the rubber characteristics. Elements with linear orthogonal material properties were superimposed onto the non-linear rubber elements to simulate the effect of the added stiffness due to steel wires, nylon threads, etc. The geometry and material characteristics were used as input for the tyre model developed.

Various experimental tests were performed to obtain load vs. displacement curves (global radial stiffness of the tyre). A plate with 6 different cleats laterally and longitudinally mounted onto it was pushed radially against the tyre to measure radial forces experienced upon displacement caused by imperfections/bumps in the road. Sidewall profiles were also measured using lasers (at zero load, 5 kN, 10 kN, 15 kN) whilst the plate and cleats were pushed against the tyre.

A FE model was developed using the global equivalent material properties of sidewall and tread. The same superimposed elements used in the tyre segment test models were used in the three-dimensional model developed.

Various alterations in the material properties of the tyre model were investigated to obtain properties that gave the best fit for the load vs. displacement curves and for the sidewall deformation profiles. The combination of material properties that gave the most accurate results was determined.

The main focus of the project was to develop a tyre model from data obtained from laser and photogrammetry measurements in a laboratory that accurately represents tyre behaviour due to radial forces. The following were achieved with this study:

- Experimental methods were established for testing. Optical measuring techniques were used to gather input and validation data for the tyre model.
- Accurately measured deformation profiles and load vs. displacement curves of the tyre was used to verify the tyre models behaviour.
- Developed a finite element model that can simulate the effect of radial forced and obstacles on a tyre.
- Investigated the use of two subsets of elements, superimposed onto each other to simulate global material properties of the rubbers, steel wires, polyester threads and nylon threads.

The final FE model can successfully predict the vertical force vs. displacement, as well as side wall deformation of the tyre under static loading conditions on both a flat surface and various different cleats.

It is clear from the results of this study that equivalent (global) material properties can be used to simulate the composite properties of the materials in tyres. Usually a tyre has a structure that can be divided into a few segments that each has its own material structure right through the region. These regions can be characterized by simple tests and the input can be used as a first estimation of the tyre's material properties for the model. Accurate validation criteria should be used to validate the tyre model if time does not allow for excessive testing of the material properties of all the rubber, steel wires, polyester threads, etc. Geometric displacement data at various loading conditions can be used for validation of the tyre model.

For future studies it is recommended that different element types be investigated in the tyre model. An Adams body can also be generated from the FE program, MSC.Marc,) which contains the description of the component's flexibility. The models can then be introduced into Adams in later studies. The model developed can be used to investigate the effect of different stiffnesses and other material changes in the sidewall or tread of a tyre.

References

Abe, M. & Manning, W., 2009. *Vehicle Handling Dynamics.* 1st ed. Amsterdam: Elsevier Ltd..

ANSYS, 2007. *ASYS theory manual 2007 Version 11.* USA: ANSYS Inc..

Badalamenti, J. & Doyle, G., 1988. Radial-interradial spring tire models. *Journal of Vibration, Acoustic, Stress and Reliability in Design,* 110(1), pp. 70-75.

Besselink, I., 2006. Vehicle dynamics analysis using SimMechanics and TNO Delft-Tyre. *TNO Automotive*.

Boulanger, P. & Hayes, M., 1998. Poisson's Ratio for Orthorhombic Materials. *Journal of Elasticity,* Volume 50, pp. 87-89.

Cerrolaza, M. & Osorio, J., 2012. Relations among stiffness coefficients of hexahedral 8-noded finite elements: A simple and efficient way to reduce the integration time. *Finite Elements in Analysis and Design,* Volume 55, pp. 1-6.

Daly, S. H., 2010. Digital Image Correlation in Experimental Mechanics for Aerospace Materials and Structures. *Encyclopedia of Aerospace Engineering.*

Darnell, I., Hulbert, G. M. & Mousseau, C. W., 1997. An efficient three-dimensional tire model for vehicle dynamics simulations. *Mechanics of Structures and Machines,* 25(1), pp. 1-19.

Drescher, A., Newcomb, D. & Heimdahl, T., 1999. *Deformability of shredded tires,* Minnesota: Minnesota Department of Transportation.

Edeskär, T., 2004. *Technical and environmental properties of tyre shreds focussing on ground engineering applications,* Luleå: Luleå University of Technology.

Gent, A., 2007. *Mechanical properties of rubber.* Köln, Presentation, 32th Tire Mechanics Short Course.

Gent, A. N. & Walter, J. D., 2005. *National highway traffic safety administration.* [Online] Available at: www.nhtsa.gov/staticfiles/safercar/pdf/PneumaticTire_HS-810-561.pdf [Accessed 16 March 2014].

Ghoreishy, H. R., 2008. A State of the Art Review of the Finite Element Modelling of Rolling Tyres. *Iranian Polymer Journal,* 17(8), pp. 571-597.

Ghoreishy, M. H. R., 2009. Finite Element Modelling of the Steady Rolling of a Tyre with Detailed Tread Pattern. *Iranian Polymer journal,* 18(8), pp. 641-650.

Gipser, M., 1999. *FTire, a New Fast Model for Ride Comfort Simulations.* Berlin, Germany, s.n.

Gipser, M., 2000. *ADAMS/FTire - A Tire Model for Ride & Durability Simulations.* Tokyo, s.n.

Gipser, M., 2007. FTire - the simulation model for all applications related to vehicle dynamics. *Vehicle system dynamics,* 45(1), pp. 139-151.

GOM Optical Measuring Techniques, 2007. *Aramis v 5.3.0 User Manual,* Braunschweig: GOM.

GOM Optical Measuring Techniques, 2008. *Pontos v 6.2 User Manual,* Braunschweig: GOM.

Hölschner, H. et al., 2004. Modeling of pneumatic tires by a finite element model for the development a tire friction remote sensor. *Computers and structures.*

Hua, J. & White, T., 2002. Study of nonlinear tire contact pressure effects on HMA rutting. *International Journal of Geomechanics,* 2(3), pp. 353-376.

Kilner, J., 1982. Pneumatic tire model for aircraft simulation. *Journal of aircraft,* 19(10), pp. 851-857.

Kindt, P., Sas, P. & Desmet, W., 2008. Three-dimensional Ring Model for the Prediction of the Tyre Dynamic Behaviour. *Proceedings of ISMA,* pp. 4155-4170.

Kindt, P., Sas, P. & Desmet, W., 2009. Measurement and analysis of rolling tire vibrations. *Optics and Lasers in Engineering,* Volume 47, pp. 443-453.

Kohlhauser, C. & Hellmich, C., 2012. Determination of Poisson's ratios in isotropic, transversely isotropic, and orthotropic materials by means of combined ultrasonic-mechanical testing of normal stiffnesses: Application to metals and wood. *European Journal of Mechanics A/Solids,* Volume 33, pp. 82-98.

Kondé, A. K. et al., 2013. On the modeling of aircraft tire. *Aerospace Science and Technology,* Volume 27, pp. 67-75.

Korunovic, N., Trajanovic, M. & Stojkovic, M., 2008. Finite Element Model for Steady-State Rolling Tire Analysis. *Journal of the Serbian Society for Computational Mechanics,* 2(1), pp. 63-79.

Korunovic, N., Trajjanovic, M. & Stojkovic, M., 2007. FEA of tyres subjected to static loading. *Journal of the Serbian Society for Computational Mechanics,* 1(1), pp. 87-98.

Kostial, P. et al., 2007. *Experimental Modal Analysis of Tyres by ESPI.* Merida, Mexico, IMEKO 20th TC3, 3rd TC16 and 1st TC22 International Conference.

Koutný, F., 2007. *Geometry and mechanics of pneumatic tires,* Zlín: Koutny-Math.

Lee, C. et al., 1997. Validation of a FEA tire model for vehicle dynamic analysis and full vehicle real time proving ground simulations. *SAE Paper Number 971100*, 24 February.

Lee, J., 2011. Finite element modeling of interfacial forces and contact stresses of pneumatic tire on fresh snow for combined longitudinal and lateral slips. *Journal of Terramechanics,* Volume 48, pp. 171-197.

Mc Allen, J., Cuitfio, A. & Sernas, V., 1996. Numerical investigation of deformation characteristics and heat generation in pneumatic aircraft tires Part I Mechanical Modeling. *Finite Elements in Analysis and Design,* 23(2-4), pp. 256-290.

MD Adams, 2010. *Adams.* [Online]
Available at: http://ti.mb.fh-

osnabrueck.de/adamshelp/mergedProjects/tire/tire_models/html_version/swift/1_tyre_model_overview.htm
[Accessed March 2011].

Merzouki, R., Ould-Bouamama, B., Djeziri, M. & Bouteldja, M., 2007. Modelling and estimation of tire-road longitudinal impact efforts using bond graph approach. *Mechatronics,* Volume 17, pp. 93-108.

MF-Tyre & MF-Swift 6.1 Users Manual, 2008. *http://www.delft-tyre.nl/.* [Online].

Miège, A. J. P. & Popov, A. A., 2004. *Truck tyre rolling resistance under dynamic vertical load,* Nottingham: University of Nottingham.

Mohsenimanesh, A., Ward, S. & Gilchrist, M., 2009. Stress analysis of a multi-laminated tractor tyre using non-linear 3D finite element analysis. *Materials and Design,* 30(4), pp. 1124-1132.

Moser, R. A., Sube, H. J., Turner, J. L. & Zakelji, P., 2010. 3D Digital Imaging Correlation: Applications to tire testing. *Tire science and technology,* 38(2), pp. 100-118.

Moser, R. & Lightner, J. G., 2006. *Using 3D Digital Imaging Correlation Techniques to Validate Tire FEM.* s.l., SEM Annual Conference.

MSC.Software, 2010. *Nonlinear Finite Element Analysis of Elastomers - White Paper.* Santa Ana: MSC.Software.

Nakashima, H. & Wong, J., 1993. A three-dimensional tire model by the Finite Element Method. *Journal of Terramechanics.*

Oertel, C. & Fandre, A., 1999. *Ride comfort simulations and steps towards life time calculations: RMOD-K and ADAMS.* Berlin, MSC Software.

Orteu, J.-J., 2009. 3-D computer vision in experimental mechanics. *Optics and Lasers in Engineering,* 47(3-4), pp. 282-291.

Pacejka, H. B., 2006. *Tyre and vehicle dynamics.* Second ed. Burlington: Elsevier.

Pacejka, H. B., 2006. *Tyre and Vehicle Dynamics.* Second ed. Butterworth-Heinemann: Elsevier Science Technology.

Pacejka, H. & Bakker, E., 1993. The Magic Formula Tyre Model.

Purslow, P. P., 2011. Poisson ratios in anisotropic materials at finite strains; comment on short communication by Smith et al. (2011). *Journal of Biomechanics.*

RMOD-K, 2011. *RMOD-K 7.* [Online]
Available at: http://rmod-k.com/index.php?option=com_content&view=article&id=49:flexiblebelt&catid=24:flexiblebelt&Itemid=79
[Accessed 2011].

Sasso, M., Palmieri, G., Chiappini, G. & Amodio, D., 2008. Characterization of hyperelastic rubber-like materials by biaxial and uniaxial stretching tests based on optical methods. *Polymer Testing,* Volume 27, pp. 995-1004.

Senatore, C. & Sandu, C., 2011. Off-road tire modeling and the multi-pass effect for vehicle dynamics simulation. *Journal of Terramechanics,* Volume 48, pp. 265-276.

Sugiyama, H. & Suda, Y., 2009. Non-linear elastic tyre model using the absolute nodal coordinate formulation. *Journal of Multi-body dynamics,* pp. 211-219.

Ting, T., 2004. Very Large Poisson's Ratio with a Bounded Transverse Strain in Anisotropic Elastic Materials. *Journal of Elasticity,* Volume 77, pp. 163-176.

Ting, T. & Chen, T., 2004. Poisson's ratio for anisotropic elastic materials can have no bounds. *Jl Mech. Appl. Math.,* 58(1), pp. 73-82.

Tönük, E. & Ünlüsoy, Y., 2001. Prediction of automobile tire cornering force characteristics by finite element modeling and analysis. *Computers & Structures,* 79(13), pp. 1219-1232.

Tschoegl, N., 1971. Constitutive Equations for Elastomers. *Journal of polymer science,* Volume 9, pp. 1959-1970.

Voyyiadjis, G. Z. & Kattan, P. I., 2005. *Mechanics of Composite Materials with MATLAB.* New York: Springer Berlin Heidelberg.

Xia, K., 2011. Finite element modeling of tire/terrain interaction: Application to predicting soil compaction and tire mobility. *Journal of Terramechanics,* Volume 48, pp. 113-123.

Yan, X., 2001. Non-linear three-dimensional finite element modeling of radial tires. *Mathematics and Computers in Simulation,* 58(1), pp. 51-70.

Yan, X., Wang, Y. & Feng, X., 2002. Study for the endurance of radial truck tires with finite element modeling. *Mathematics and Computers in Simulation,* 59(6), pp. 471-488.

Zegelaar, P. W. A., 1998. *The dynamic response of tyres to brake torque variations and road unevennesses, PhD thesis,* Delft, The Netherlands: Delft University of Technology.

Zhang, X., Rakheja, S. & Ganesan, R., 2002. Stress Analysis of the multi-layered system of a Multi-Layered System of a Truck Tire. *Tire Science and Technology,* 30(4), pp. 240-264.

Zorofski, C. F., 1973. Mathematical Prediction of Dynamic tire Behavior. *Tire Science and Technology,* Volume 1, pp. 99-117.

Appendix A – Load vs. displacement plots

Flat Surface

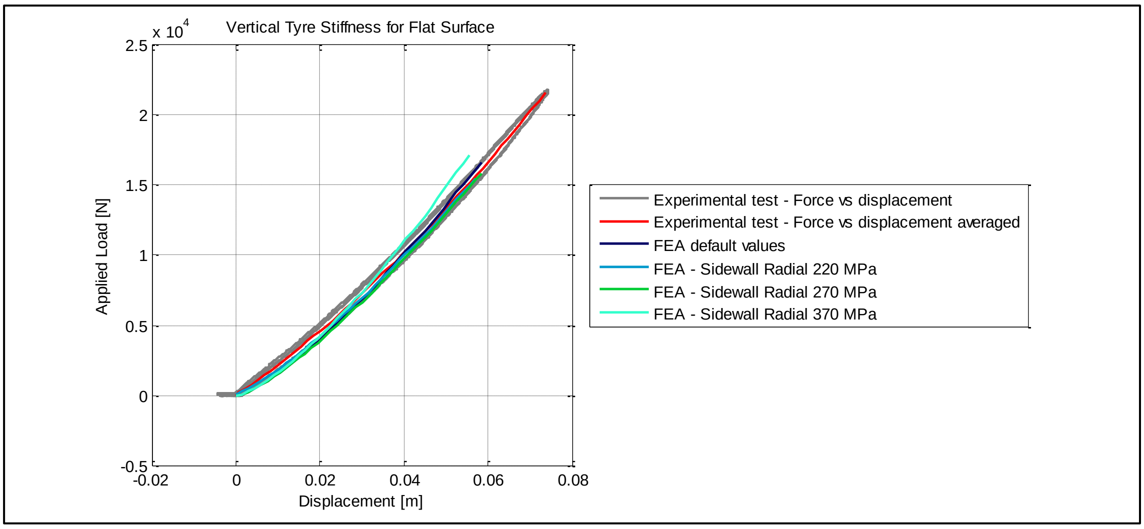

Figure A.1: Load vs. displacement comparison for different radial sidewall stiffnesses on a flat surface

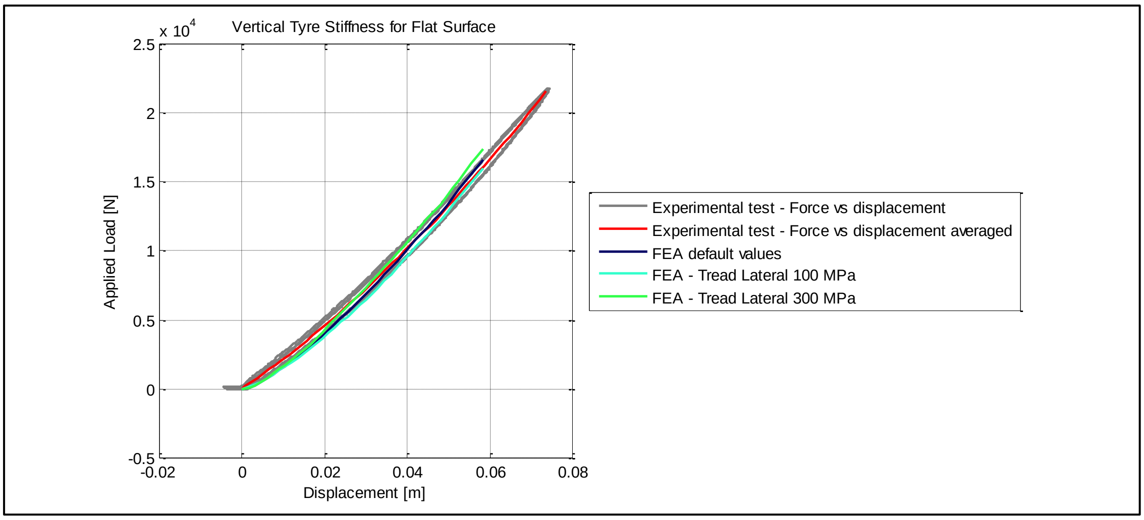

Figure A.2: Load vs. displacement comparison for different lateral tread stiffnesses on a flat surface

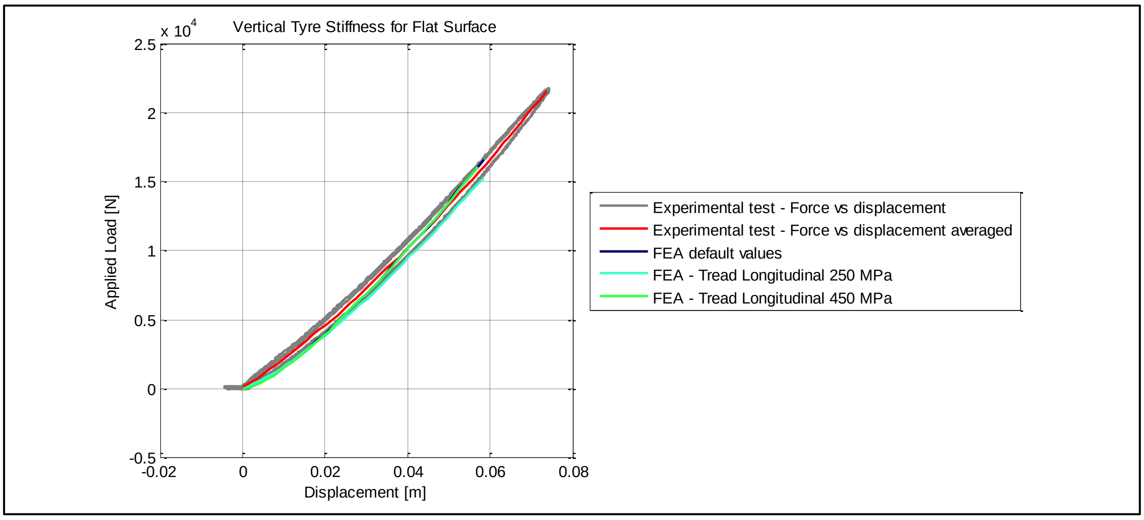

Figure A.3: Load vs. displacement comparison for different longitudinal tread stiffnesses on a flat surface

19x19 Lateral cleat

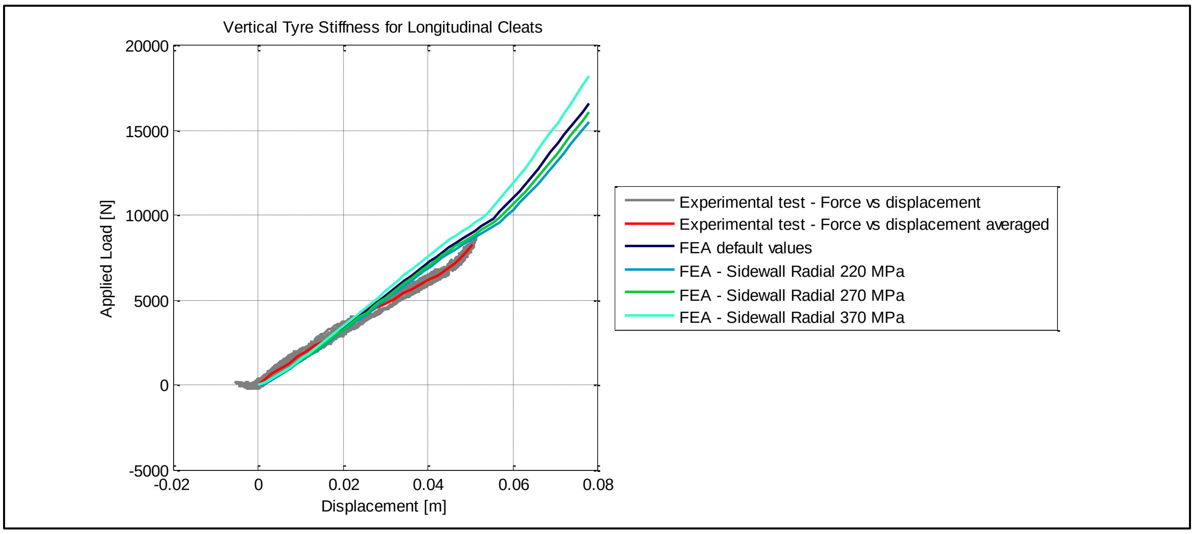

Figure A.4: Comparison for different radial sidewall stiffnesses on a 19mm x 19mm lateral cleat

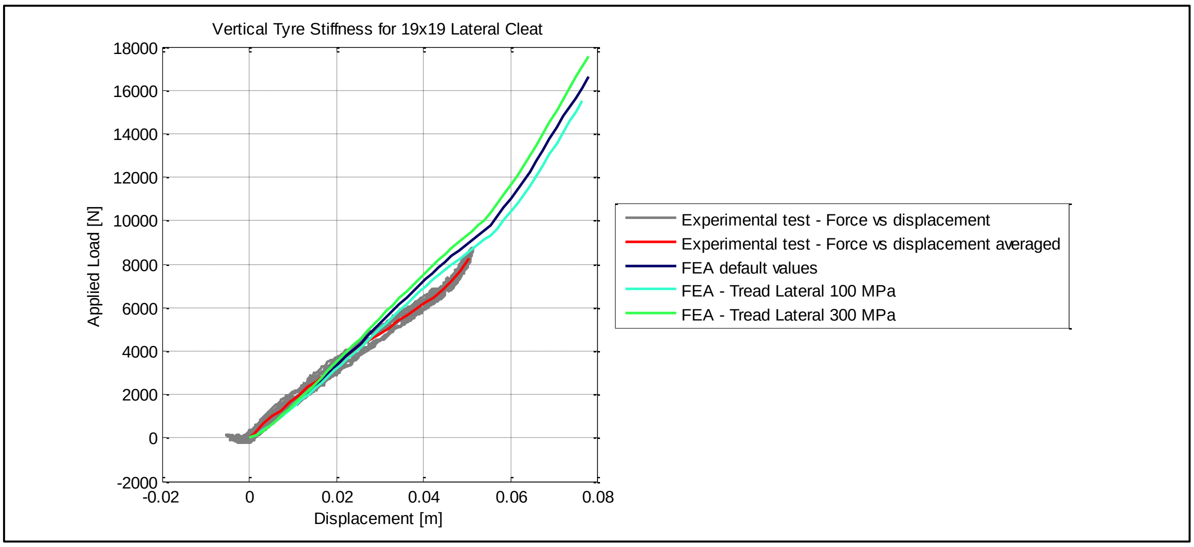

Figure A.5: Comparison for different lateral tread stiffnesses on a 19mm x 19mm lateral cleat

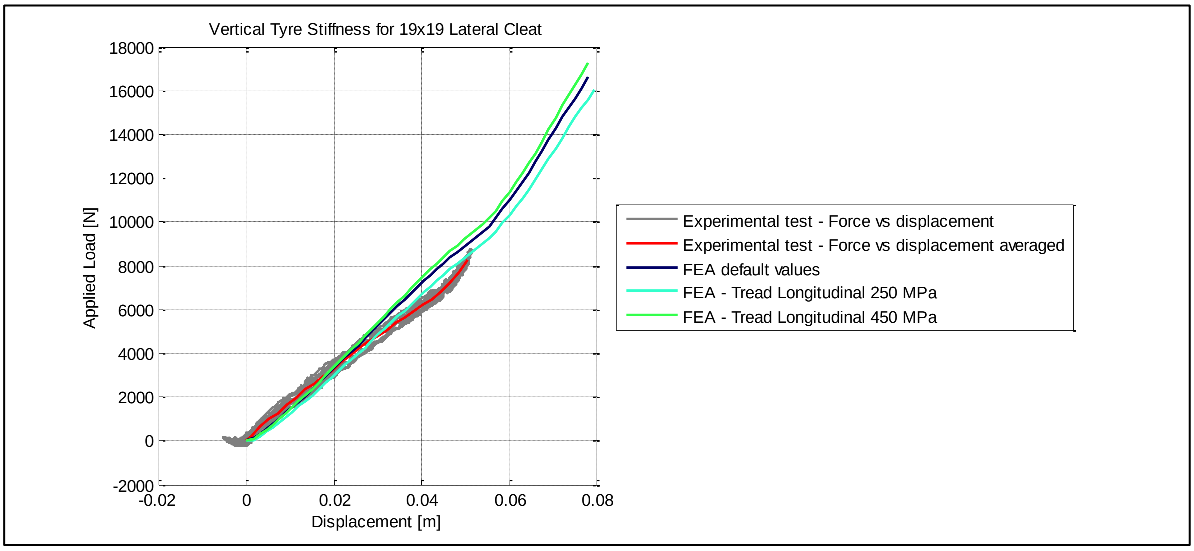

Figure A.6: Comparison for different longitudinal tread stiffnesses on a 19mm x 19mm lateral cleat

19x19 Longitudinal cleat

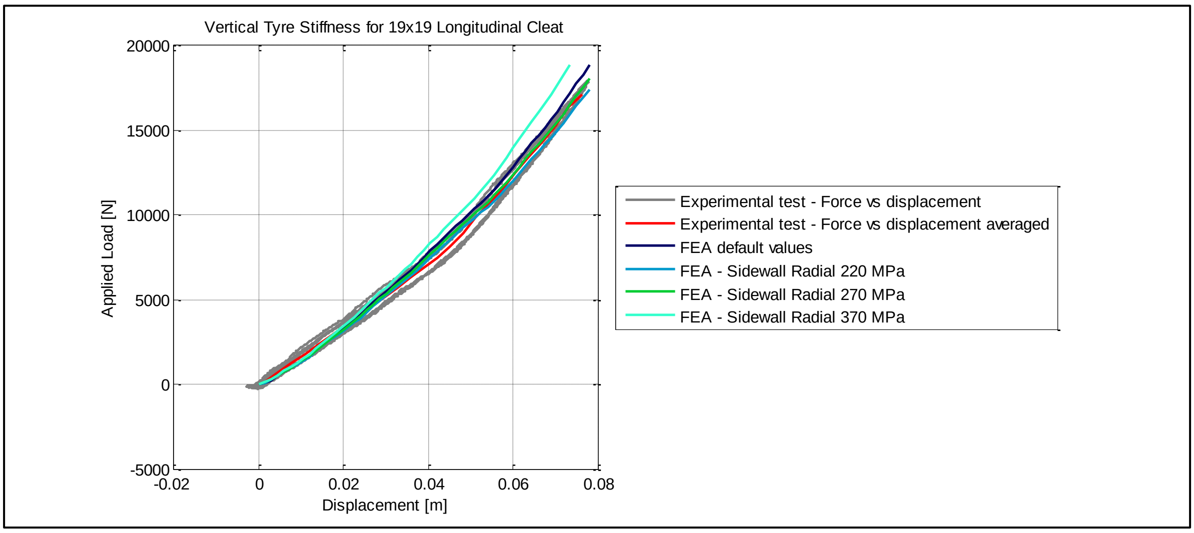

Figure A.7: Comparison for different radial sidewall stiffnesses on a 19mm x 19mm longitudinal cleat

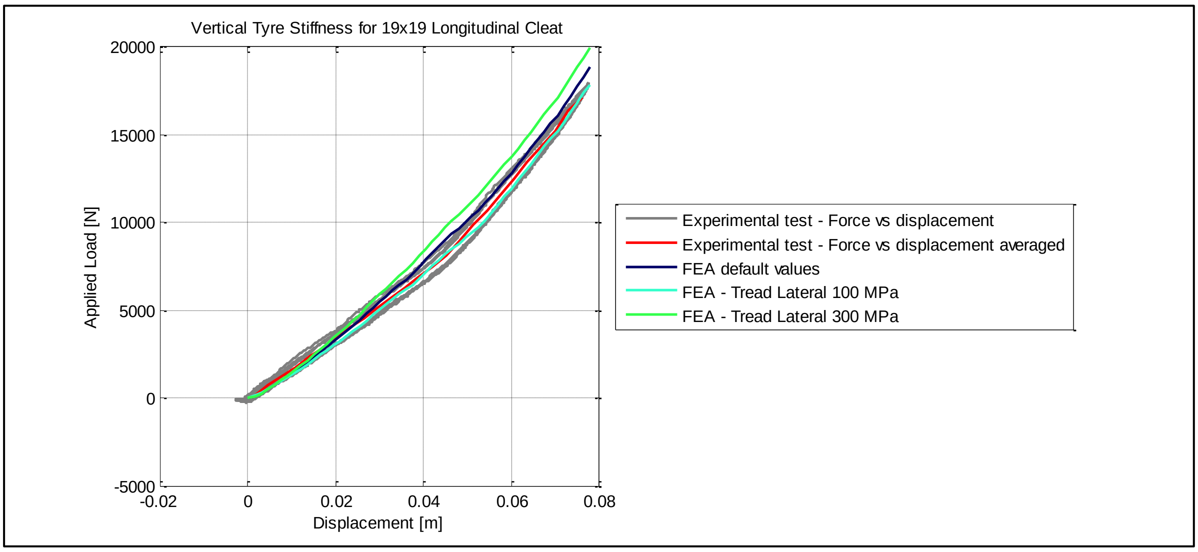

Figure A.8: Comparison for different lateral tread stiffnesses on a 19mm x 19mm longitudinal cleat

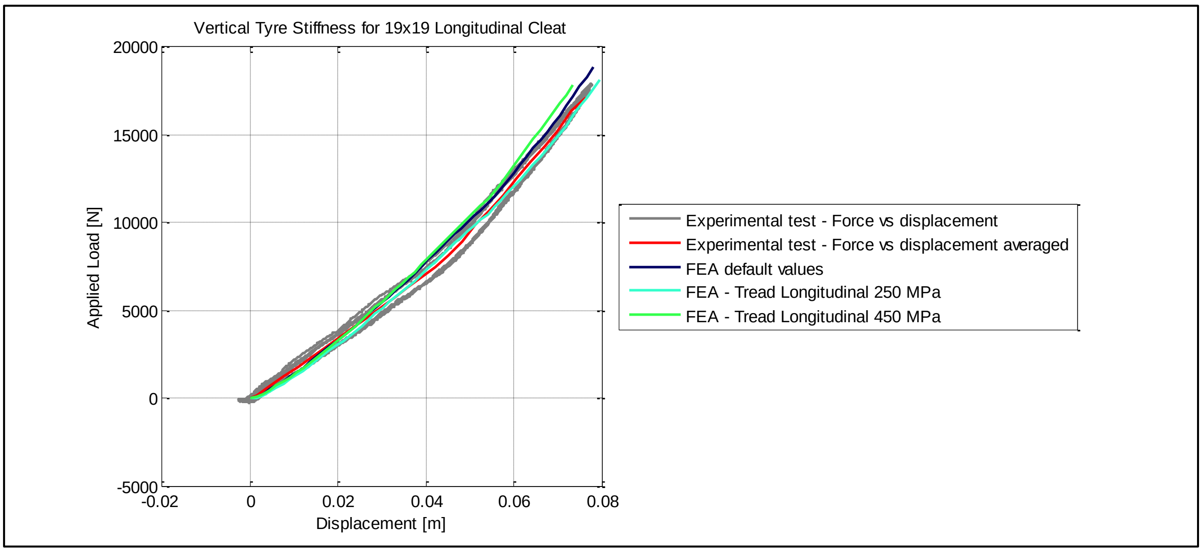

Figure A.9: Comparison for different longitudinal tread stiffnesses on a 19mm x 19mm longitudinal cleat

25x25 Lateral cleat

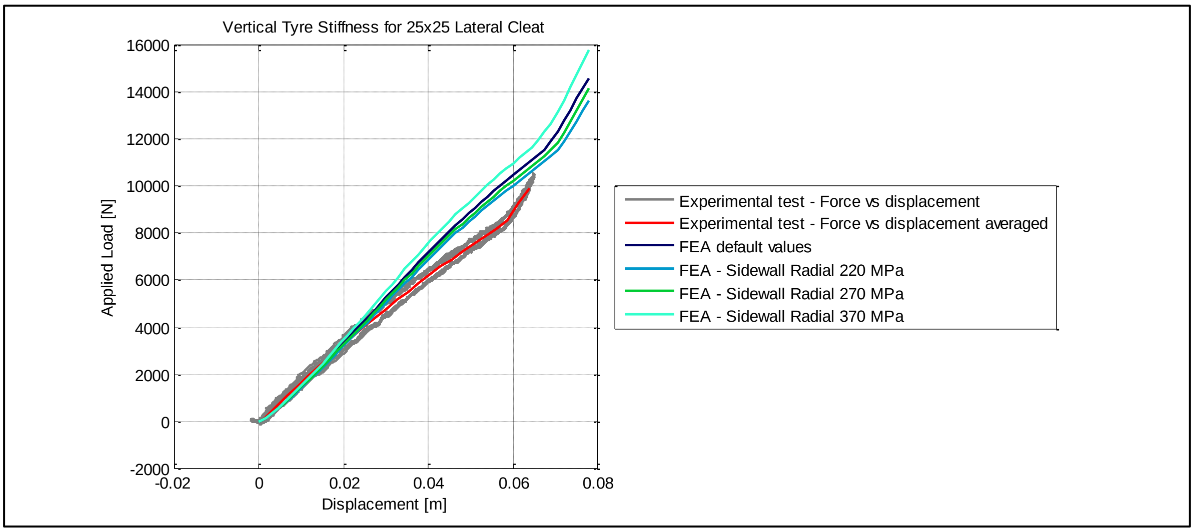

Figure A.10: Comparison for different radial sidewall stiffnesses on a 25mm x 25mm lateral cleat

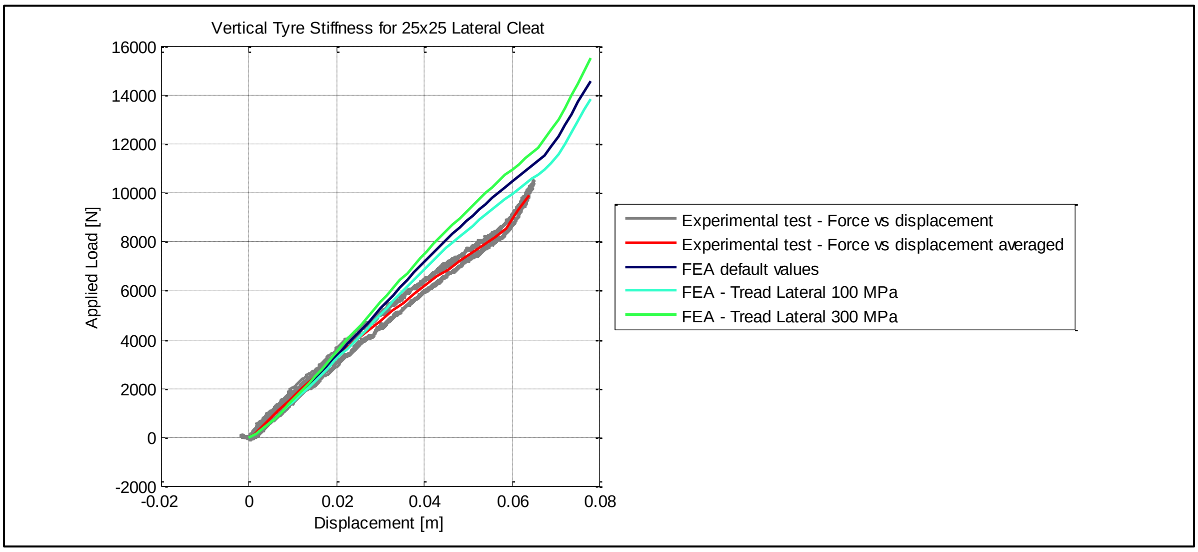

Figure A.11: Comparison for different lateral tread stiffnesses on a 25mm x 25mm lateral cleat

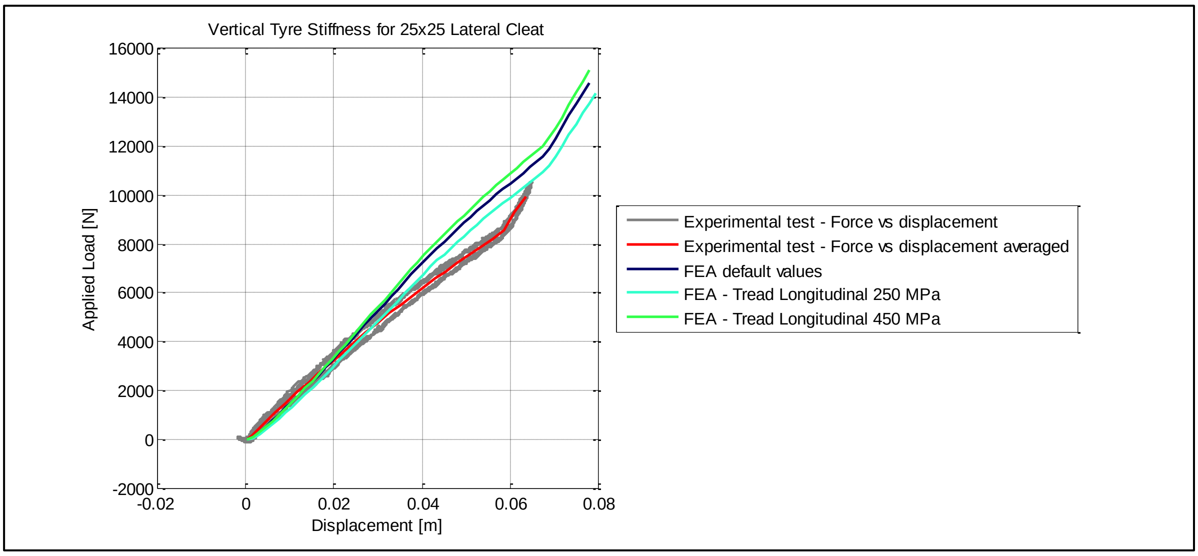

Figure A.12: Comparison for different longitudinal tread stiffnesses on a 25mm x 25mm lateral cleat

25x25 Longitudinal cleat

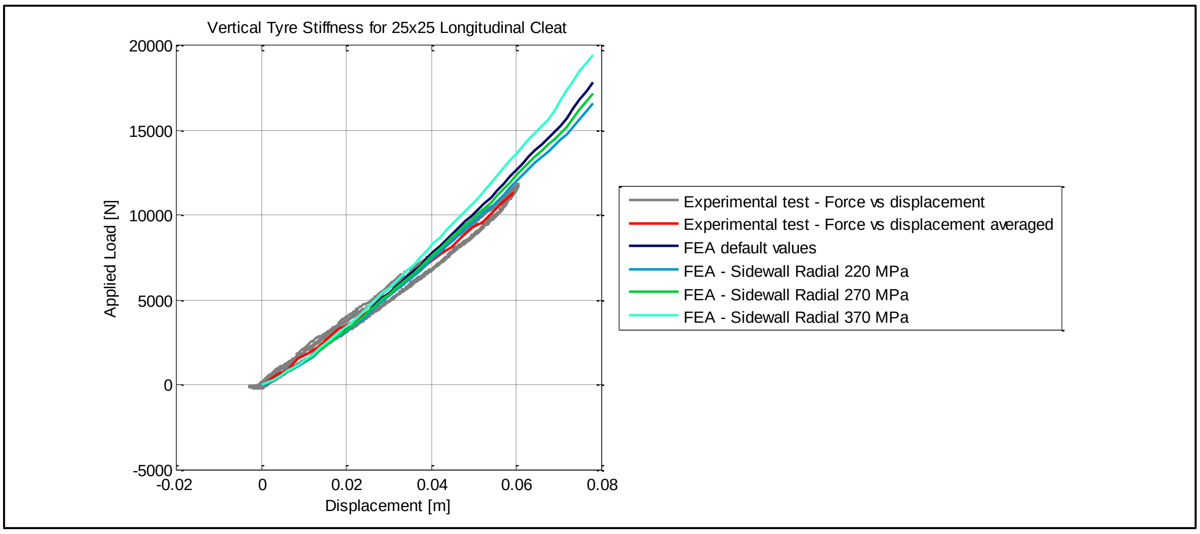

Figure A.13: Comparison for different radial sidewall stiffnesses on a 25mm x 25mm longitudinal cleat

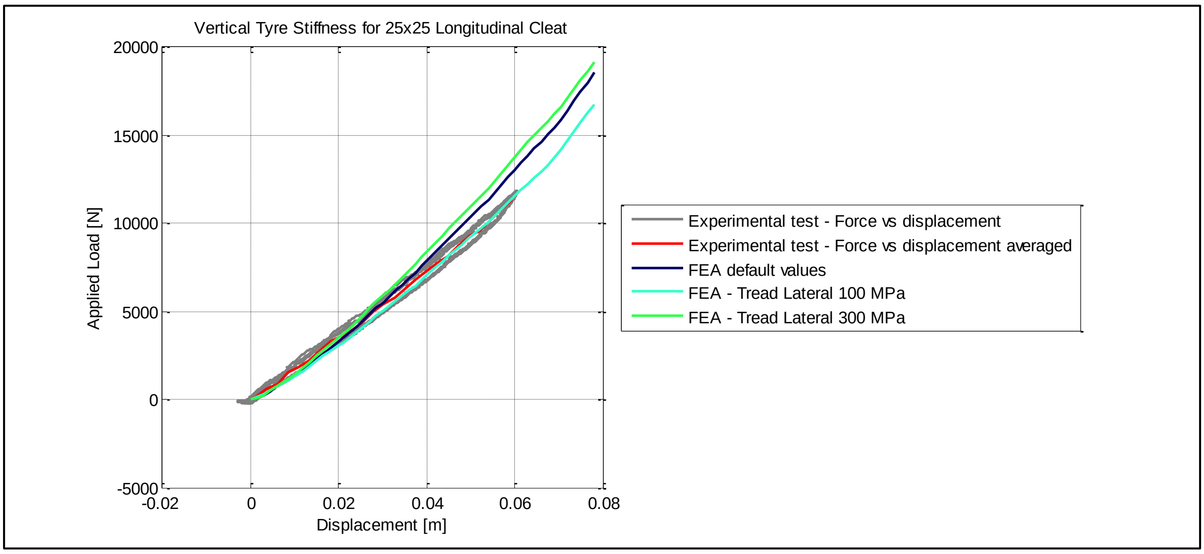

Figure A.14: Comparison for different lateral tread stiffnesses on a 25mm x 25mm longitudinal cleat

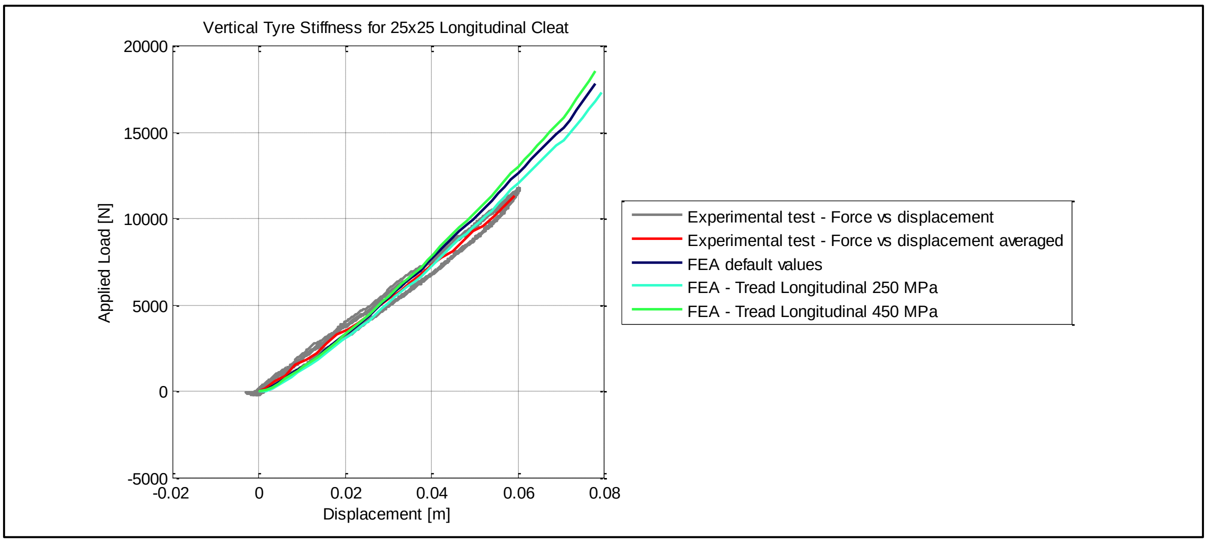

Figure A.15: Comparison for different longitudinal tread stiffnesses on a 25mm x 25mm longitudinal cleat

38x38 Lateral cleat

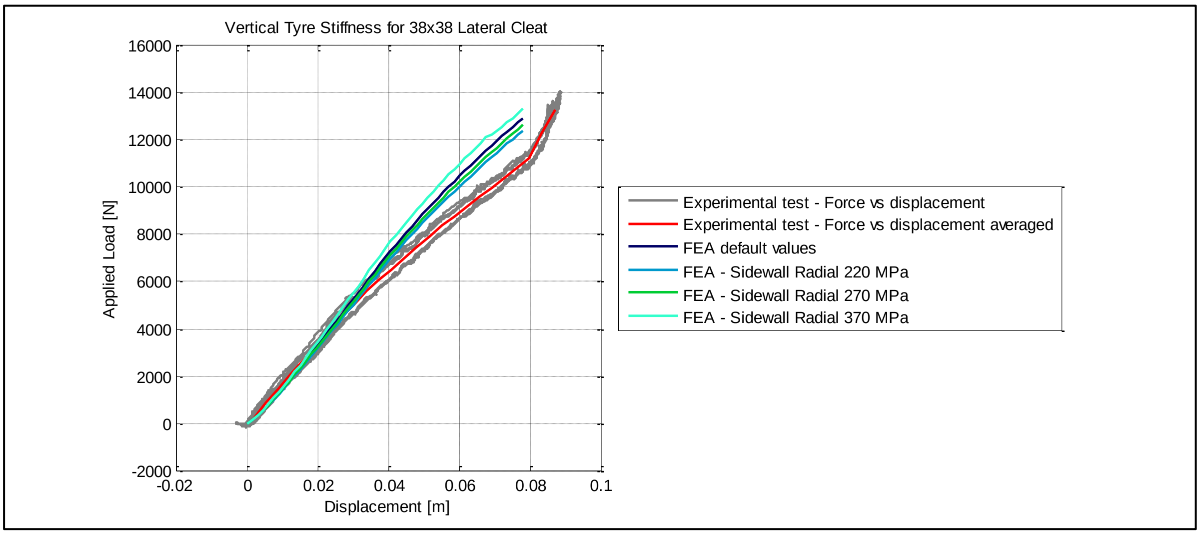

Figure A.16: Comparison for different radial sidewall stiffnesses on a 38mm x 38mm lateral cleat

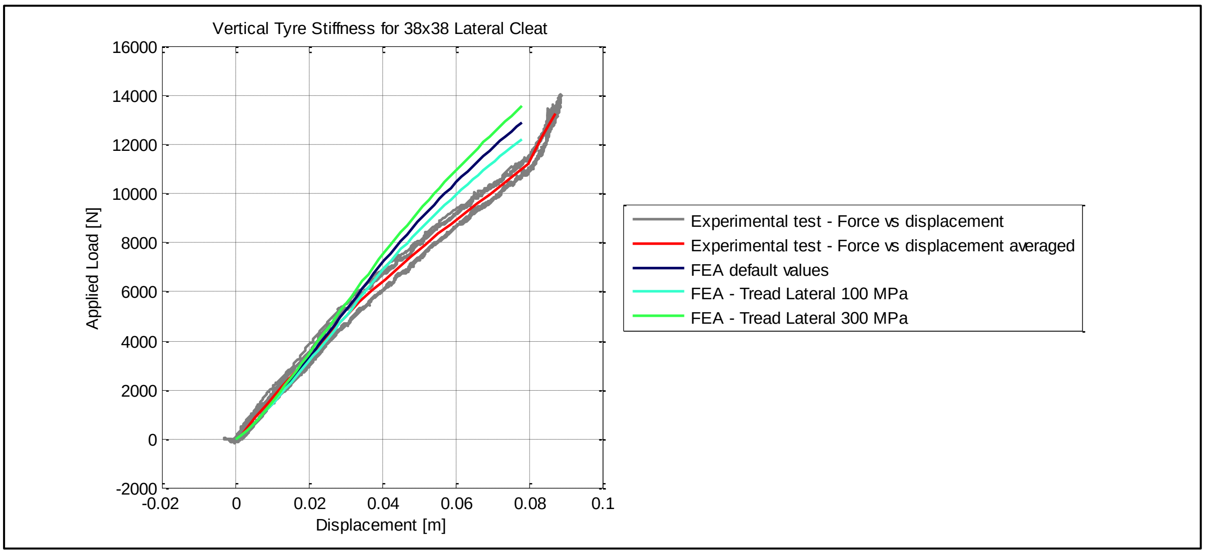

Figure A.17: Comparison for different lateral tread stiffnesses on a 38mm x 38mm lateral cleat

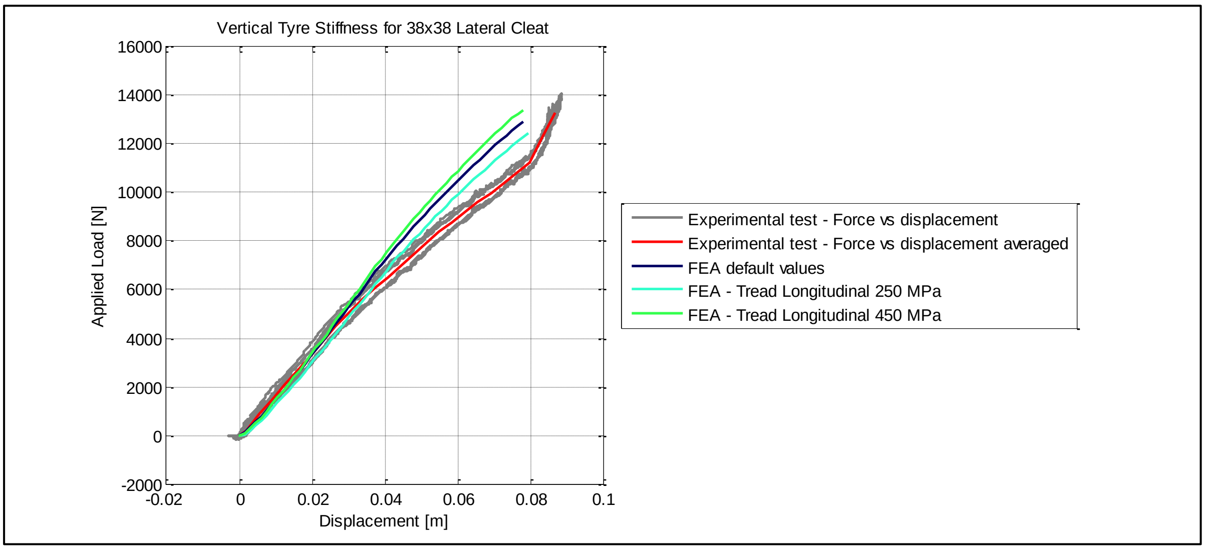

Figure A.18: Comparison for different longitudinal tread stiffnesses on a 38mm x 38mm lateral cleat

38x38 Longitudinal cleat

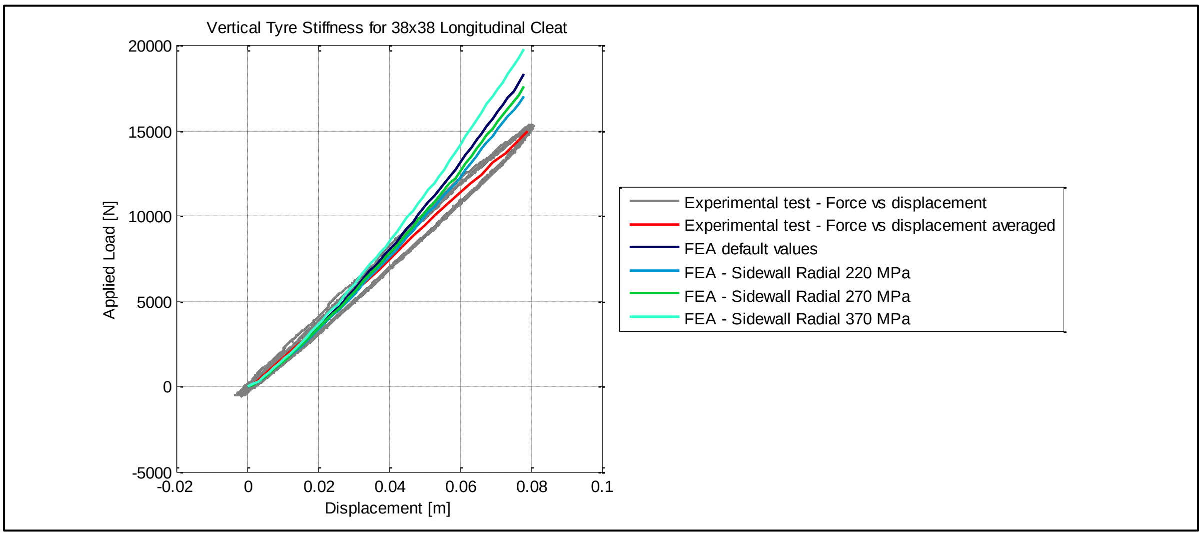

Figure A.19: Comparison for different radial sidewall stiffnesses on a 38mm x 38mm longitudinal cleat

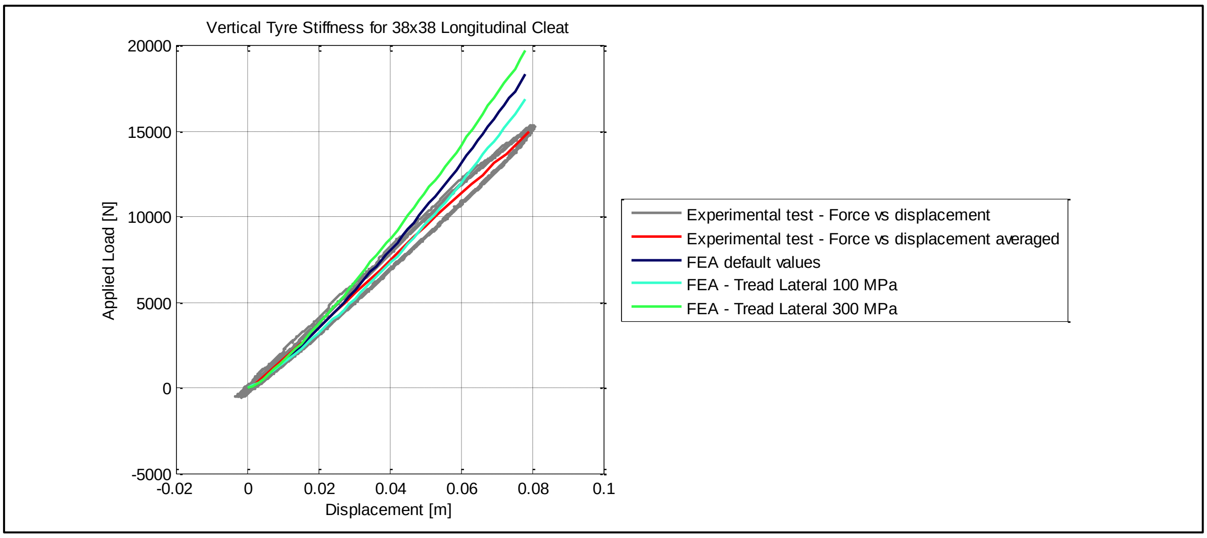

Figure A.20: Comparison for different lateral tread stiffnesses on a 38mm x 38mm longitudinal cleat

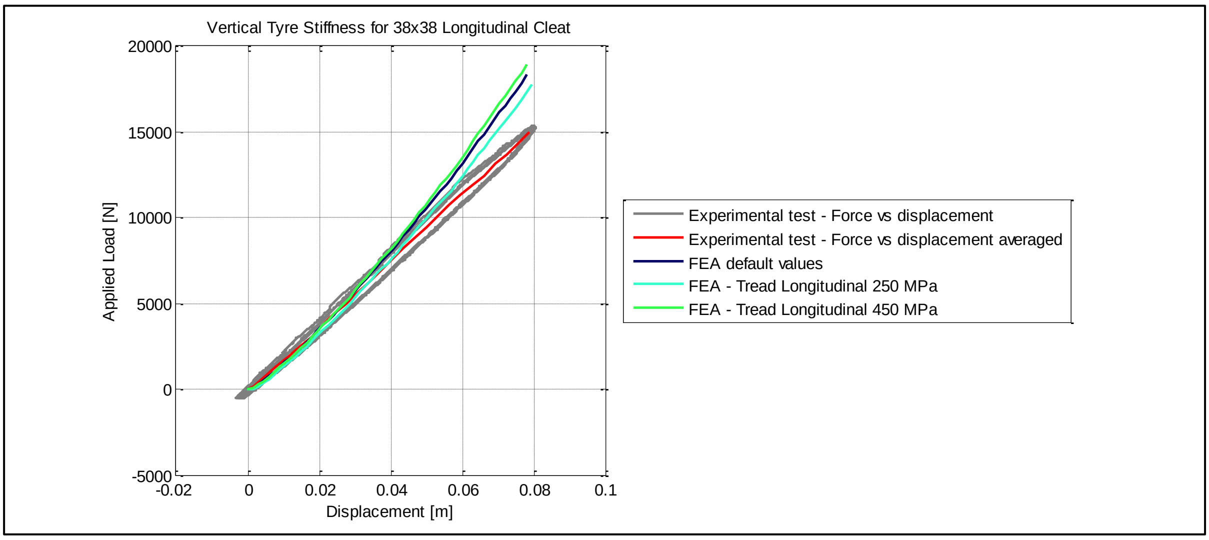

Figure A.21: Comparison for different longitudinal tread stiffnesses on a 38mm x 38mm longitudinal cleat

51x51 Lateral cleat

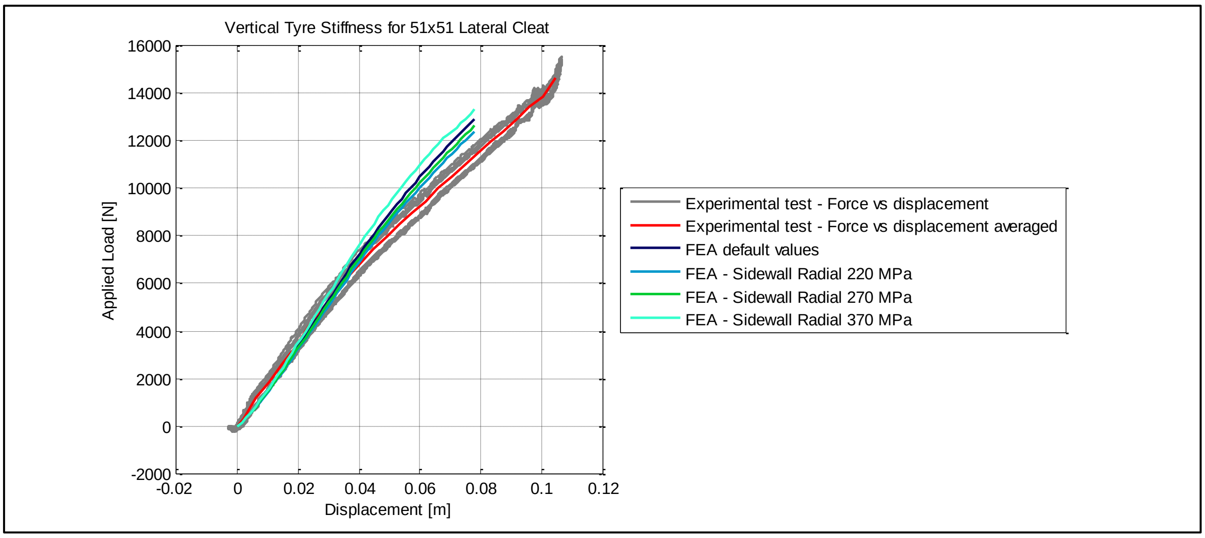

Figure A.22: Comparison for different radial sidewall stiffnesses on a 51mm x 51mm lateral cleat

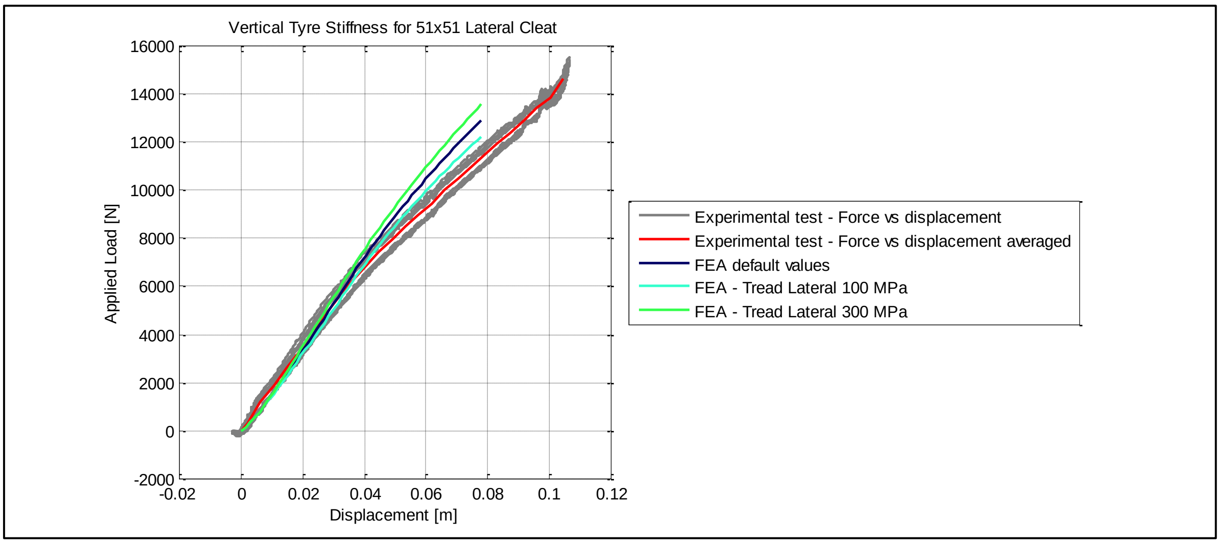

Figure A.23: Comparison for different lateral tread stiffnesses on a 51mm x 51mm lateral cleat

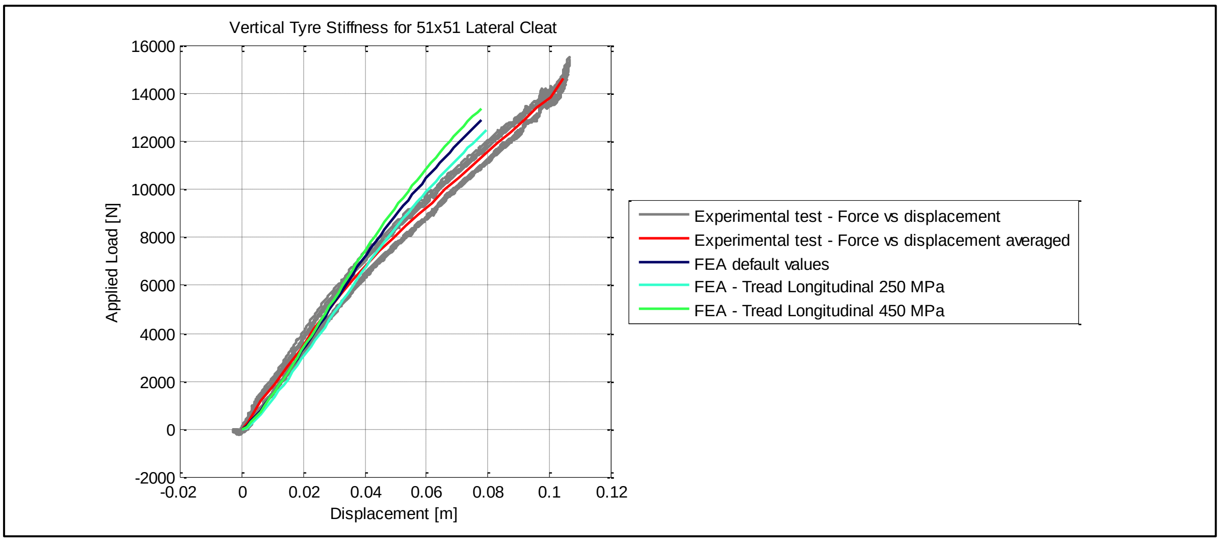

Figure A.24: Comparison for different longitudinal tread stiffnesses on a 51mm x 51mm lateral cleat

51x51 Longitudinal cleat

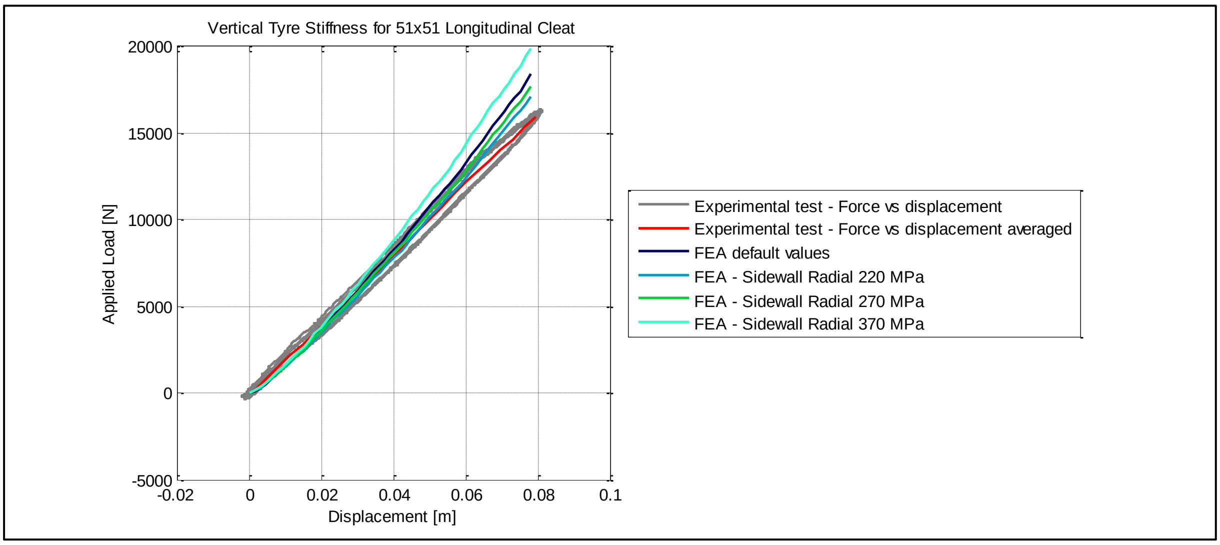

Figure A.25: Comparison for different radial sidewall stiffnesses on a 51mm x 51mm longitudinal cleat

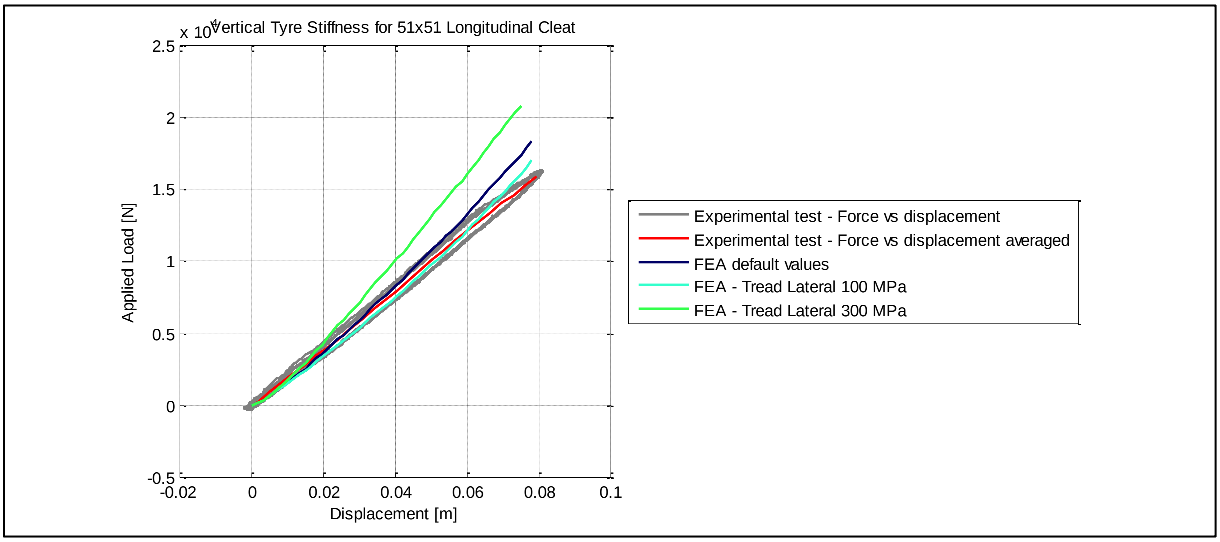

Figure A.26: Comparison for different lateral tread stiffnesses on a 51mm x 51mm longitudinal cleat

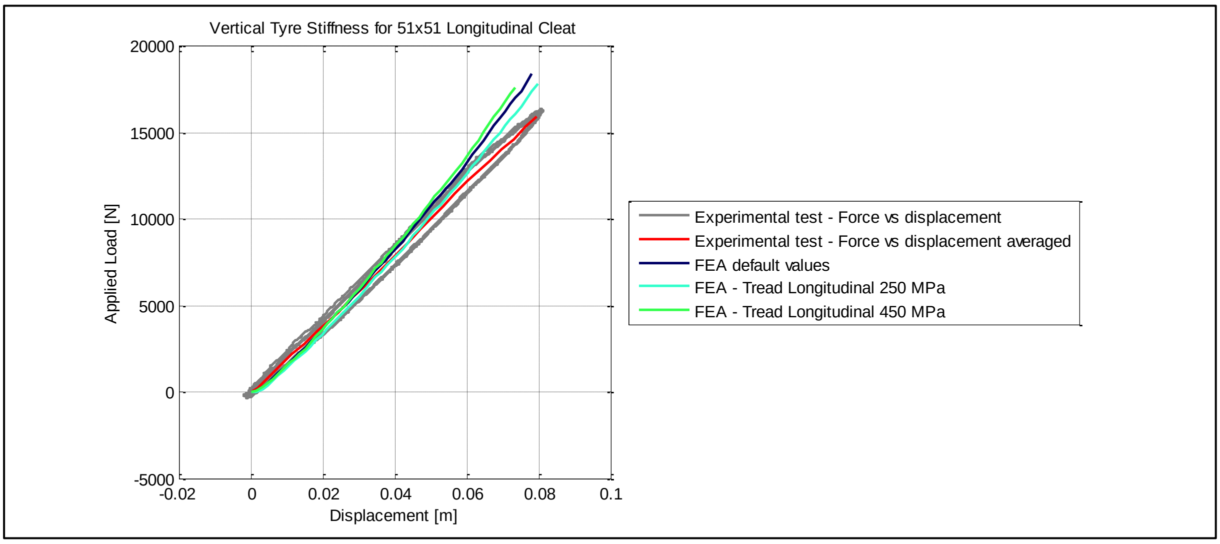

Figure A.27: Comparison for different longitudinal tread stiffnesses on a 51mm x 51mm longitudinal cleat

76x76 Lateral cleat

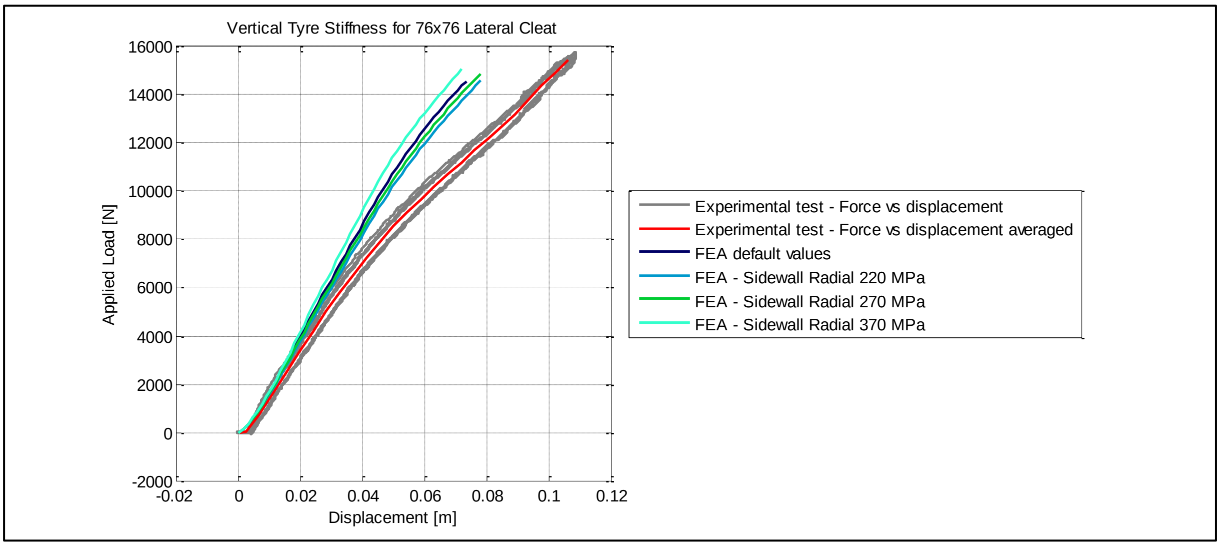

Figure A.28: Comparison for different radial sidewall stiffnesses on a 76mm x 76mm lateral cleat

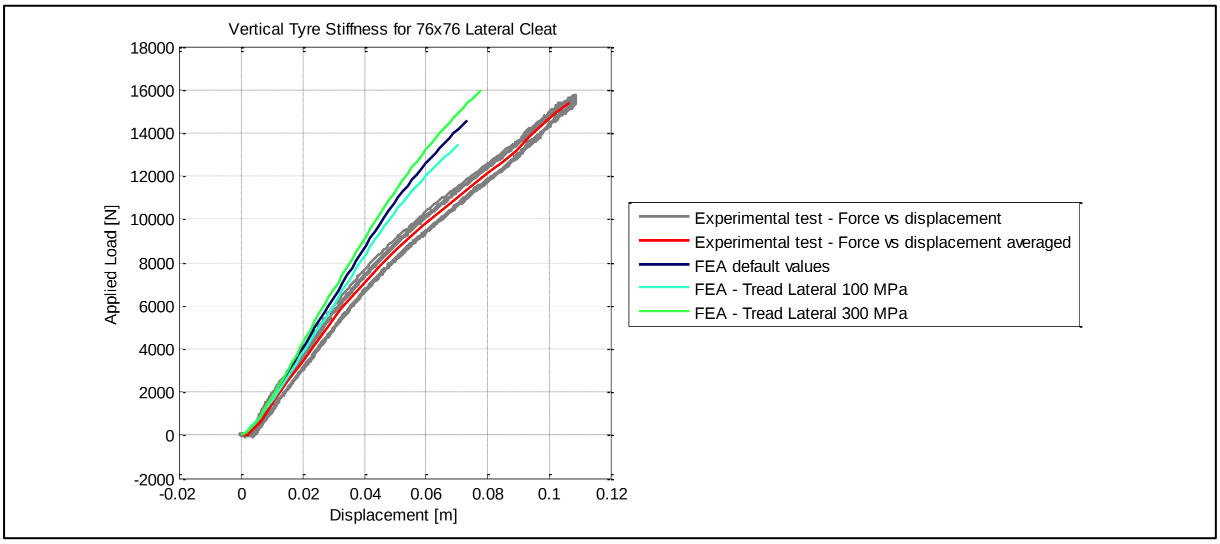

Figure A.29: Comparison for different lateral tread stiffnesses on a 76mm x 76mm lateral cleat

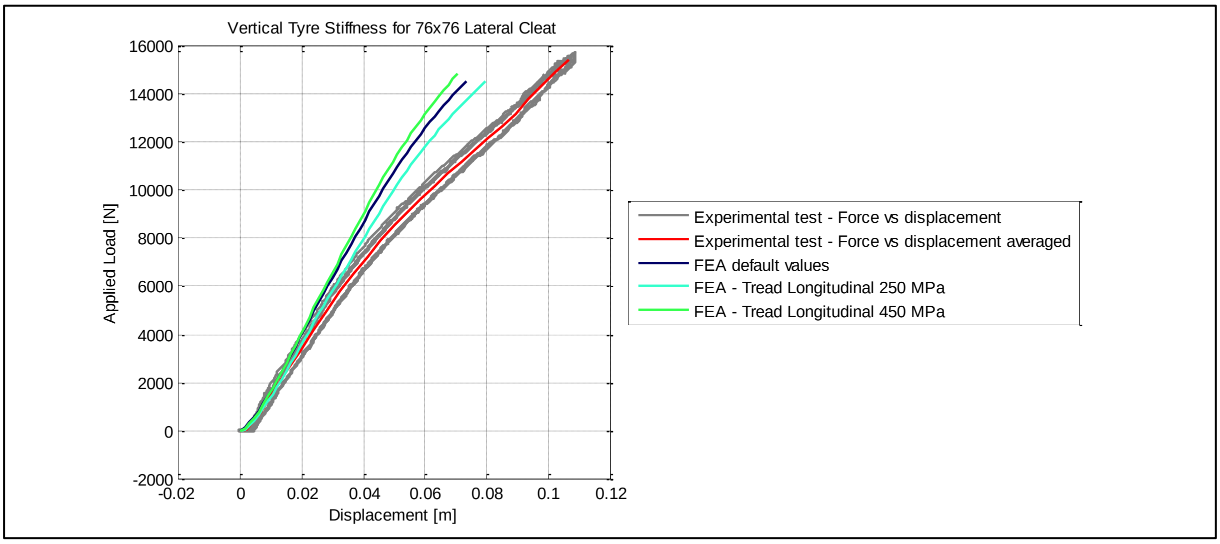

Figure A.30: Comparison for different longitudinal tread stiffnesses on a 76mm x 76mm lateral cleat

76x76 Longitudinal cleat

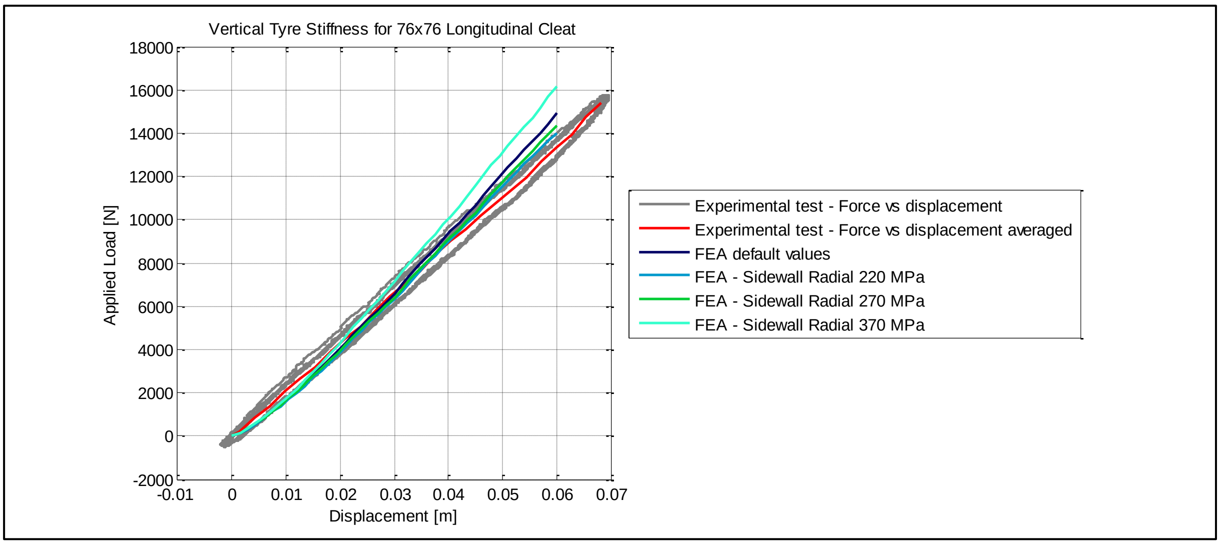

Figure A.31: Comparison for different radial sidewall stiffnesses on a 76mm x 76mm longitudinal cleat

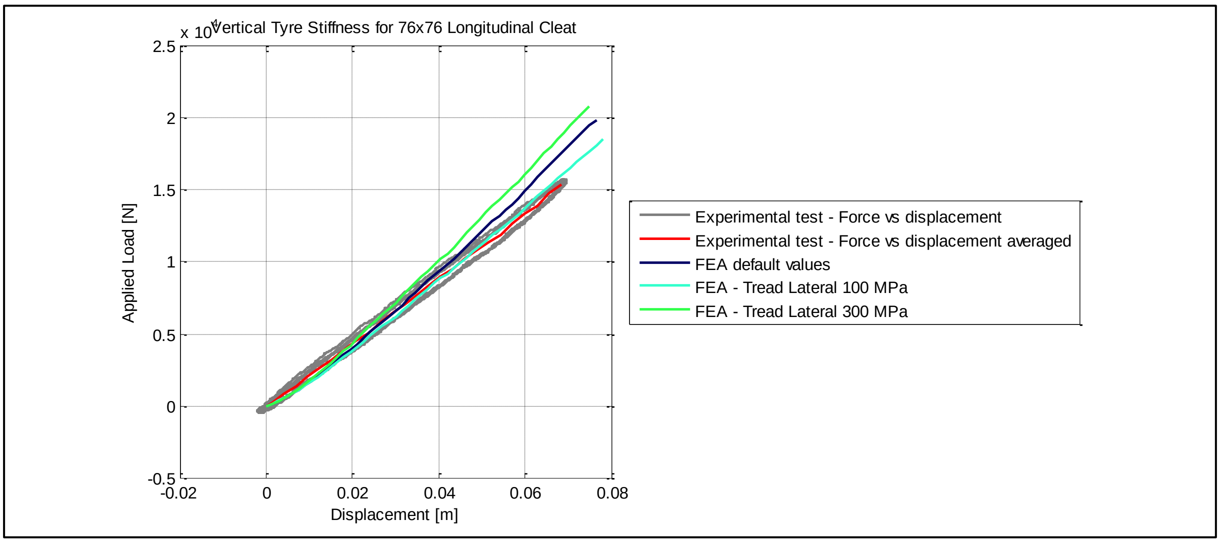

Figure A.32: Comparison for different lateral tread stiffnesses on a 76mm x 76mm longitudinal cleat

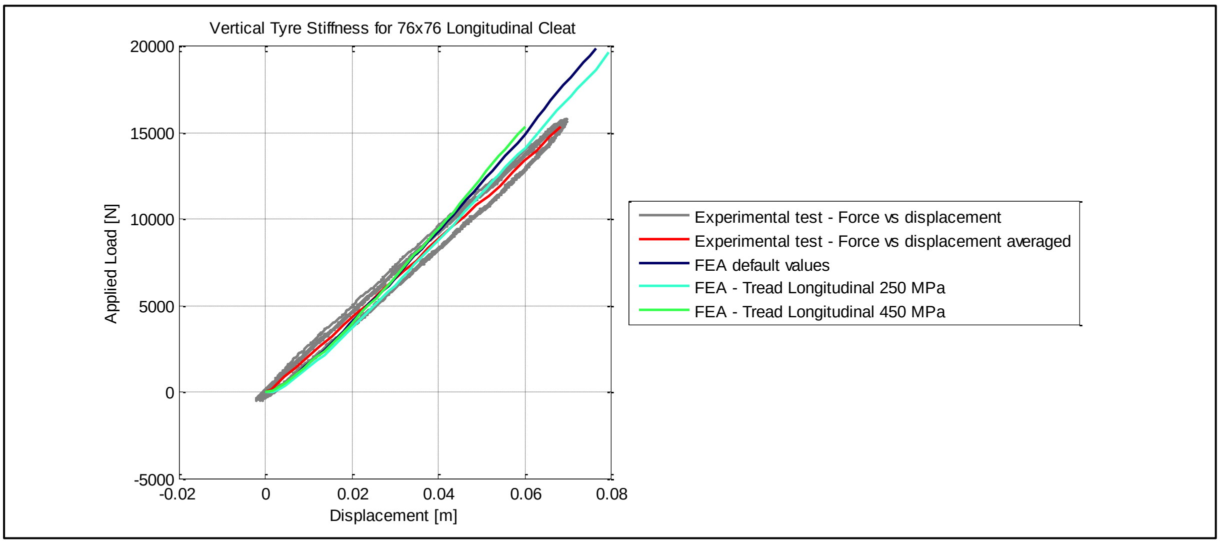

Figure A.33: Comparison for different longitudinal tread stiffnesses on a 76mm x 76mm longitudinal cleat

100x50 Lateral cleat

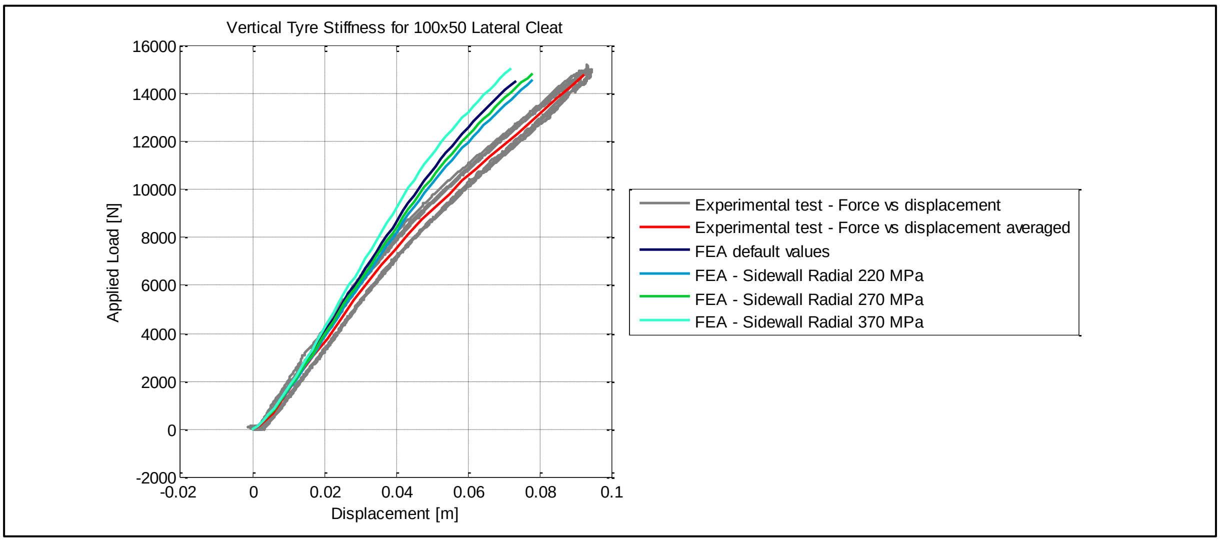

Figure A.34: Comparison for different radial sidewall stiffnesses on a 100mm x 50mm lateral cleat

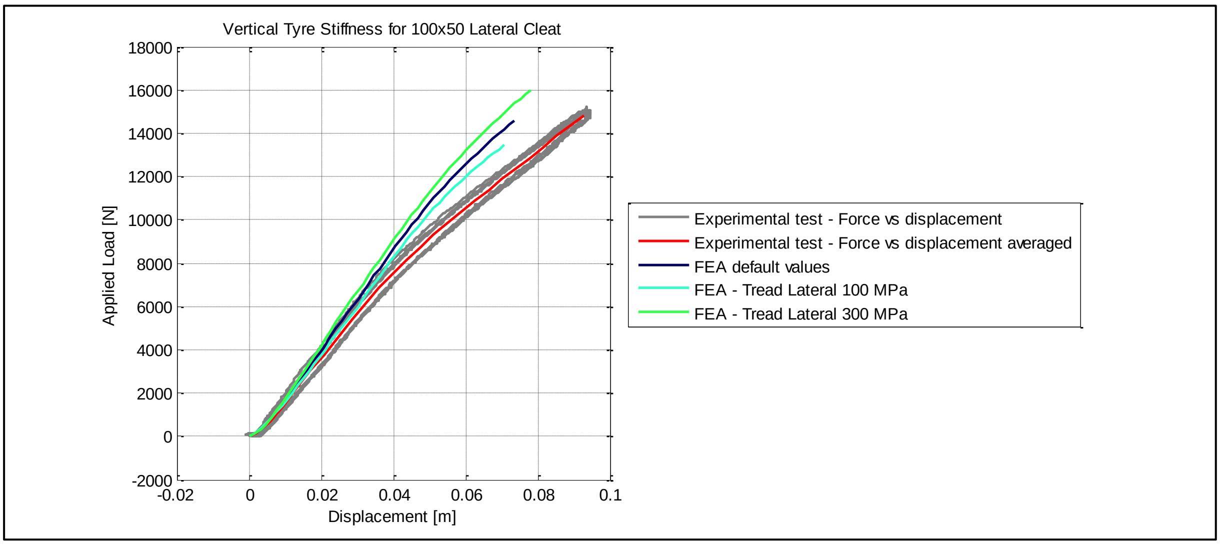

Figure A.35: Comparison for different lateral tread stiffnesses on a 100mm x 50mm lateral cleat

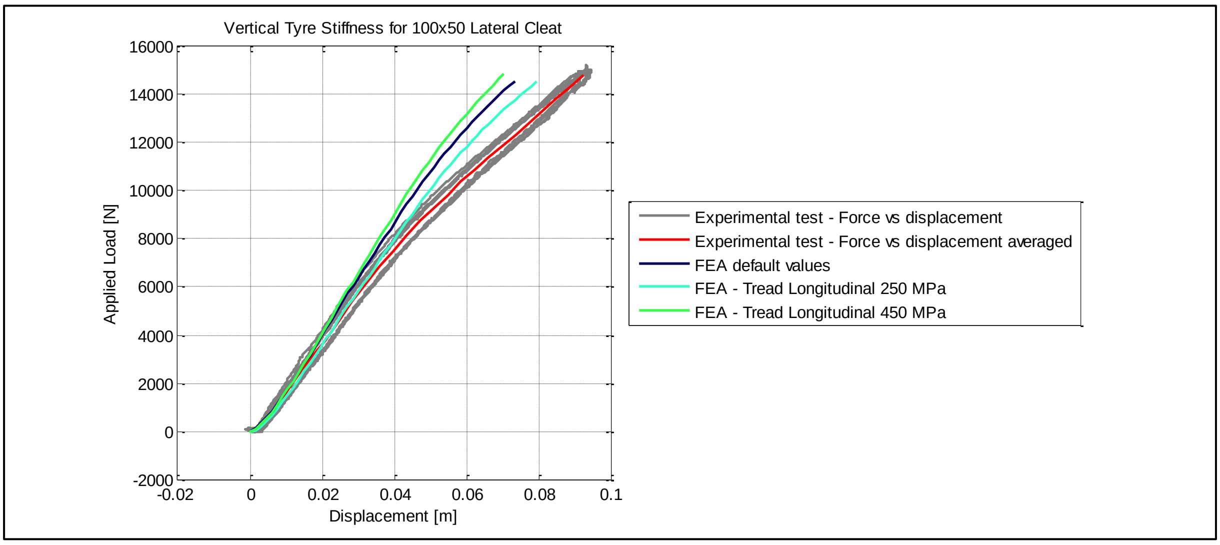

Figure A.36: Comparison for different longitudinal tread stiffnesses on a 100mm x 50mm lateral cleat

100x50 Longitudinal cleat

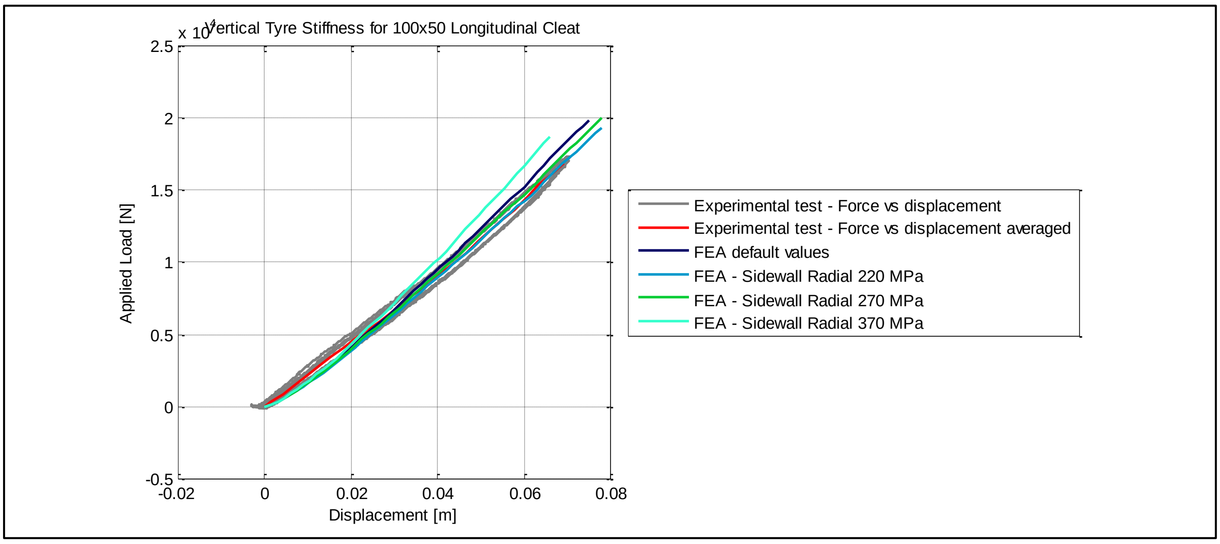

Figure A.37: Comparison for different radial sidewall stiffnesses on a 100mm x 50mm longitudinal cleat

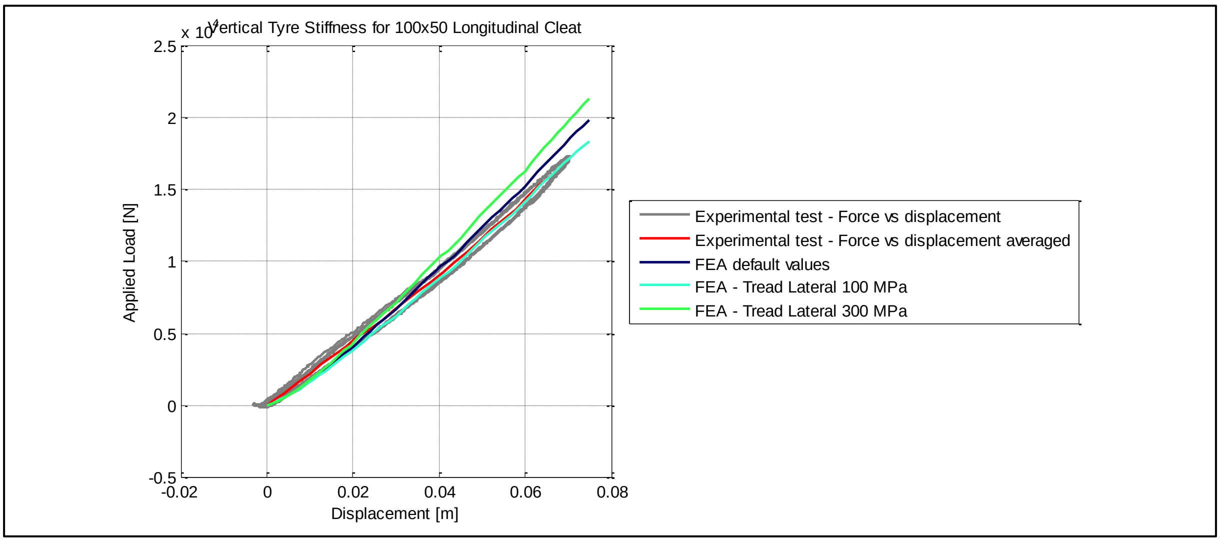

Figure A.38: Comparison for different lateral tread stiffnesses on a 100mm x 50mm longitudinal cleat

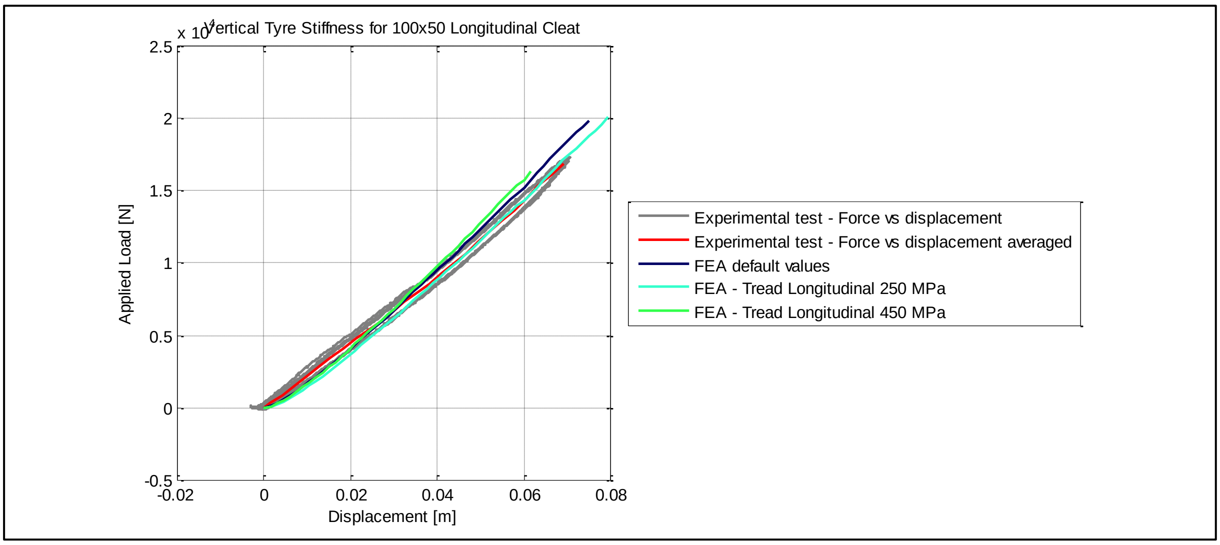

Figure A.39: Comparison for different longitudinal tread stiffnesses on a 100mm x 50mm longitudinal cleat

Appendix B – Load vs. displacement, experimental vs. final FE Model

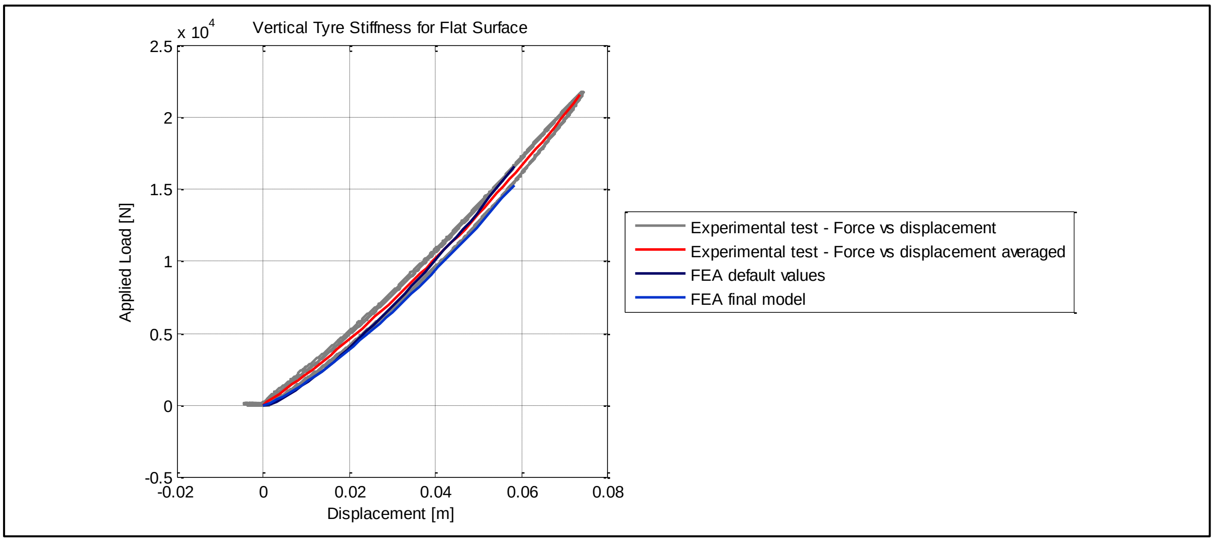

Figure B.1: Radial load vs. displacement with a flat surface

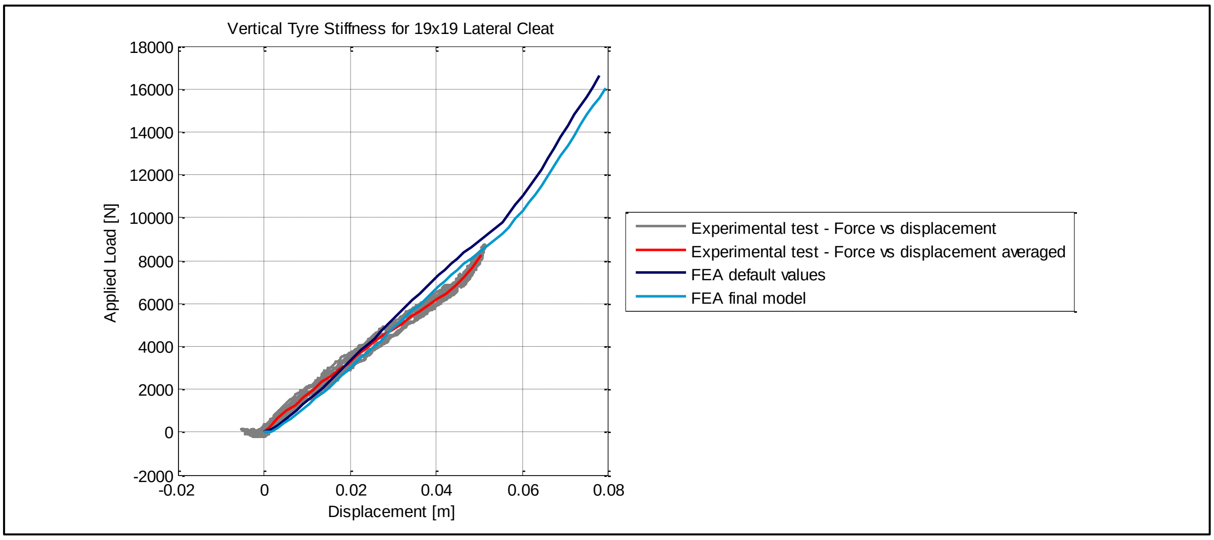

Figure B.2: Radial vs. displacement with a 19x19 lateral cleat

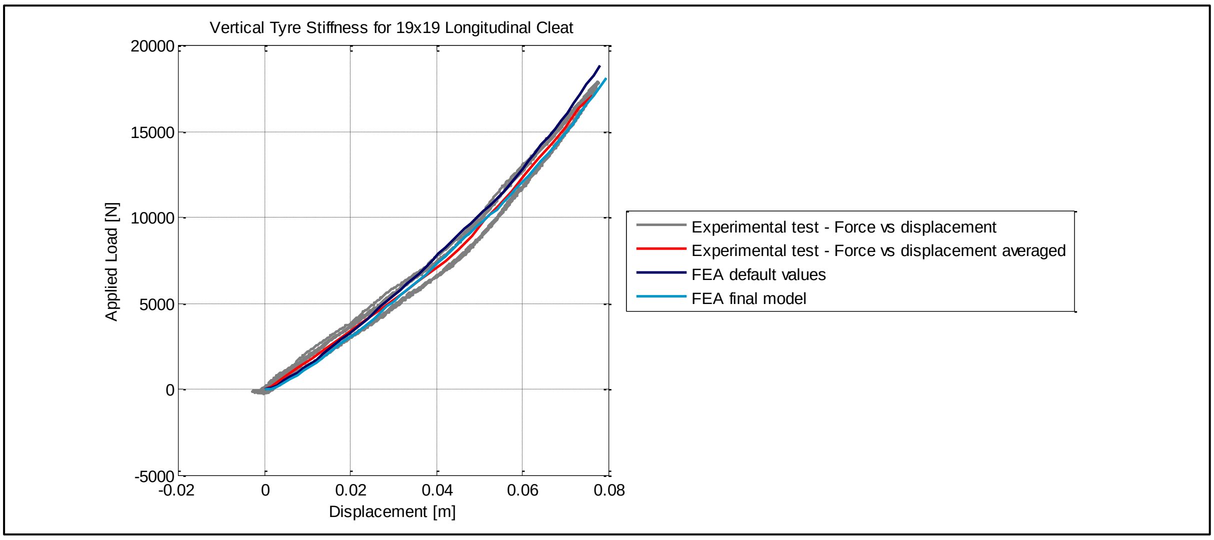

Figure B.3: Radial vs. displacement with a 19x19 longitudinal cleat

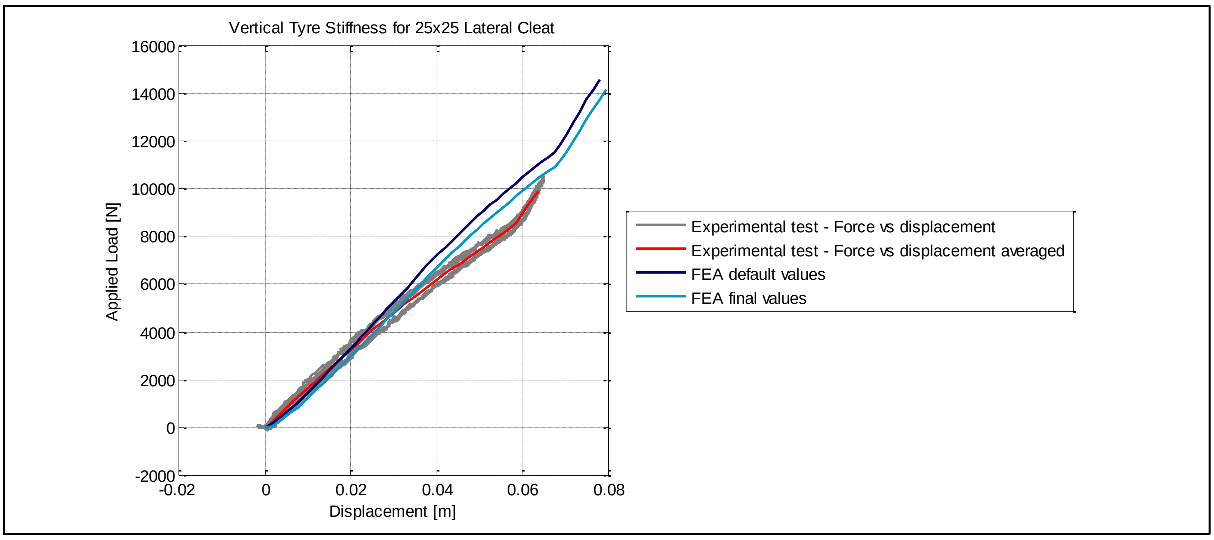

Figure B.4: Radial vs. displacement with a 25x25 lateral cleat

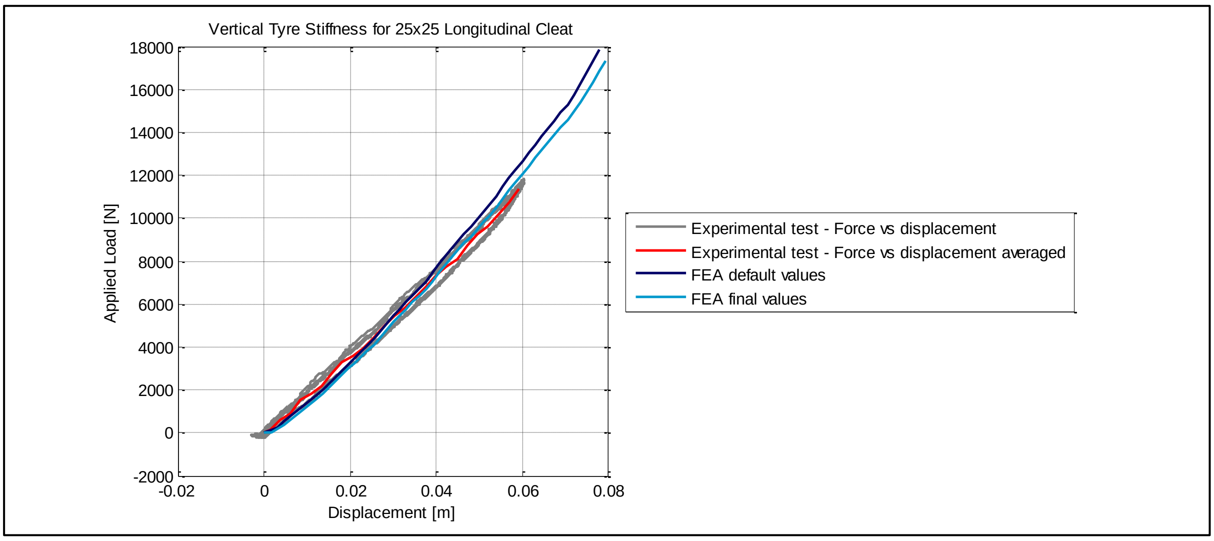

Figure B.5: Radial vs. displacement with a 25x25 longitudinal cleat

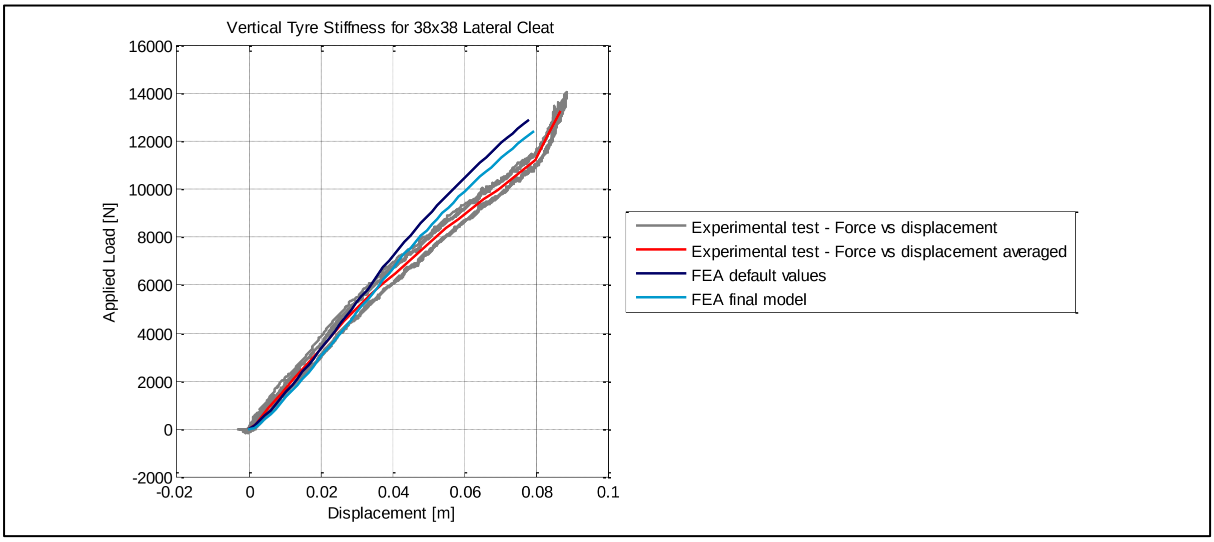

Figure B.6: Radial vs. displacement with a 38x38 lateral cleat

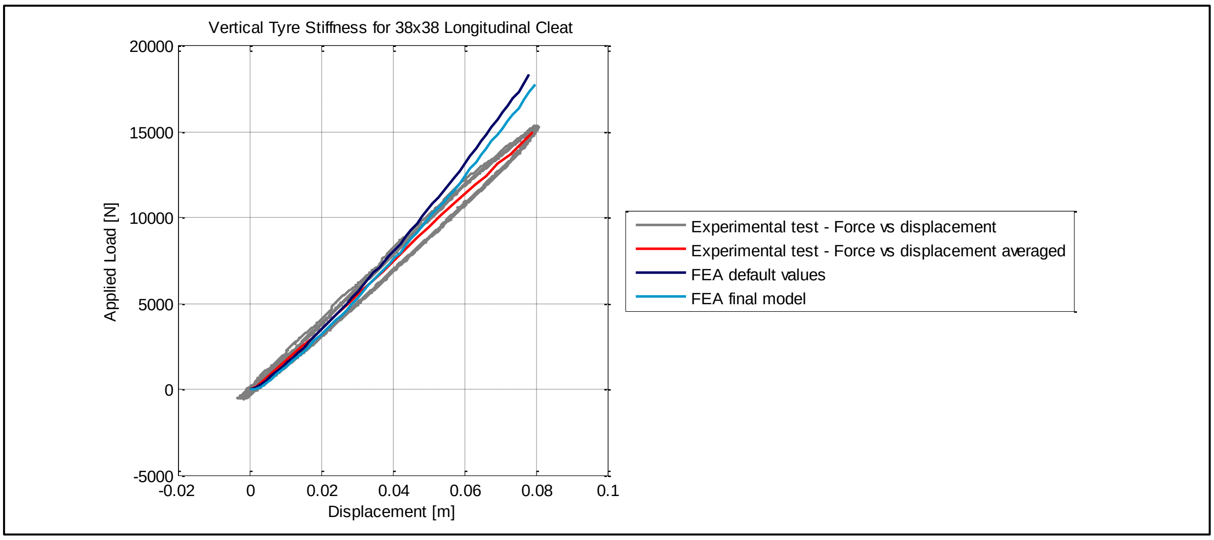

Figure B.7: Radial vs. displacement with a 38x38 longitudinal cleat

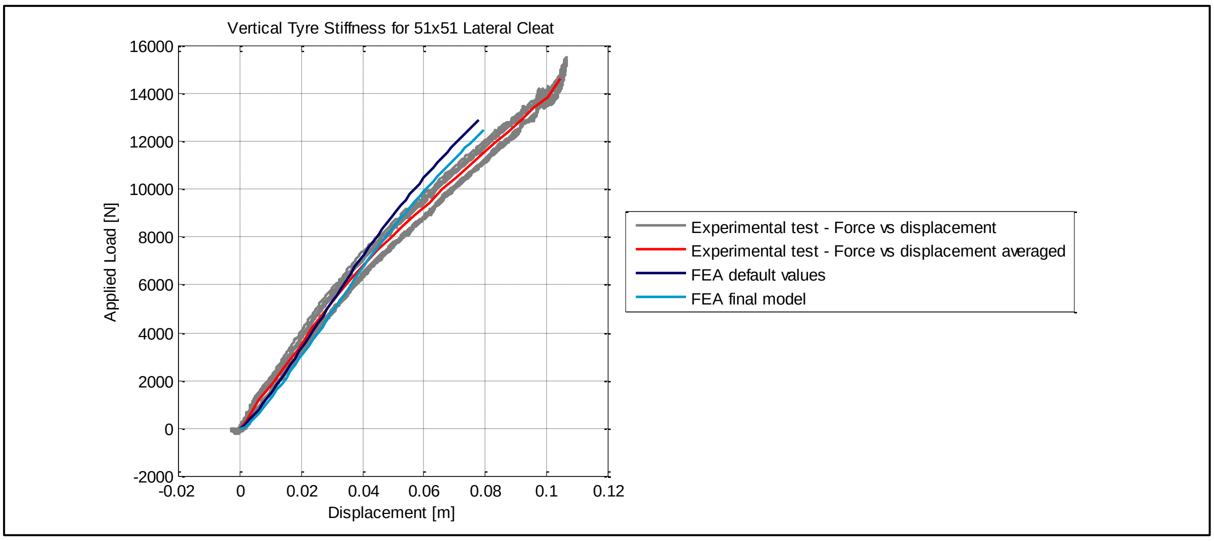

Figure B.8: Radial vs. displacement with a 51x51 lateral cleat

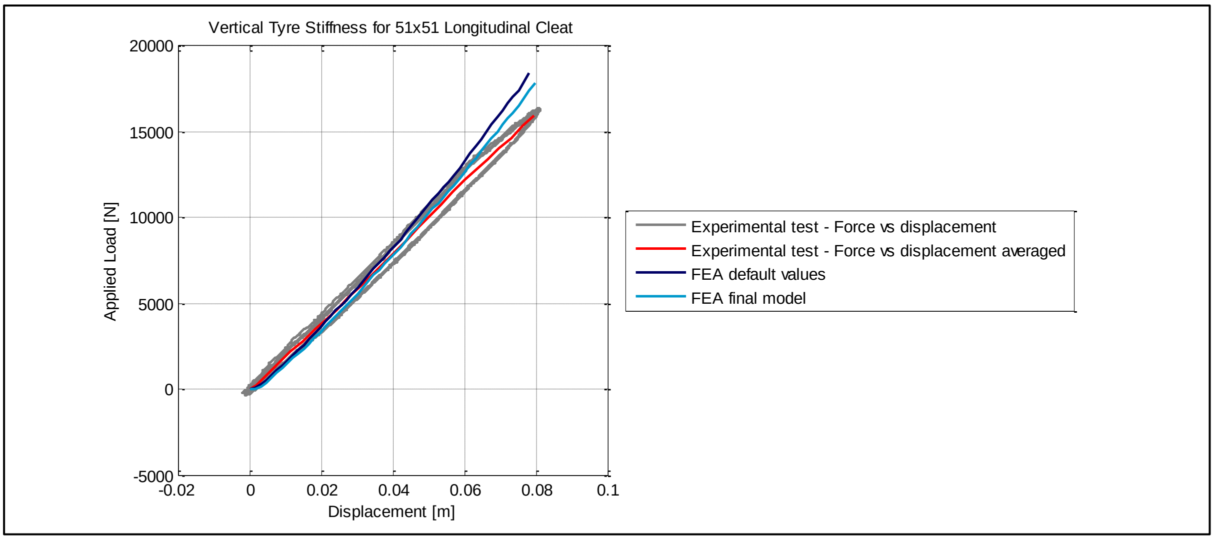

Figure B.9: Radial vs. displacement with a 51x51 longitudinal cleat

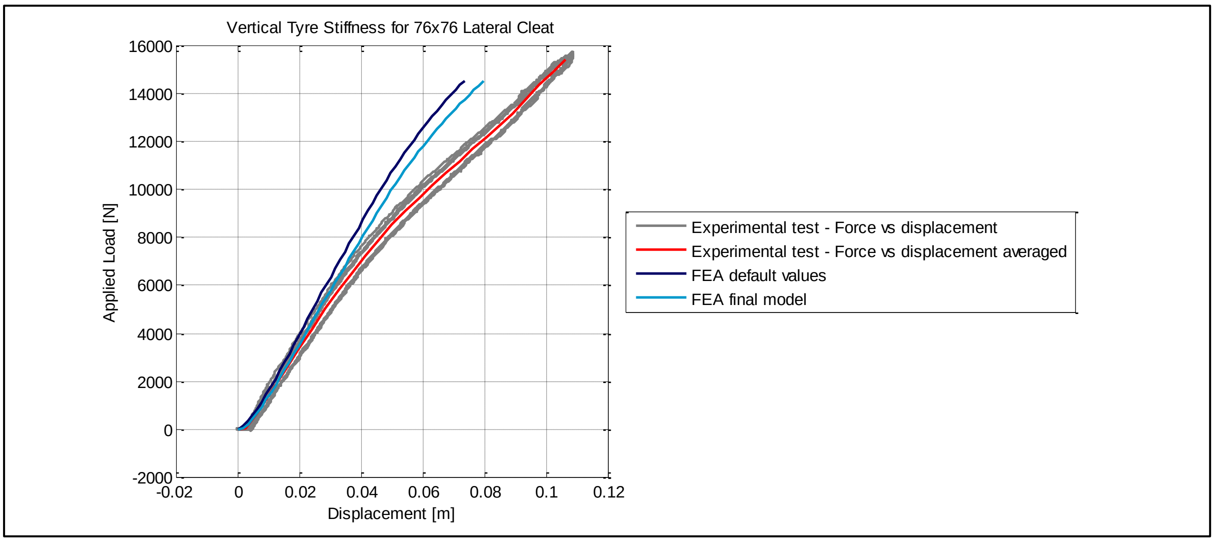

Figure B.10: Radial vs. displacement with a 76x76 lateral cleat

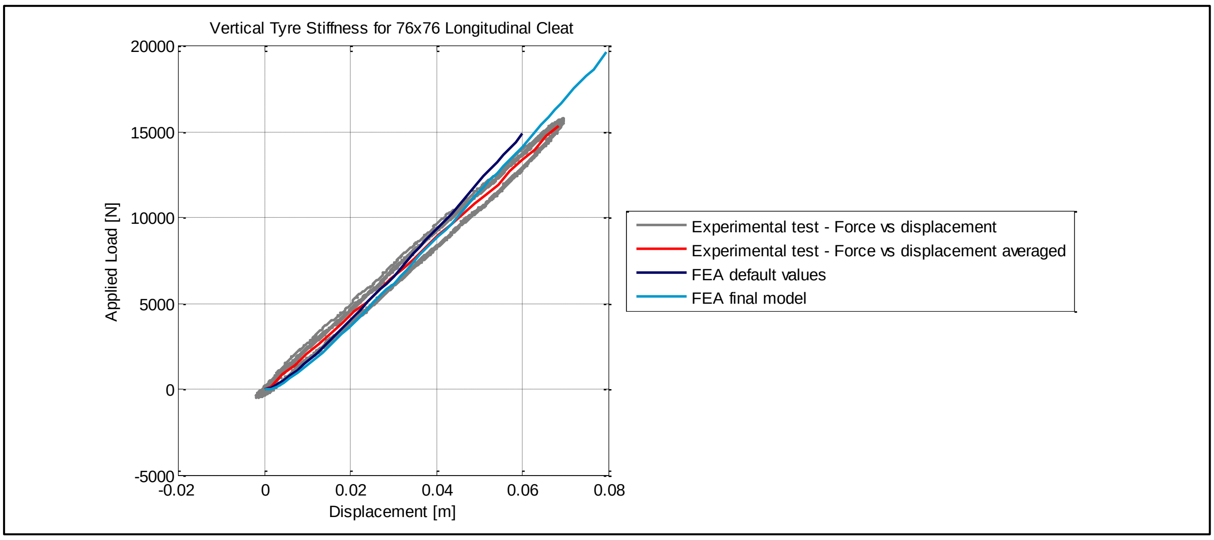

Figure B.11: Radial vs. displacement with a 76x76 longitudinal cleat

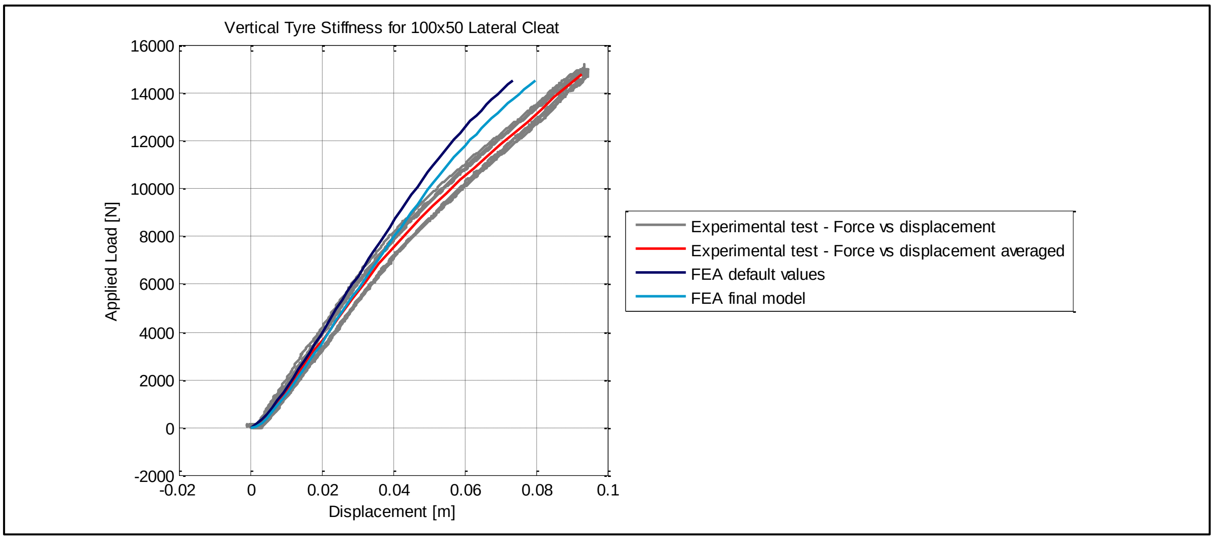

Figure B.12: Radial vs. displacement with a 100x50 lateral cleat

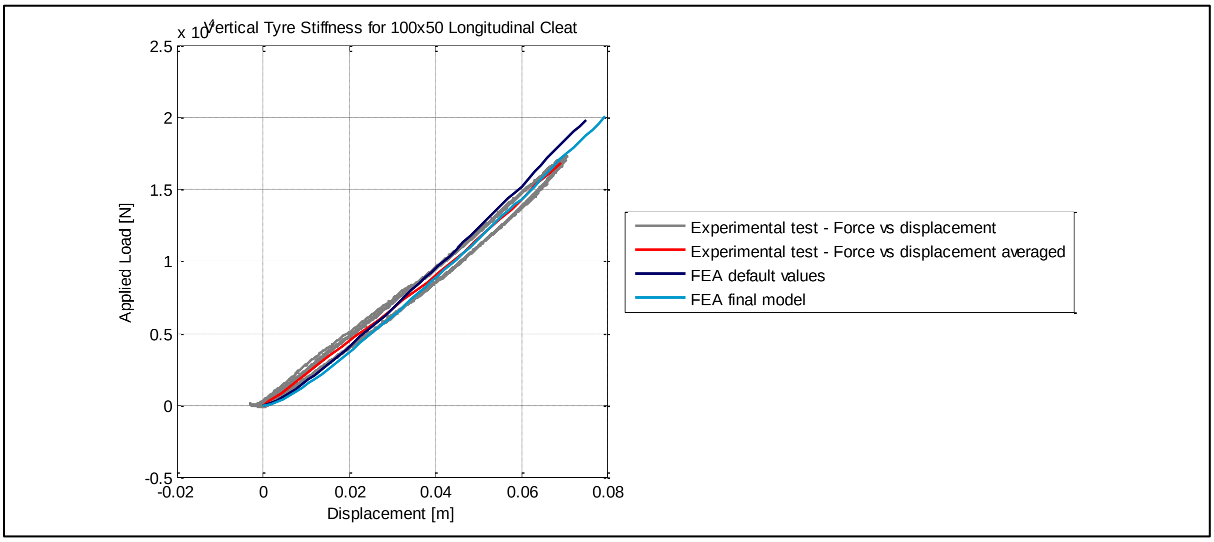

Figure B.13: Radial vs. displacement with a 100x50 longitudinal cleat

Appendix C – Sidewall profiles, experimental vs. final FE Model

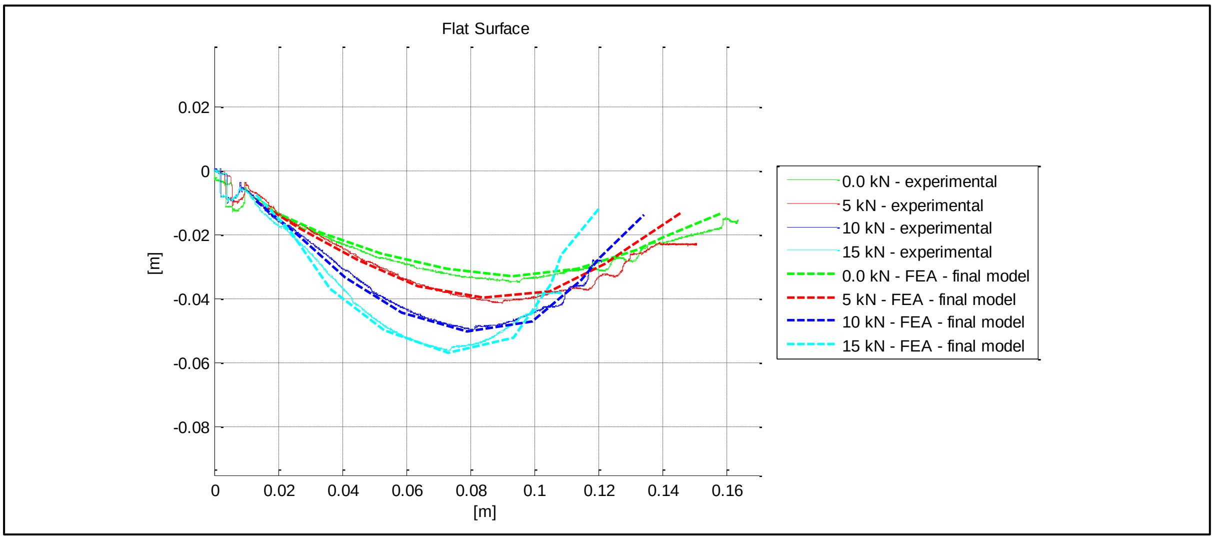

Figure C.1Sidewall profiles for a flat surface

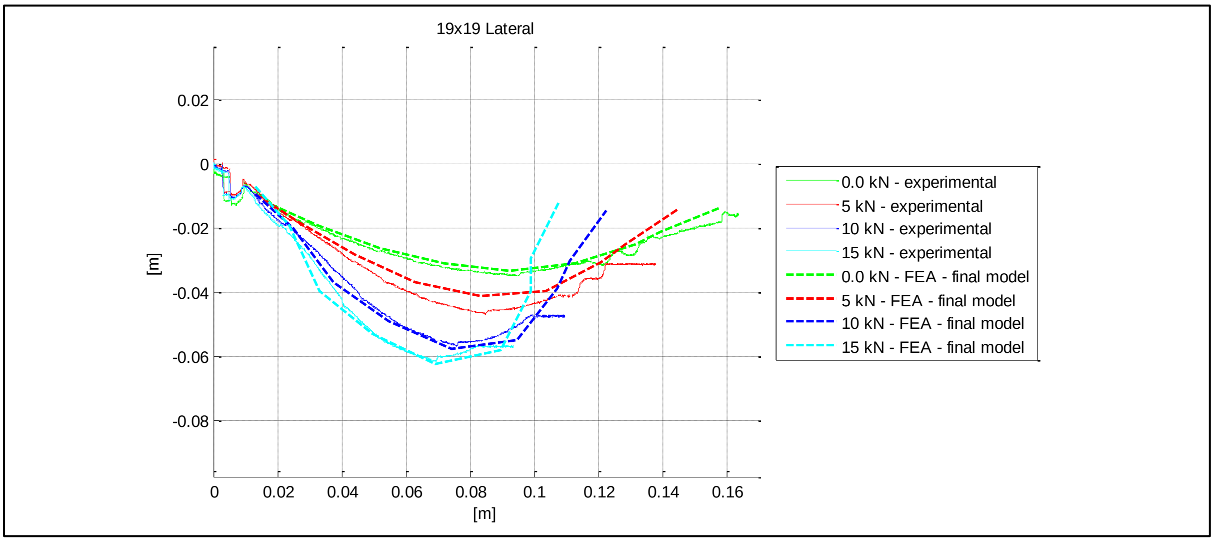

Figure C.2: Sidewall profiles for a 19x19 lateral cleat

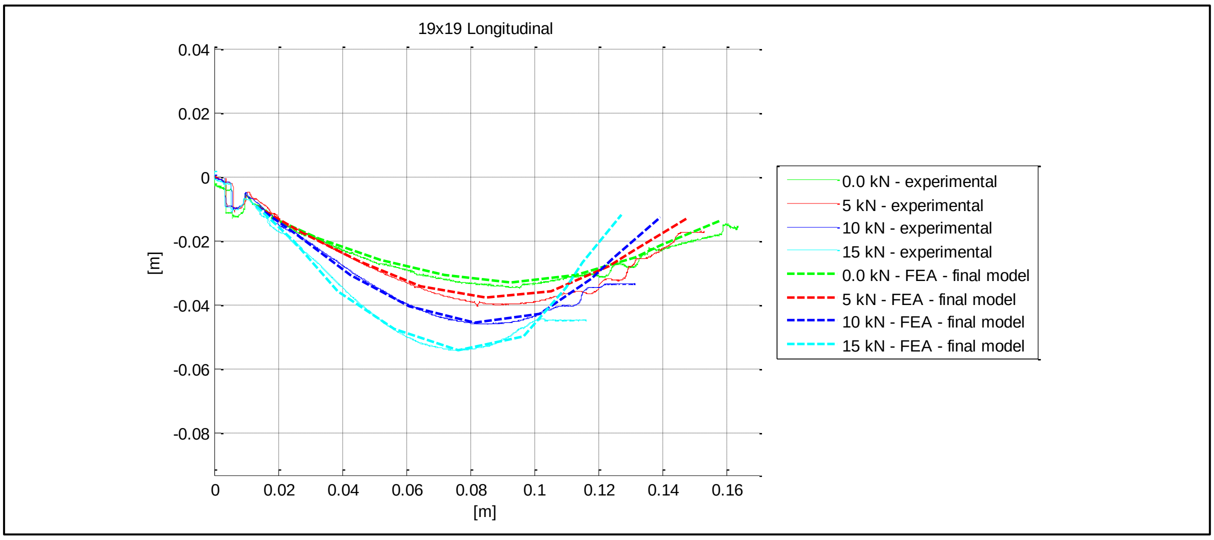

Figure C.3: Sidewall profiles for a 19x19 longitudinal cleat

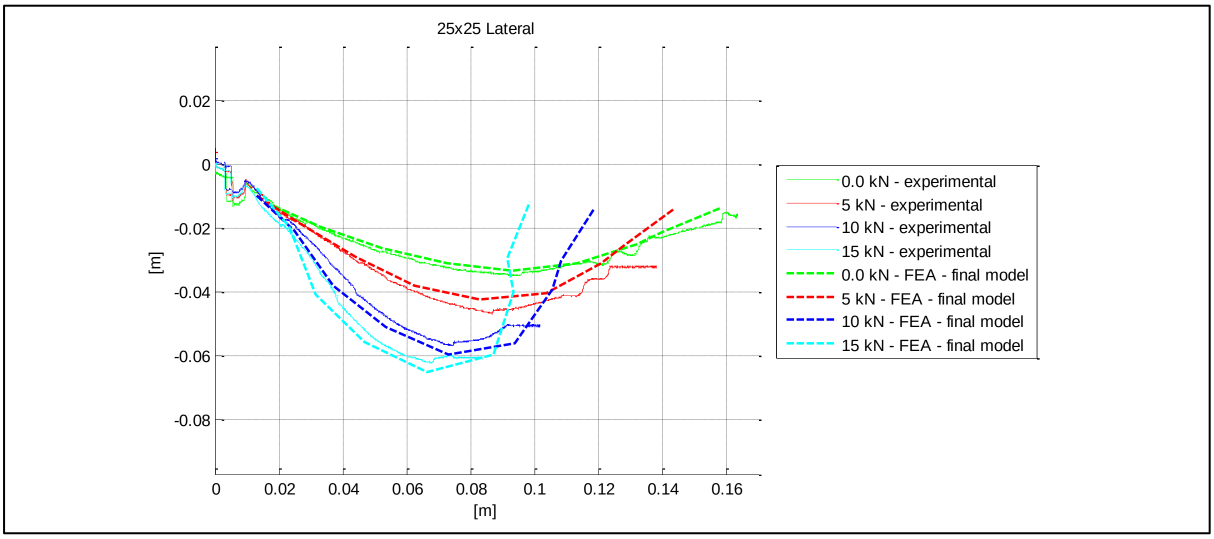

Figure C.4: Sidewall profiles for a 25x25 lateral cleat

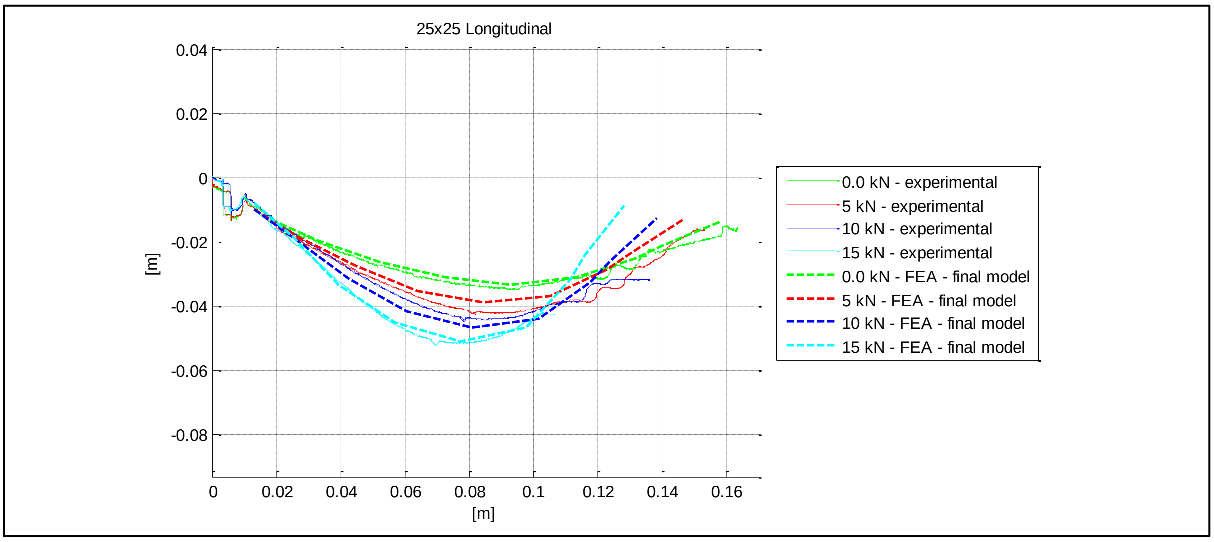

Figure C.5: Sidewall profiles for a 25x25 longitudinal cleat

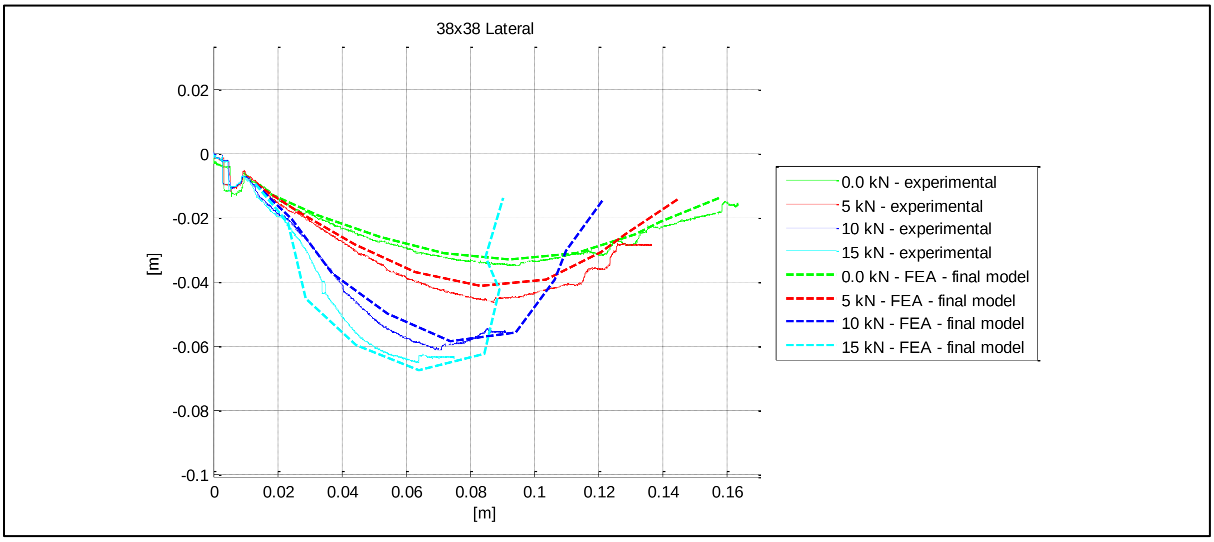

Figure C.6: Sidewall profiles for a 38x38 lateral cleat

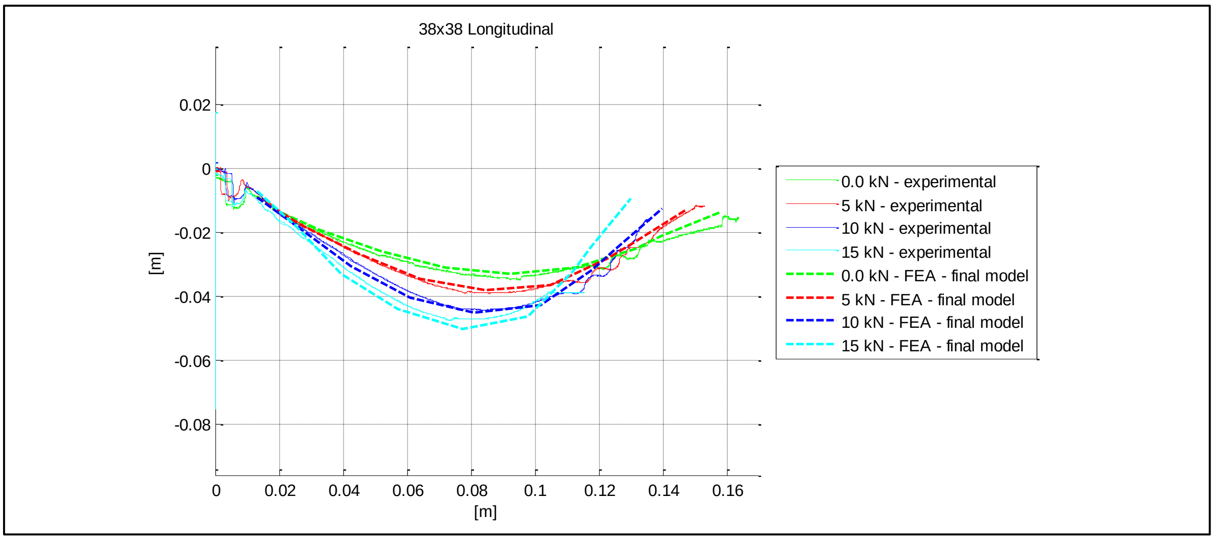

Figure C.7: Sidewall profiles for a 38x38 longitudinal cleat

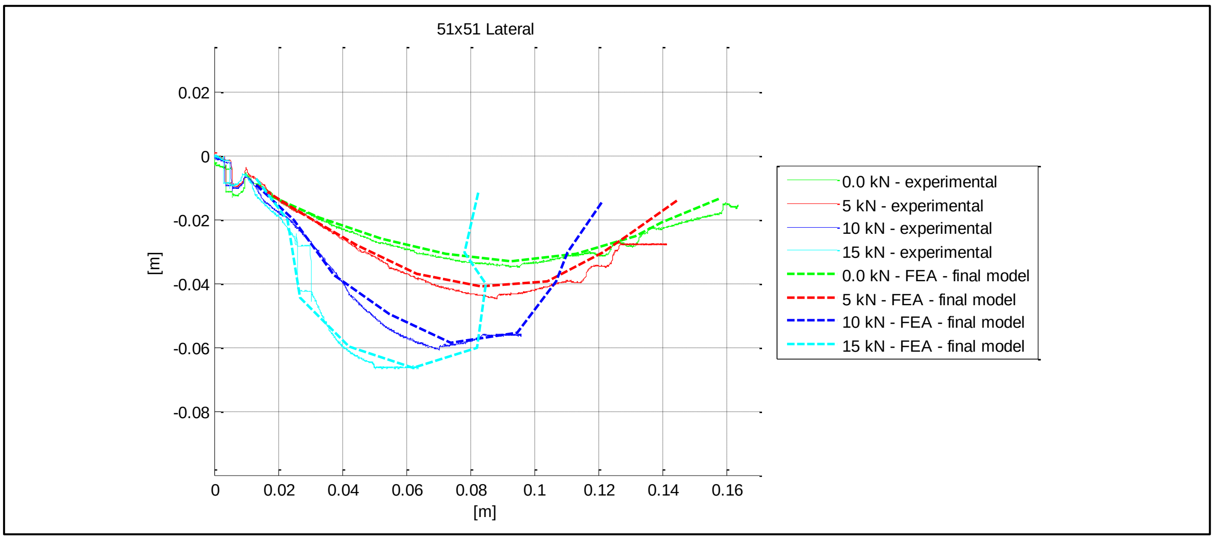

Figure C.8: Sidewall profiles for a 51x51 lateral cleat

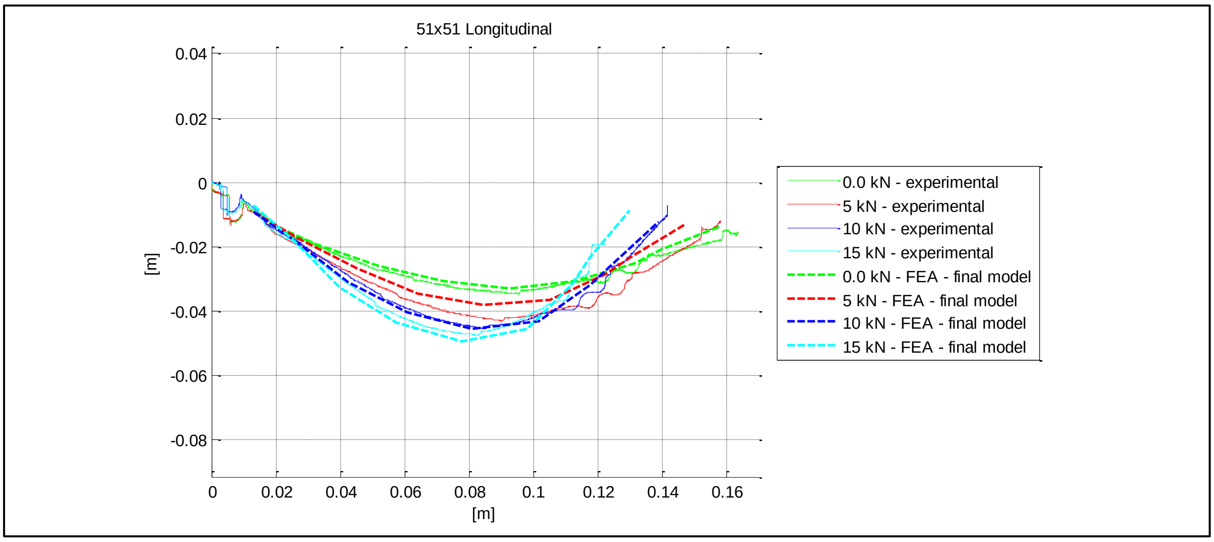

Figure C.9: Sidewall profiles for a 51x51 longitudinal cleat

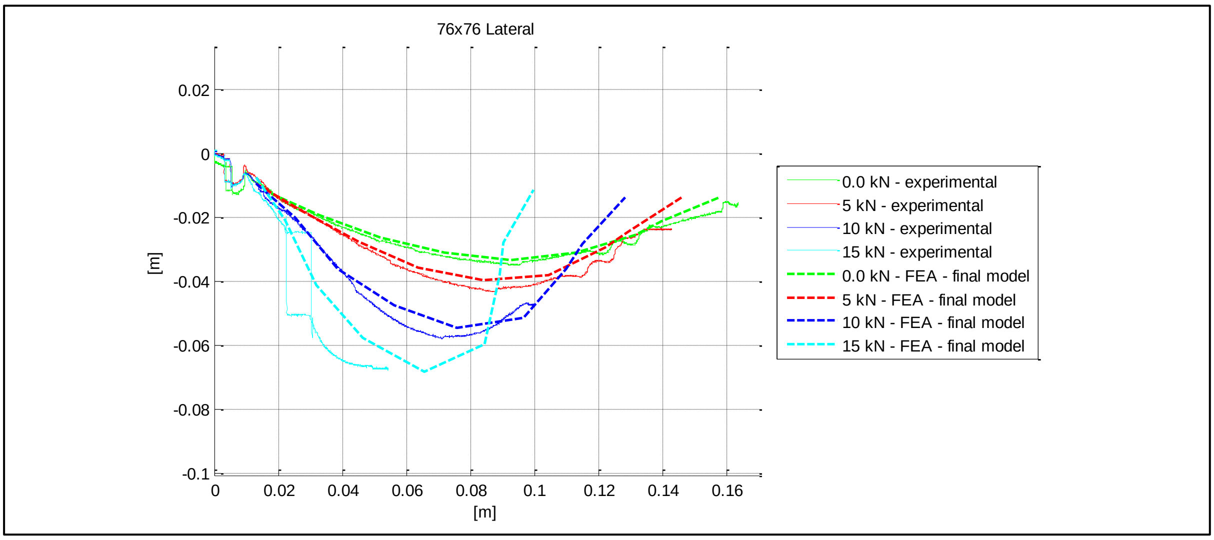

Figure C.10: Sidewall profiles for a 76x76 lateral cleat

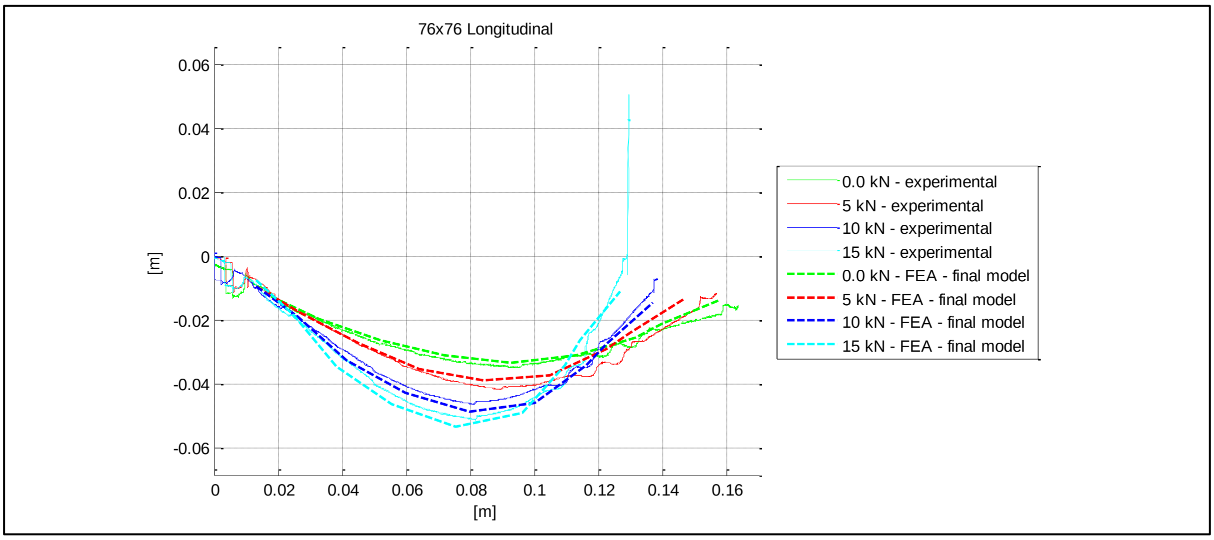

Figure C.11: Sidewall profiles for a 76x76 longitudinal cleat

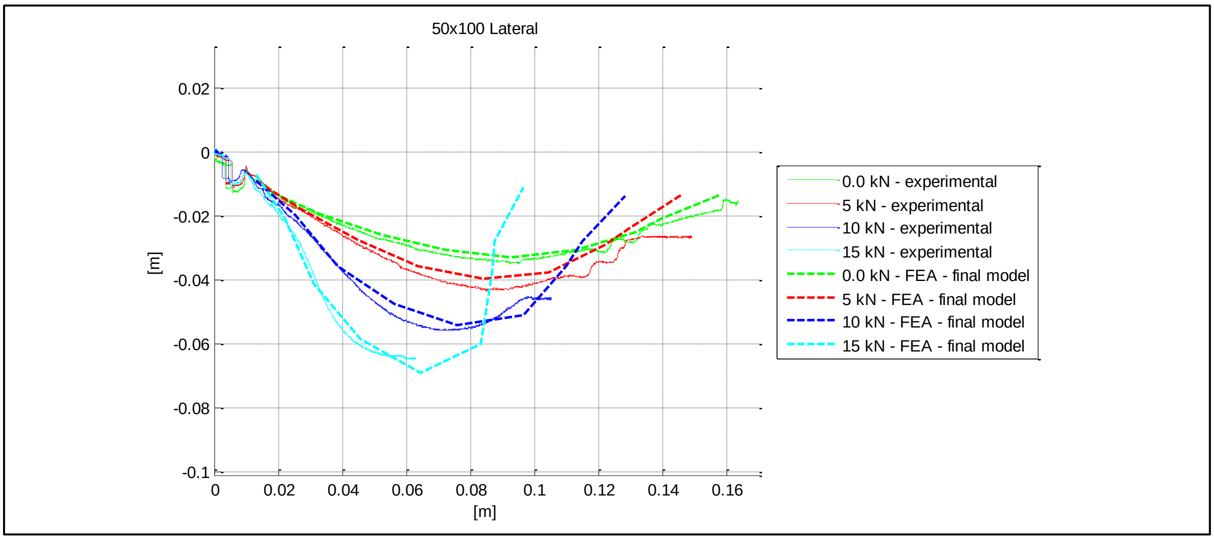

Figure C.12: Sidewall profiles for a 100x50 lateral cleat

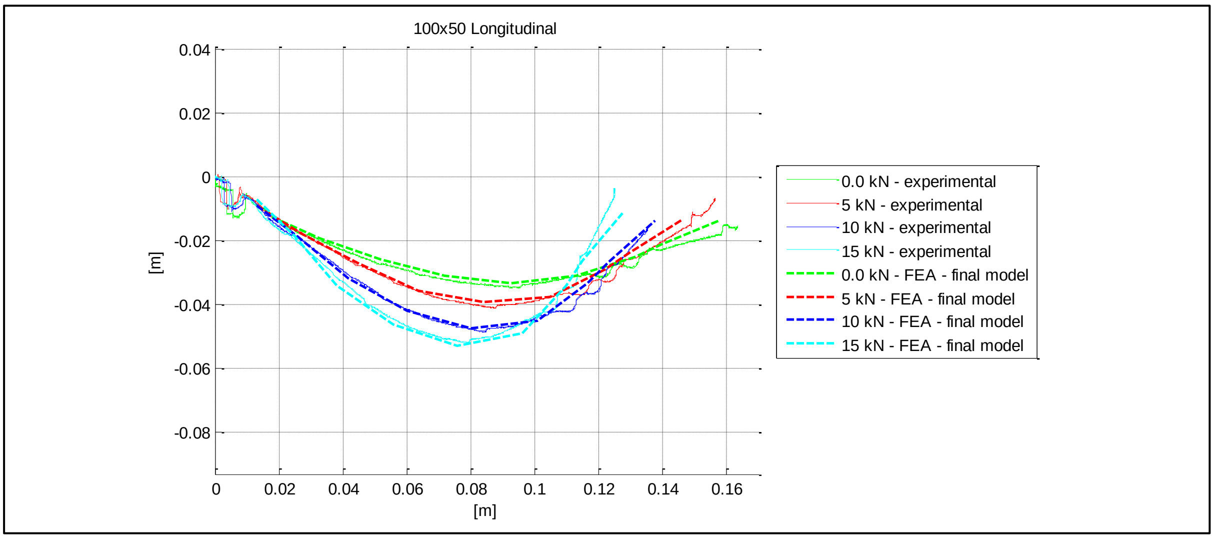

Figure C.13: Sidewall profiles for a 100x50 longitudinal cleat